

K – Further Contributions

- Polarimeter concepts for the EDM precursor experiment *page K 4*
- Spin Tune Determination of Deuteron Beam at COSY *page K 6*
- Polarisation Lifetime Studies for EDM Measurements at COSY .. *page K 8*
- Matrix integration of ODEs for spin-orbit dynamics simulation .. *page K 10*
- Upgrade of the Readout Electronics for the EDDA-Polarimeter .. *page K 11*
- Orbit excitation investigations *page K 12*
- Modeling of Spin Depolarization in Electrostatic Rings on Supercomputer JUROPA *page K 13*
- Spin Coherence Time Measurements at COSY *page K 14*
- Noise measurements at COSY *page K 17*
- Systematic error studies of storage ring EDM searches at COSY using an RF Wien filter, and the dependence of the beam polarization on the harmonics of a radio-frequency spin rotator *page K 19*
- Machine Development for Spin-filtering Experiments at COSY .. *page K 20*
- Construction of test station for the beam current measurement devices *page K 21*
- Analyzing powers of the $\vec{d}p \rightarrow \vec{d}p$ reaction at 1.2 and 2.27 GeV .. *page K 23*
- First results on A^y analyzing power measurements in $\vec{p}p$ elastic scattering experiment *page K 24*
- Measurements of the $\vec{p}n$ quasi-free elastic scattering at ANKE .. *page K 26*
- The cross section angular dependences of the $pp \rightarrow pp_s\pi^0$ reaction at several energies in the $\Delta(1232)$ excitation range *page K 27*
- The quasi-free reaction $pd \rightarrow d + \eta + p_{sp}$ close to threshold at ANKE *page K 28*
- Double differential cross sections for $d + p \rightarrow {}^3\text{He}\pi^+\pi^-$ *page K 29*

- Commissioning of the polarized deuterium gas target
at ANKE *page K 30*
- Data analysis of the Silicon Tracking Telescope for the $pn \rightarrow nK^+\Lambda$
reaction *page K 31*
- Improvement in position and spatial resolution determination
of the COSY-TOF Straw-Tube-Tracker *page K 32*
- Study of the beam polarization with COSY-TOF *page K 34*
- New Results of Studies on Piezoelectric Nozzle Units
for Pellet Targets *page K 36*
- Implementation of pellet tracking in physics experiments
- initial studies at WASA *page K 37*
- ABC effect and Resonance Structure in the Double-Pionic Fusion
to ${}^3\text{He}$ *page K 39*
- Systematic Study of Three-Nucleon Dynamics in the Cross Section of the
Deuteron-Proton Breakup Reaction *page K 40*
- Measurement of total and differential cross sections of $p + d \rightarrow {}^3\text{He} + \eta$
with WASA-at-COSY *page K 41*
- Investigation of the $p + d \rightarrow {}^3\text{He} + \eta'$ reaction
at WASA-at-COSY *page K 42*
- Search for ${}^4\text{He} - \eta$ bound state via $dd \rightarrow {}^3\text{He} p \pi$ and $dd \rightarrow {}^3\text{He} n \pi^0$ reaction
with the WASA-at-COSY facility *page K 43*
- Studies of Systematic Uncertainties of Polarization Estimation
for Experiments with the WASA Detector at COSY *page K 45*
- Energy Calibration of the WASA-at-COSY Forward Detector ... *page K 47*
- Study of the $\eta \rightarrow \pi^+ \pi^- \pi^0$ decay in pp collisions with WASA-at-COSY
page K 48
- Analysis of the decay $\eta \rightarrow \pi^+ \pi^- \gamma$ with WASA-at-COSY *page K 50*

- Pre-Studies for a Measurement of the $\omega\pi$ Transition Form Factor *page K 52*
- Simulations of the Measurement of the Form Factor for the D_s Semileptonic Decay with the PANDA Detector *page K 54*
- Clusterization for Recoil Proton Energy of Day-One Experiment Commissioning at COSY *page K 55*
- GPU Online Tracking Algorithms for the PANDA Experiment .. *page K 56*
- Development of a Silicon Strip Sensor Readout System *page K 58*
- Analysis of $\Lambda\bar{\Lambda}$ decay with PandaRoot Analysis Framework *page K 60*
- Adapting the TOFPET Readout ASIC for the MVD Strip Sensors *page K 62*
- ADC based readout system for the Straw Tube Tracker at PANDA *page K 63*
- The electronical time-resolution for the PANDA Straw Tube Tracker for Fast Flash-ADC read out *page K 69*
- A DIRC demonstrator at COSY *page K 72*

Polarimeter concepts for the EDM precursor experiment

P. Maanen^a, N. Hempelmann^a and J. Pretz^{a,b} for the JEDI Collaboration

The proposed method for a search for an Electric Dipole Moment of charged particles consists of storing the particles in a storage ring and letting the charged particles interact with a radial electric field. Starting with a horizontally polarized beam, the EDM signal would be a vertical polarization build-up. If the EDMs of deuteron and proton are in the order of 10^{-29} e·cm, the polarization build-up due to the EDM is in the order of nrad/s. Assuming a horizontal polarization lifetime of 1000 s, this means the vertical polarization to be detected is in the order of 10^{-5} .

For the polarization measurement, nuclear scattering which uses spin-dependent asymmetries in the nuclear scattering cross section to measure the beam polarization was chosen. A vertical polarization is associated with a left-right asymmetry in the scattering cross section while a longitudinal polarization leads to a up-down asymmetry. A quantity to characterize the statistical accuracy of a polarimeter is the so called Figure of Merit (FOM) it is defined as follows:

$$\mathcal{F} = \sigma \cdot A_y^2$$

This means, in order to maximize the statistical accuracy of a polarimeter, one has to choose a process with the highest possible cross section and analyzing power.

Target material

Different target materials were evaluated for their applicability as a polarimetry target. In Fig. 1 the differential FOM for Deuteron-Proton and Deuteron-Carbon elastic scattering are shown. As one can clearly see, the differential Figure of Merit for the dC scattering is more than an order of magnitude higher. Both processes clearly favor the forward direction.

Target type

In principle, many different target types are available for use. The candidates evaluated here are cluster targets and solid state targets. Both have advantages and disadvantages. Solid State Targets in general are easier to handle than cluster targets and target densities in the order of magnitude of 10^{20} cm $^{-2}$ are achievable. However, in order to better control systematic uncertainties, it is preferable to sample particles from the beam statistically. Even white noise extraction can change the spin tune. Cluster targets can achieve target densities of up to 10^{14} cm $^{-2}$ - 10^{15} cm $^{-2}$. Most gases can be prepared for use as a cluster target. The advantage of a cluster target target is that the extracted particles are statistically sampled from the whole beam without changing the orbit. Additionally it is possible to simply turn the target on and off at arbitrary times if one only desires to measure the polarization at specific times.

Detector technologies

Several detector technologies have been evaluated for their applicability for an EDM polarimeter. The

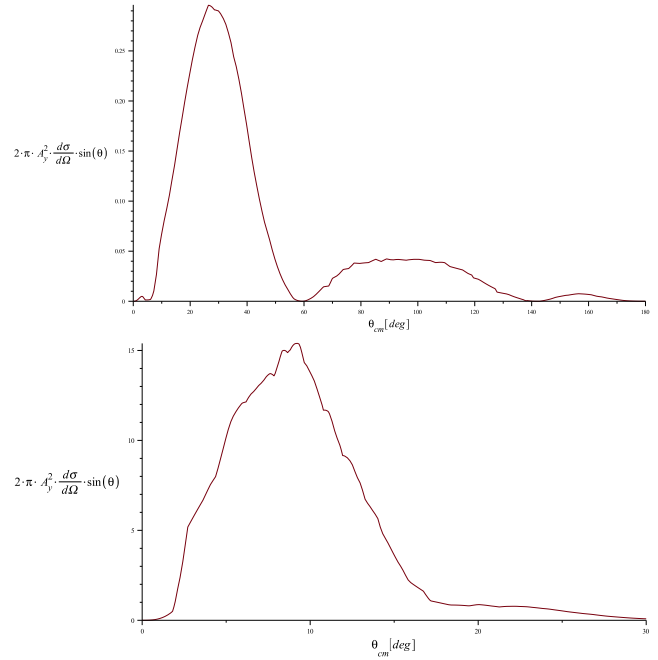


Figure 1: top: Differential FOM for Deuteron-Proton scattering at $T_d = 270$ MeV[1] bottom: The same quantity for Deuteron-Proton scattering at the same energy[2]. Note the different scale.

most probable candidates are Silicon (strip) detectors and scintillating fibres. While in principle a 4-fold partition of the active Volume would suffice to extract up-down and left-right asymmetries, a polarimeter capable of tracking individual particles has certain statistical advantages[3] and could be used to measure the phase space of the beam. The top priority for an EDM polarimeter is the stability of the measurement conditions over time.

Silicon detectors Silicon strip detectors are currently in use in Jülich at the ANKE and PAX experiments. Because they can be operated in the COSY ultra high vacuum, it is possible to place them very close to the beam with a minimum of material between the interaction region and the active detectors. The spacial resolution of silicon strip detectors depends on the chosen strip pitch. A small pitch means high precision, but the number of readout channels rise which raises costs.

Scintillating fibers Scintillating fiber (SciFi) trackers have previously been used for the PERDAIX experiment and in the hadron therapy group at RWTH Aachen. PERDAIX has achieved a spacial resolution of better than $50\text{ }\mu\text{m}$ [4]. However, as they can not be operated in high vacuum, there has to be some material between the reaction region and the active detectors. Simulation studies have shown that simply placing SciFi trackers on the outside of the beampipe would limit the vertex resolution to $\mathcal{O}(1\text{ mm})$. Simulation Studies with a

more sophisticated detector geometry using mylar windows to minimize the material budget are currently ongoing.

We recently received a prototype module of the PER-DAIX Tracker. Hardware studies are currently ongoing.

Beam emittance measurement

In order to better control systematics it would be preferable to measure the beam phase space simultaneously with the polarization. Preliminary analysis of data taken with the ANKE STT have shown that an emittance measurement is in principle possible, but one has to be careful not to be dominated by multiple scattering, especially at low beam momenta.

^aRWTH Aachen University, Germany

^bIKP FZJ Germany

References

- [1] SAKAMOTO, N. et al., Physics Letters B **367** (1996) 60 .
- [2] SATOU, Y. et al., Physics Letters B **549** (2002) 307 .
- [3] PRETZ, J., Nuclear Instruments and Methods in Physics Research A **659** (2011) 456.
- [4] BACHLECHNER, A. et al., Nuclear Instruments and Methods in Physics Research A **695** (2012) 91 .

Spin Tune Determination of Deuteron Beam in COSY

D. Eversmann^a for the JEDI collaboration

This report describes how the spin tune v_s of a deuteron beam stored in the storage ring COSY is determined. Since the spin tune is defined as the number of spin rotations during one orbit revolution of the particle in the ring

$$v_s = \frac{f_s}{f_{cyc}}, \quad (1)$$

it is necessary to determine the spin precession f_s in the horizontal plane in units of the cyclotron frequency f_{cyc} of the particles. This is done by extracting a bunched beam slowly on a solid carbon target and recording the time of every event of a elastically scattered deuteron detected in the EDDA detector. Counting the particle rates of opposite detector areas (e.g. up and down) allows to calculate an asymmetry related to the polarization of the beam.

For a beam momentum of $p_d = 0.97$ GeV/c the cyclotron frequency is approximately $f_{cyc} \approx 750$ kHz which leads to a spin precession frequency of

$$f_s = v_s f_{cyc} = \gamma G_d f_{cyc} \approx 120$$
 kHz, (2)

where $\gamma = 1.125$ is the relativistic Lorentz factor and $G_d \approx -0.143$ denotes the anomalous magnetic moment of deuteron. The relation $v_s = \gamma G$ is valid for a particle on a closed orbit in the horizontal plane in a pure magnetic ring. For a beam of 10^9 particles per fill the detector rate is in the order of 5 kHz which is far too low to measure the spin precession in real time. To determine the spin tune it is necessary to start with a first approximation. In first order this is provided by calculating the spin tune from the relation $v_s = \gamma G$.

Under the precondition that the spin tune itself does not change much within a macroscopic interval of several seconds, it is possible to sort all events detected during this macroscopic interval into a microscopic period T_s defined by the assumed spin tune

$$T_{s,assumed} = \frac{1}{f_{s,assumed}} = \frac{1}{v_{s,assumed} f_{cyc}}. \quad (3)$$

Beeing near to the real spin tune of the beam and calculating the asymmetries from the detector rates the spin precession reveals by means of a sine wave shown in figure 1. The fit-function is described by a superposition of a sine and a cosine with the following parameterisation:

$$f_{fit,s}(\phi_s) = p_0 \sin(\phi_s) + p_1 \cos(\phi_s) + p_2 \quad (4)$$

The offset p_2 occurs due to several systematic effects like geometric displacements of the detector or missalignment of the beam which leads to shifts in the counting rates. The absolute asymmetry $A_{UD,abs} = \sqrt{p_0^2 + p_1^2}$ is extracted by calculating the square root of the sum of the squared amplitudes

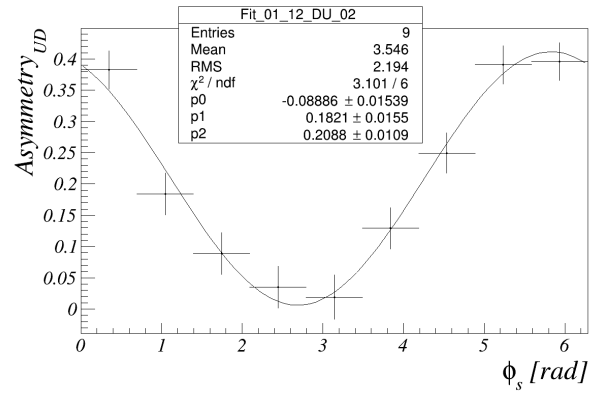


Fig. 1: Asymmetry distribution for a macroscopic time interval of one second. To obtain enough statistics for each asymmetry calculation the phase binning is set to 9.

p_0 and p_1 . In the following two methods are described to determine the spin tune

If the selected spin tune is close to the real spin tune the asymmetry will reach its maximum. In figure 2 an amplitude scan for a macroscopic time interval of one second with a central spin tune $v_{s,central} = -0.16097485$ is shown for 200 different spin tunes with a scan range of 10^{-5} that means one step of the selected tune represents a spin tune change of $\Delta v_s = 5 \cdot 10^{-8}$. A clear maximum close to $v_{s,max} = 104$

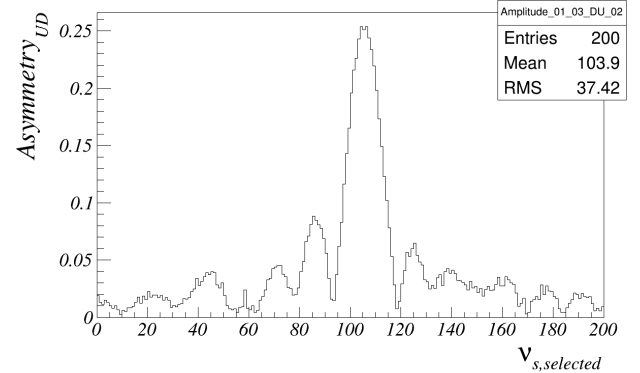


Fig. 2: Amplitude scan for 200 different spin tunes used in the analysis

can be seen. This method allows a determination of the spin tune for every macroscopic time interval with a precision of approximately 10^{-8} by following formula:

$$v_s = v_{s,central} + \Delta v_s \cdot (v_{s,max} - 100) \quad (5)$$

In order to achieve a better sensitivity of the spin tune determination the selected spin tune can be fixed $v_{s,fixed}$ in the analysis for the whole cycle. A non-linear change of the

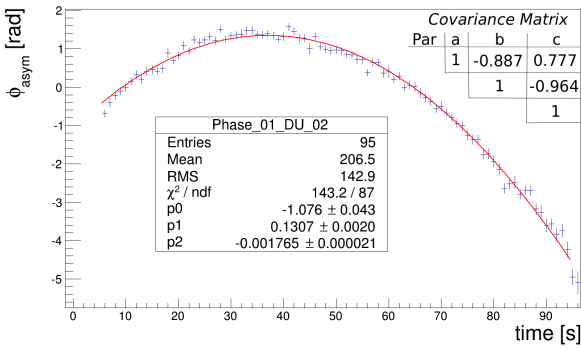


Fig. 3: Phase distribution for one cycle fitted by a quadratic function

asymmetry phase $\phi_{asym} = \arctan(\frac{p_1}{p_0})$ (see: figure 1) in time indicates a drift of the spin precession frequency. In figure 3 a typical phase distribution for a whole cycle (≈ 100 s) is shown. A quadratic behaviour can be observed with a total change of the asymmetry phase of approximately 10 radian. The change of the spin tune can be calculated from the following relation:

$$\Delta v_s(t) = \frac{f_s(t)}{f_{cyc}} = \frac{\omega_s(t)}{2\pi f_{cyc}} = \frac{1}{2\pi f_{cyc}} \frac{\partial \phi_{asym}(t)}{\partial t}$$

$$= \frac{1}{2\pi f_{cyc}} (p_1 + 2p_2 t) = 2.12 \cdot 10^{-7} (p_1 + 2p_2 t),$$

where p_1 and p_2 are the linear respectively quadratic coefficients of the parabola fit in figure 3.

From this the total spin tune is then simply calculated by

$$v_s(t) = \Delta v_s(t) + v_{s,fixed}. \quad (6)$$

A negative quadratic coefficient represents a decreasing value of the absolute spin tune during one cycle.

Applying gaussian error propagation the precision of the spin tune measurement depends on the errors of the coefficients σ_{p_1} , σ_{p_2} and their correlation coefficients

$$\sigma_{v_s(t)}^2 = (2.12 \cdot 10^{-7})^2 \cdot (\sigma_{p_1}^2 + 4t^2 \sigma_{p_2}^2 + 4t \text{cov}(p_1, p_2)) \quad (7)$$

with the given covariance matrix of the fit in figure 3. This allows to calculate the error of the spin tune at each time in the cycle.

In figure 4 the absolute value of the spin tune calculated from the asymmetry phase fit is plotted with its error marked as a blue band. It decreases by $6 \cdot 10^{-8}$ during the 90 seconds interval of extraction time. The smallest error ($\approx 10^{-10}$) of the spin tune determination is reached after 40 seconds due to formula (7).

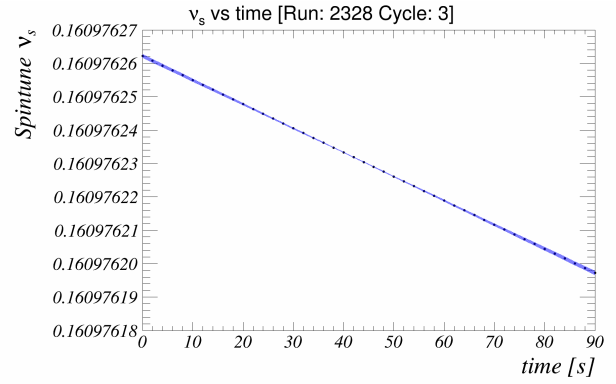


Fig. 4: Decreasing spin tune for one cycle. The blue band indicates the error of the spin tune

During the beamtime in August 2013 several sets of idle precession runs were performed to investigate the spin coherence time for different sextupole settings in the ring. In figure 5 the absolute value of the spin tune of every cycle and run for a group of runs is shown where the beam was extracted by applying a white noise electrical field (vertical lines delimits the runs). One sees that the spin tune changes within one run from cycle to cycle in the order of 10^{-8} and from run to run there are changes in the order of one magnitude higher. In particular after run 2101,2135 and 2165 huge jumps of the

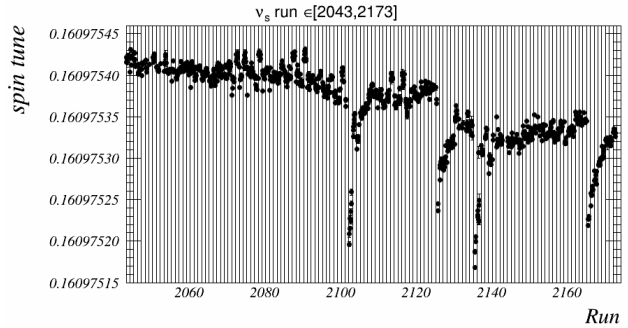


Fig. 5: Spin tune for a set of runs where the sextupole settings were changed to investigate the spin coherence time.

spin tune are discovered. One explanation for this behaviour could be the large changes of the sextupole magnets which were made before this runs. In fact sextupole magnets cause spin tune changes and it seems to be that for huge changes of the sextupole magnets they need time to reach their preset value.

^a RWTH Aachen University, Germany

Polarisation Lifetime Studies for EDM Measurements at COSY

M. Rosenthal^{a,b} for the JEDI-Collaboration

The spin motion of relativistic charged particles is described by the Thomas-BMT-equation:

$$\frac{d\vec{S}}{dt} = \frac{e}{\gamma m} \vec{S} \cdot \left[(1+G\gamma) \vec{B}_\perp + (1+G) \vec{B}_\parallel + \left(G\gamma + \frac{\gamma}{\gamma+1} \right) \frac{\vec{E} \times \vec{\beta}}{c} \right].$$

The spin vector \vec{S} is given in the particle rest frame, the electric and magnetic fields \vec{E} and \vec{B} in the laboratory frame. Latter is splitted into parts with respect to the momentum vector. In the shown expression only the interaction of the fields with the magnetic moment of the particle is shown. The parameter G is the anomalous magnetic moment. Considering this equation the vertical magnetic guiding field created by the COSY dipoles leads to an additional precession angle $G\gamma\theta$ with respect to the momentum vector rotation θ . In a magnetic storage ring the quantity $G\gamma$ is called the spin tune. Each particle within the beam possesses its own trajectory in phase space with a different path-length for one turn in the accelerator. Using a bunching rf cavity fixes the mean revolution time for one turn. This leads to a change of mean energy and thus a different spin tune for each particle. For a beam particles with initially aligned spin in the horizontal plane, the spin tune difference causes a spin decoherence over time and a polarisation loss as shown in Fig. 1. In these simulations deuteron beams with reference momentum $p = 970 \text{ MeV}/c$ were used and represented by a finite num-

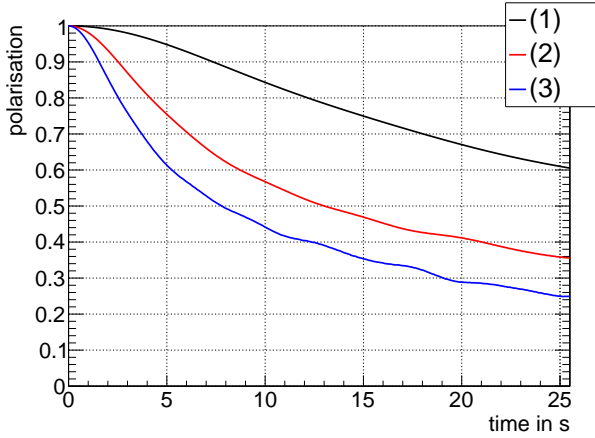


Fig. 1: Polarisation development for initially longitudinal polarised bunched deuteron beams of different sizes represented by 500 particles.

- (1): $\epsilon_x^{\text{rms}} = \epsilon_y^{\text{rms}} = 1 \text{ mm mrad}$, $(\frac{\Delta p}{p})^{\text{rms}} = 5 \cdot 10^{-5}$
- (2): $\epsilon_x^{\text{rms}} = \epsilon_y^{\text{rms}} = 3 \text{ mm mrad}$, $(\frac{\Delta p}{p})^{\text{rms}} = 1 \cdot 10^{-4}$
- (3): $\epsilon_x^{\text{rms}} = \epsilon_y^{\text{rms}} = 5 \text{ mm mrad}$, $(\frac{\Delta p}{p})^{\text{rms}} = 2 \cdot 10^{-4}$

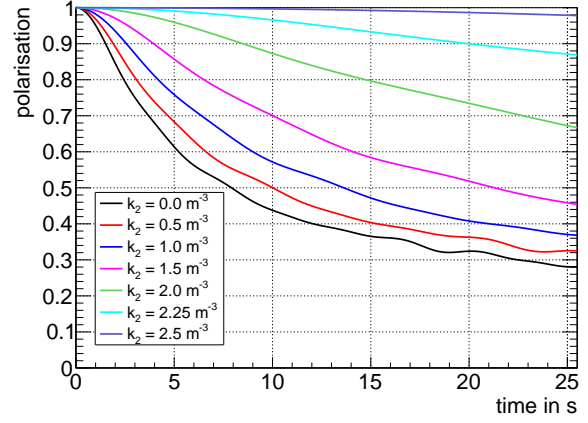


Fig. 2: Influence of sextupole corrections using different strength k_2 of the MXS family for an initially longitudinal polarised bunched deuteron beam with initial distributions according to $\epsilon_x^{\text{rms}} = 5 \text{ mm mrad}$, $\epsilon_y^{\text{rms}} = 0$, $(\frac{\Delta p}{p})^{\text{rms}} = 0$.

ber of particles. The initial distributions were randomly generated according to Gaussian distributions. The widths correspond to the normalized single particle emittances ϵ_x^{rms} , ϵ_y^{rms} and the momentum deviation of the particles $(\frac{\Delta p}{p})^{\text{rms}}$, respectively. Simulations allow to create beams, which consist of particles initially distributed in only one phase space dimension, to investigate phase space dimensions separately. A suitable way to correct for decoherence of the particles' spin are sextupole magnets, which influence the path-length changes. The three sextupole families (MXS,MXL,MXG) located in the arcs of COSY have been studied. Exemplarily the influence of the family MXS on a radial distributed beam is illustrated in Fig. 2. Spin tune aberrations to first order in $\frac{\Delta p}{p}$ are canceled using the rf cavity. Theoretically these three sextupole families are sufficient to correct for the spin tune aberrations, which are proportional to ϵ_x , ϵ_y and $(\frac{\Delta p}{p})^2$, respectively. In reality the accelerator stability over time is a further limiting factor.

A further field of interest is the influence of induced spin resonances on polarisation. For that purpose measurements and simulations utilizing a magnetic rf solenoid were performed. The resonance strength is defined as follows:

$$\epsilon = \frac{e}{p} \frac{1+G}{4\pi} \int B_\parallel dl.$$

The considered momentum of $p = 970 \text{ MeV}/c$ corresponds to a revolution frequency of about $f_{\text{rev}} = 750 \text{ kHz}$. The spin resonance frequencies of the time-varying solenoid field f_{sol} are given by:

$$f_{\text{sol}} = |(K + G\gamma)| \cdot f_{\text{rev}}, \quad K \in \mathbb{Z}$$

The parameter K represents different harmonics. In Fig. 3 (Fig. 4) the influence of different harmonics on polarisation lifetime for beams with radial (longitudinal) initial distributed particles is shown. In the latter case the choice of harmonic has a strong impact on the polarization damping time. This could be explained by the finite length of the particle bunch in longitudinal phase space. Some particles of the bunch arrive at the rf solenoid earlier than others and due to the time-varying field, they encounter different field strengths each turn. This leads to decoherence within the particle bunch. Theoretical calculations predict that this kind of decoherence vanishes at certain relations between machine parameters, solenoid harmonics and beam energies.

During the beam times in February 2013 and August/September 2013 a huge amount of data was collected. The analysis of this data is in progress. The timing information of recorded events allows to extract informations about the longitudinal particle distribution of the beam. In addition to the polarimeter data the transverse profiles of the beam were recorded occasionally. Taking these information into account it is possible to restrict the initial particle distribution of the beam in the simulations. Together with the recorded polarisation data using varius machine settings, this allows a benchmarking of simulation codes with measurements at COSY.

^a IKP FZJ, Germany

^b RWTH Aachen University, Germany

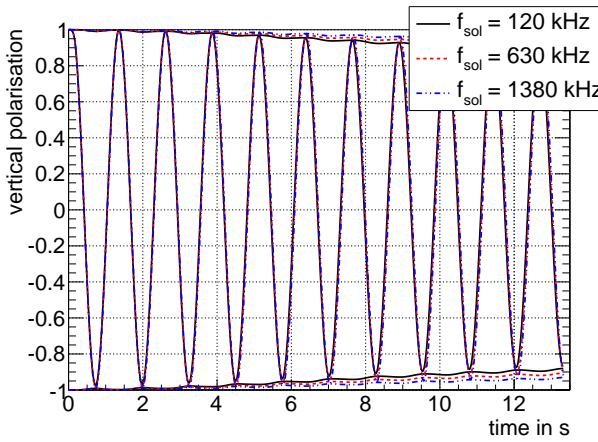


Fig. 3: Vertical polarisation oscillation and polarisation envelope with active rf solenoid ($\epsilon = 10^{-6}$) running on different resonance frequencies for an initially vertical polarised bunched deuteron beam with initial distributions according to $\epsilon_x^{\text{rms}} = 5 \text{ mm mrad}$, $\epsilon_y^{\text{rms}} = 0$, $(\frac{\Delta p}{p})^{\text{rms}} = 0$.

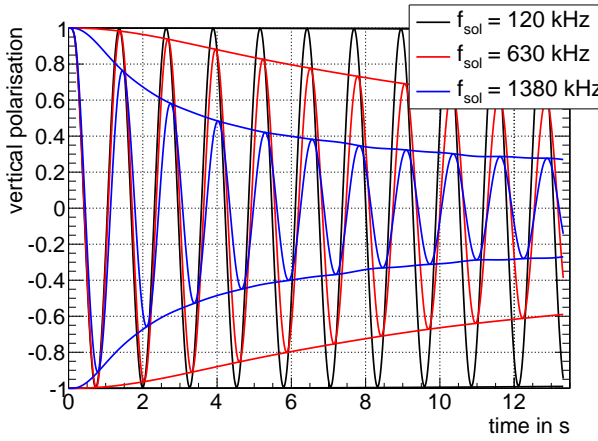


Fig. 4: Vertical polarisation oscillation and polarisation envelope with active rf solenoid ($\epsilon = 10^{-6}$) running on different resonance frequencies for an initially vertical polarised bunched deuteron beam with initial distributions according to $\epsilon_x^{\text{rms}} = \epsilon_y^{\text{rms}} = 0$, $(\frac{\Delta p}{p})^{\text{rms}} = 2 \cdot 10^{-4}$.

Matrix integration of ODEs for spin-orbit dynamics simulation

A. Ivanov^{a,b}, S. Andrianov^b, Yu. Senichev^a for the JEDI-Collaboration

The prototype of an IDE (Integrated Development Environment) for beam dynamics simulation is developed. Using this program one can compute not only the dispersion and betatron functions, etc., but also track the spin-orbit motion of charged particles. In the linear case transfer matrices are used. For the nonlinear dynamics matrix integration up to the necessary order and step-by-step integration are applied.

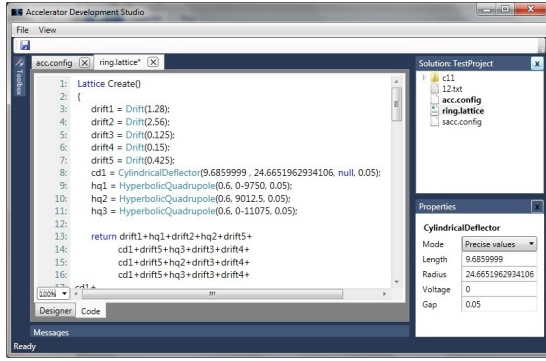


Fig. 1:
MODE GUI interface

The key functionality of the IDE in beam dynamics is to provide a high-level environment for accelerator design, simulation and analysis. Implementation issues are hidden from the users. If the selected method needs symbolic calculations or Taylor series expansion, they will process without direct user activity. On the other hand all information and model descriptions are available. So the researcher can be sure what exactly he calculates and how to interpretate the results.

The main approach that is used for simulation is a numerical implementation of matrix formalism. This method allows to represent an element of accelerator lattice by a set of the numerical matrices

$$X = R^1 X_0 + R^2 X_0^{[2]} + R^3 X_0^{[3]} \dots,$$

where X is a state vector of particle description. Note that the linear part R^1 is transfer matrix exactly, and matrix R^k is related to the non-linearities of order k . Moreover, it is possible to compute such accelerator parameter as the dispersion and betatron functions based on this matrix map elements. Multi-state dynamics is also proceeded in matrix form

$$[X^1 X^2 \dots X^N] = R^1 [X_0^1 \dots X_0^N] + R^2 [X_0^{1[2]} \dots X_0^{2[2]}] + \dots$$

In order to achieve the increase of performance one can generate computational code in different program languages

- C++ (with OpenMP);
- MATLAB (with Parallel Computing Toolbox);
- .NET Framework languages (with Parallel Extension).

```

1: Lattice Create()
2: {
3:   len = 9.68599;
4:   cd1 = CylindricalDeflector(len, 24.6651962934106,
5:   return cd1;
6: }
7: }
8: void OnElementCompleted(int elementID)
9: {
10:   // TO DO: describe the activities that will be run after each element of the lattice
11:   // elementID is an element indentifier
12: }
13: }
```

CylindricalDeflector(length, radius, **voltage**, aperture)
voltage: voltage in V at side of deflector

Fig. 2:
Autocomplete technology in the MODE

Table 1: Spin rotation oscillation, sec

Case	COSY Infinity	MODE
1. Cylindrical deflector		
$\delta T = 1 \cdot 10^{-4}$	5749,4	5749,0
$\delta T = 3 \cdot 10^{-4}$	635,6	635,5
$\Delta x = 0,003$	1184,3	1184,3
2. Cylindrical deflector $\times 16$		
$\delta T = 1 \cdot 10^{-4}$	5705,1	5704,6
$\delta T = 3 \cdot 10^{-4}$	633,9	633,8
3. Lattice with deflectors and quadrupole lenses		
$\delta T = 1 \cdot 10^{-4}$	0,2008	0,2008
$\delta T = 3 \cdot 10^{-4}$	0,0704	0,0704
$\Delta x = 0,003$	2072,3	2072,3
4. Lattice with deflectors, quadrupole lenses and RF		
$\delta T = 1 \cdot 10^{-4}$	4438,2	4415,3
$\delta T = 3 \cdot 10^{-4}$	492,9	491,7

The given approach is applied to the investigation of spin-orbit motion in an electrostatic storage ring. Particle dynamics is considered in 8-dimensional space. A state of dynamic system is described as $(x, x', y, y', S_x, S_y, \delta W, t)$ vector, where x, x' and y, y' are transverse and vertical displacement and velocity respectively; S_x, S_y are components of spin vector, W is Kinetic energy, t is time variable. Description of orbit motion is based on Newton-Lorentz equation. Spin dynamics is described by T-BMT-equation.

In the research the matrix methods for obtaining a map have been developed. Numerical matrix maps are built by a numerical step-by-step integration method. This approach allows to estimate map terms up to the necessary order of non-linearity and on a predetermined level of accuracy. The given technique have been tested on spin-orbit particles motion simulation in an electrostatic storage ring. The results are coincide with such numerical simulation tools as COSY Infinity and OptiM.

^a IKP FZJ, Germany

^b St. Petersburg State University, Russia

Upgrade of the Readout Electronics for the EDDA-Polarimeter

F. Hinder^{a,b}, B. Lorentz^a and J. Pretz^{a,b} for the JEDI collaboration

The readout electronics for the EDDA detector was upgraded by the installation of the general purpose VME board V1495 manufactured by CAEN. Figure 1 is a photograph of the new V1495 board. It consists of 194 IO channels and an onboard field programmable gate array (FPGA) which is programmable with a custom firmware. This single board can replace the existing programmable logic units (in total four boards) and the scaler modules (two boards). For tests the old electronics and the new V1495 board were installed and used in parallel.

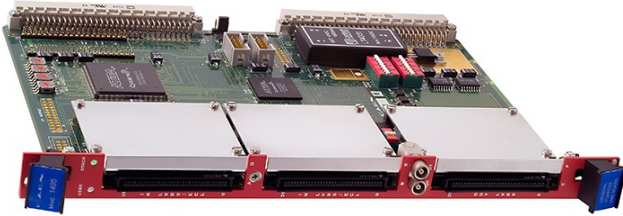


Fig. 1: New readout electronic board for the EDDA-Polarimeter.

The EDDA detector, built to study the inelastic proton-proton scattering, is nowadays used as an internal polarimeter at COSY. It consists of 32 bars and 2×16 semirings out of plastic scintillators, readout by photomultiplier tubes (PMTs). The bars cover the whole azimuthal angle Φ , the semirings measure the scattering angle θ in the range $9.9^\circ < \theta < 72.4^\circ$. The existing electronics combines only the signals in the semirings to measure the vertical polarisation of a stored particle beam. The new developed firmware, running on the FPGA, combines all informations of the detector elements and enables a measurement of the vertical and the horizontal polarization of the COSY beam. Furthermore, a differential measurement of the analysing power with respect to the scattering angle is possible by the new readout electronics. During the JEDI beamtime in July 2013 the V1495 module was installed. During this beamtime, simple tests with unpolarised deuterons were done.

A first measurement of a deuteron beam polarisation was done in September 2013. The vector polarisation of a deuteron beam was measured by steering the beam towards a carbon target. The polarisation of the beam lead to a left-right asymmetry for a vertical polarised beam. A horizontal polarised beam lead to an up-down asymmetry in the counted rates in EDDA. As an example of these measurements a Froissart Stora Scan, recorded by semiring 21, is presented in figure 2. The parameters of the fitted formula are: the analysing power A times the initial polarisation P_i , the resonance strength ϵ and the time of resonance crossing t_0 .

The fit delivers the initial polarisation multiplied with the

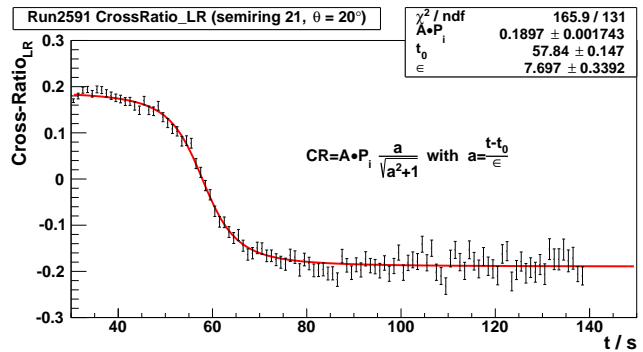


Fig. 2: Froissart Stora Scan, measured with semiring 21 ($\theta = 20^\circ$).

analysing power. These initial parameters, measured with 13 semirings are presented in figure 3. Due to the fact, that the measured polarisation is independent of the scattering angle, the the measured cross ratios are proportional to the analysing power of deuteron carbon scattering.

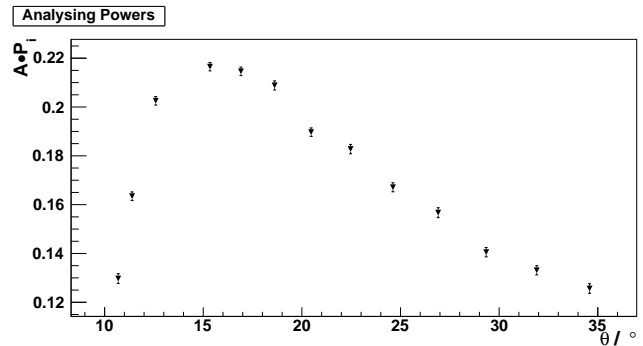


Fig. 3: Measured analysing power.

In conclusion, the developed firmware runs successfully on the onboard FPGA of the general purpose VME board. The upgraded readout electronics replaces the functions of the existing programmable logic units. In addition, the new system combines the signals of the semirings and the bars which allows a measurement of the horizontal polarisation apart from the vertical polarisation. The installed system is ready to use and features beam polarisation studies at COSY.

^a IKP FZJ, Germany

^b RWTH Aachen University, Germany

Orbit excitation investigations

S. Chekmenev^a for JEDI Collaboration

Since a permanent EDM of a particle lays along the direction of the spin, it can be observed by its small influence on the spin motion inside a storage ring. We plan to search for the presence of the EDM by looking into tiny changes of a spin tune of a polarized beam of deuterons or a change in polarization. In an ideal case a spin tune of a particle equals $G\gamma$, however there are different sources of systematic errors which can vary that original value and therefore mimic or spoil the signal from the EDM. Due to this fact, for the future charged hadron EDM experiment one should carefully study systematic errors arising from misaligned magnets, orbit lengthening, different types of extraction, etc.

In the real experiment one can create an orbit excitation with different amplitudes to study misalignment effects. This can be done by using steering magnets of COSY for example. I have been working on the implementation of this procedure in COSY Infinity for last couple of months. COSY Infinity is an arbitrary order beam dynamics simulation and analysis code. The first model had been created and it was decided to benchmark that with existing data. Linear drift of the spin tune was experimentally observed during our latest beam times in this and previous year. The drift can be explained by the extraction method. Each time the bunch were passing through the steerers the spin tune was gaining an additional kicks inside the steerers:

$$\frac{(1 + \mathbf{G} \cdot \boldsymbol{\gamma}) \int \mathbf{B} d\mathbf{l}}{B_0 \rho}$$

where $\int \mathbf{B} d\mathbf{l}$ is the integrated steerer field and $B_0 \rho$ is the magnetic regidity of COSY ring. Those kicks should have been compensated in quadrupoles between the steering magnets, nevertheless we suppose that full compensation didn't occur. The beam was continuously moved onto the target until fully extracted. For this purpose the strength of the magnets, and hence the beam deflection angle, slowly varied during a time interval of roughly 100 seconds, which caused a linear time dependence of the spin tune. The model demonstrates the same behavior (Fig. 1).

Unfortunately the numeric values didn't coincide with the experimental existing data. The problem was that in reality the second steerer bends back the beam to its original trajectory, but in COSY Infinity this process doesn't happen, and one can see the orbit is no longer closed. The horizontal phase space is drawn in Fig. 2.

Such situation appears, because of the difficulties with orbit description in COSY Infinity. One cannot simply produce a closed orbit bump at a certain point, it demands a bigger effort to realize that. As one can see in the picture, the model also gives the unrealistic horizontal emittance, which turns out to be larger than COSY acceptance. Hence, more detailed studies are needed to fix this problem or, perhaps a different type of spin tracking programs ought to be chosen.

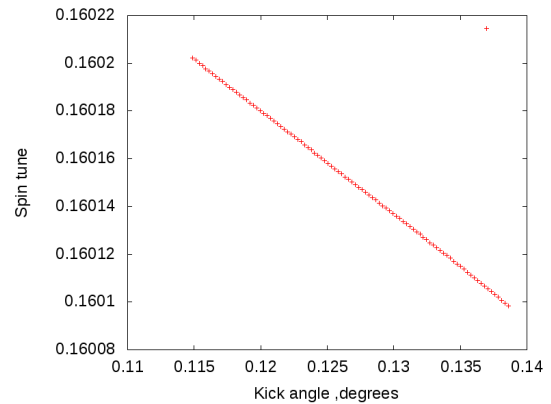


Fig. 1: Simulation of the spin tune drift caused by horizontal extraction at COSY. Initial momentum is 970 MeV/c, initial polarization is longitudinal, $G\gamma = -0.1609$.

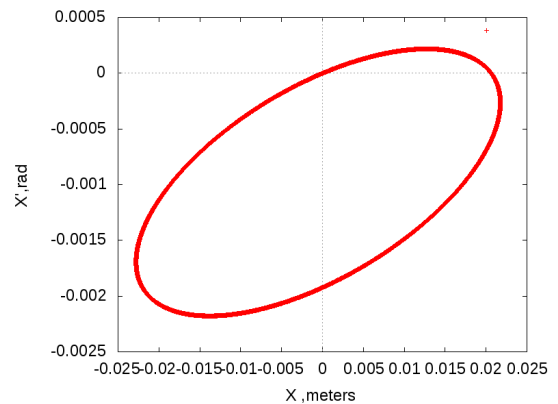


Fig. 2: Phase space ellipse in horizontal plane. Initial momentum is 970 MeV/c, initial polarization is longitudinal.

^a RWTH Aachen University, Germany

Modeling of Spin Depolarization in Electrostatic Rings on Supercomputer JUROPA

D. Zyuzin, Yu. Senichev*
for the JEDI collaboration

In purely electrostatic ring spin of “magic” particle rotates with the same angular frequency as the momentum and the vertical spin component S_y grows up due to the EDM. Spin dynamics described by T-BMT equation:

$$\begin{aligned}\frac{dS_x}{dt} &= \Omega_y S_z - \Omega_z S_y \\ \frac{dS_y}{dt} &= \Omega_z S_x - \Omega_x S_z \\ \frac{dS_z}{dt} &= \Omega_x S_y - \Omega_y S_x\end{aligned}$$

In purely electrostatic ring we have $\vec{B} = 0$ and $\vec{E} = \{E_x, 0, 0\}$ (if we do not have fringe fields). Then

$$\begin{aligned}\Omega_x &= -\frac{e}{m} \frac{\eta}{2} E_x \\ \Omega_z &= \frac{e}{m} \left\{ \left(\frac{1}{\gamma^2 - 1} - G \right) E_x \beta_y \right\},\end{aligned}$$

where β_y is vertical velocity, η — EDM factor, $d = \frac{\eta e}{4mc}$. Vertical spin component equation looks like

$$\frac{dS_y}{dt} = -\Omega_x S_z, \text{ and } \Omega_x = -\frac{e}{m} \frac{\eta}{2} E_x.$$

So, if we have horizontally polarized beam with $S_z \approx 1$ (or at least $S_z > 0$), we will observe S_y component due to the EDM signal. As soon as we lose horizontal polarization ($S_z < 0$ for part of the beam and $S_z > 0$ for the rest of the beam), accumulated S_y will decrease. Therefore, we need to have horizontally polarized beam long time enough to accumulate S_y that can be measured. In depolarized beam S_y component doesn't grow.

To be able to measure accumulated S_y component, we need SCT more than 1000 seconds.

Horizontal spin component equation:

$$\frac{dS_x}{dt} = \Omega_y S_z,$$

where

$$\Omega_y = -\frac{e}{m} \left(\frac{1}{\gamma^2 - 1} - G \right) \beta_z E_x.$$

If we will make $\Omega_y = 0$, we will get infinite SCT [1]. Unfortunately each particle has its own Ω_y , all spins rotate on different angles and polarization disappears after somewhat. Using JUROPA cluster at FZJ we made large scale simulation of EDM growth and spin depolarization. In the modelling we used 32768 particles with the following initial parameters: $\bar{x} = 0\text{mm}$, $\sigma(x) = 3\text{mm}$,

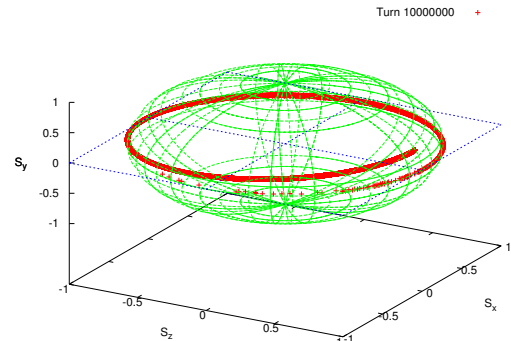


Fig. 1: Spin distribution of 32768 particles after 10^6 turns,
 $\eta = 10^{-9}$.

$$\begin{aligned}\bar{y} &= 0\text{mm}, \sigma(y) = 3\text{mm}, \frac{\Delta K}{K} = 0, \sigma(\frac{\Delta K}{K}) = 10^{-3}, \\ \bar{S}_x &= 0, \sigma(S_x) = 10^{-3}, \bar{S}_y = 0, \sigma(S_y) = 10^{-3}, \bar{S}_z = 1, \sigma(S_z) = 10^{-6}.\end{aligned}$$

Figure 1 shows 3D sphere with spin distribution with X , Y and Z axes. One can clearly see depolarization process in X – Z plane after 10^6 rotations and using different techniques [2] it is possible to decrease depolarization.

Beam depolarizes because of $\gamma \neq \gamma_{\text{magic}}$ [1]:

- $\frac{\Delta p}{p} \neq 0$.
- Initial offsets x , y (energy change depends on orbit lengthening due to initial distribution).
- Fringe fields influence (even reference particle changes its energy entering the deflector and leaving it).

The authors gratefully acknowledge the computing time granted on the supercomputer JUROPA at Jlich Supercomputing Centre (JSC).

References:

- [1] Yu. Senichev, A. Lehrach, R. Maier, D. Zyuzin, *The Spin Aberration of Polarized Beam in Electrostatic Rings*, Proc. of the 2nd International Particle Accelerator Conference IPAC'11, pp. 2175–2177, San Sebastián, Spain, 2011.
- [2] Yu. Senichev, R. Maier, D. Zyuzin, M. Berz, *Alternating Spin Aberration Electrostatic Lattice for EDM Ring*, Proc. of the 3rd International Particle Accelerator Conference IPAC'12, pp. 1332–1334, New Orleans, LA, USA, 2012.

*IKP FZJ, Germany

Spin Coherence Time Measurements at COSY

Greta Guidoboni

The spin coherence time measurements are part of the feasibility studies for a search for an Electric Dipole Moment (EDM) of charged particles. The proposed method for this experiment involves the use of a storage ring where the polarized charged particle beam can be kept circulating while interacting with a radial electric field. Starting with a longitudinally polarized beam, the EDM signal would be detected as a polarization precession starting from the horizontal plane and rotating toward the vertical direction. A long horizontal polarization lifetime, called spin coherence time (SCT), is required since it represents the time available to observe the EDM signal. At EDM sensitivity levels approaching 10^{-29} e·cm, the EDM signal would be a rotation on the order of 10^{-5} rad for a beam storage time of 1000 s.

In order to provide such a long SCT, an understanding of spin dynamics in the ring is crucial. The stable spin axis in a storage ring is along the vertical axis, orthogonal to the ring plane. As soon as a particle's spin moves away from the stable direction, it will start precessing around it with a frequency proportional to the relativistic factor γ of its motion and the local magnetic field. The number of spin precessions per turn around a storage ring is called the *spin tune*. Since particles in a storage ring have slightly different velocities, the spins will precess with different frequencies, spreading around in the horizontal plane and making the horizontal polarization shrink and vanish.

A direct measurement of the SCT was achieved at COSY in 2012 using a deuteron beam with a momentum of 0.97 GeV/c. It was possible to continuously measure the horizontal polarization as a function of time with the development of a dedicated data acquisition system¹ and a slow extraction of the beam onto a thick carbon target. The beam was bunched in order to remove in first order the momentum spread $(\Delta p/p)$ as a cause of the in-plane spin decoherence. The horizontal polarization lifetime was then limited only by second-order effects, such as emittance and $(\Delta p/p)^2$ from synchrotron motion.

The purpose of our experiment was to demonstrate that sextupole fields may be used to counteract the spread of spin tunes associated with second-order effects. Using cooling to first minimize the emittance and $(\Delta p/p)^2$ and then electric field white noise applied either in the vertical or the horizontal direction to increase the beam profile width separately, it was possible to examine decoherence effects one by one. The first result obtained in 2012 showed that the horizontal emittance contribution can be corrected by sextupole fields, as it is illustrated in Fig. 1 by the overlap of the zero crossings (largest SCTs) for each of three data sets. The best spin coherence time was larger than 200 s. The run in 2013 inve-

¹“Measuring the Polarization of a Rapidly Precessing Deuteron Beam” has been submitted to Physical Review Special Topics - Accelerators and Beams.

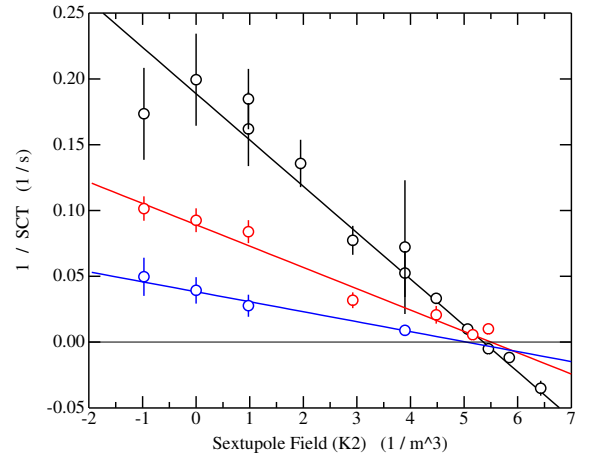


Fig. 1: Measurements of the reciprocal of the spin coherence time as a function of the sextupole magnetic field strength from the 2012 run. The three lines correspond to three different horizontal beam profile widths, starting from a narrow (bottom, blue) and going to a wide (top, black) profile. In order to determine whether this behavior is linear, all the points above the zero crossing at $5.4 \pm 0.1 \text{ m}^{-3}$ were reversed in sign.

stigated the possibility of finding multiple sextupole settings that in combination could minimize more than one source of decoherence. This study concentrated only on horizontal emittance and $(\Delta p/p)^2$ contributions from synchrotron oscillations. Vertical emittance effects were not considered since the required vertical acceptance is limited by the arcs of the COSY storage ring.

In order to prepare a beam with only a large horizontal emittance, the beam was bunched and cooled for 30 s, then heated for 1 s by applying white noise on electric field plates. For the polarization measurement, it was extracted onto a carbon target for about a hundred seconds. In a separate test, a large $(\Delta p/p)^2$ distribution was introduced by separately cooling for 30 s and then bunching the beam. In both cases, the polarization was rotated into the ring plane after roughly 40 s from the beginning of the beam manipulation in order to measure the time dependence of the horizontal polarization. In 2013 the tube-shaped carbon target was replaced by a ridge target in order to gain beam intensity.

A large set of data for the horizontal polarization as a function of time was recorded for several combinations of the two families of sextupole magnets: MXS, placed at the beginning of the arc section where the β_x function is the largest, and MXG, positioned in the middle of the arc section where the dispersion function D is the largest. MXS will preferentially correct for horizontal emittance effects and MXG for the $(\Delta p/p)^2$ contributions. The procedure developed to an-

alyze the data from the 2012 run and extract the spin coherence time is based on the use of template functions¹. A preliminary result similar to the reciprocal of the spin coherence time shown in Fig. 1 can be obtained from the initial slope of the falling horizontal polarization. This number was recorded for the various combinations of the sextupole magnetic fields and the beam setup (large emittance or large $(\Delta p/p)^2$). The measurements were organized into scans similar to Fig. 1 and the best (zero-crossing) SCT located for each scan. In the 2D plot shown in Fig. 2, the axes represent the MXG and MXS currents in percent of the power supply full scale. The blue points represent the best SCT measured in the case of a beam with large $(\Delta p/p)^2$ and the black points are the best SCT in the case of a large horizontal emittance. Since the two lines do not have a crossing point it means that we found no sextupole combination capable of correcting simultaneously for more than one source of decoherence.

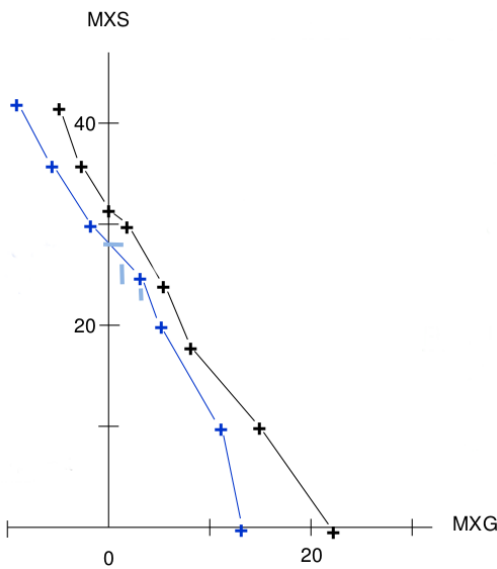


Fig. 2: 2D map of MXS and MXG where the units are a percent of power supply full scale. The blue points locate the best SCT values measured for a wide horizontal beam and the black points locate the best SCT values for a beam with a large $(\Delta p/p)^2$.

New issues were observed during the 2013 run that were not present in 2012. Fig. 3 shows two horizontal polarization profiles recorded with the same horizontal emittance but for different sextupole settings. The red points represent a typical behavior observed already in 2012 that was reproducible assuming that the spread of spin tunes is due solely to the particle path lengthening associated with a finite emittance of a bunched beam. The black points show a new feature, a double slope behavior. The data demonstrated that the later slope is almost featureless, falling at a constant fraction of the starting asymmetry. Instead, the initial slope depends on the sextupole setting or the amount of white noise (called “heating”) applied to increase the horizontal beam emittance (see Fig. 4). The larger the heating, the faster it decays. Not only

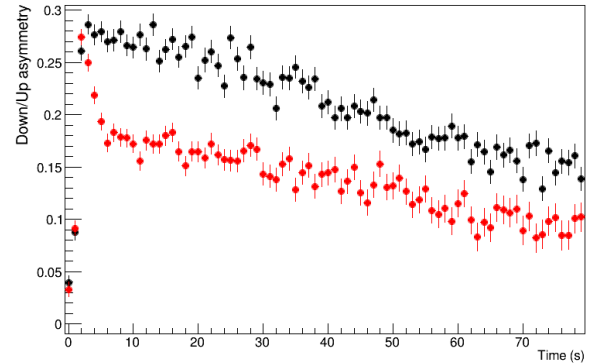


Fig. 3: Down/Up asymmetry (proportional to the horizontal polarization) as a function of time. These data represent a wide horizontal beam with two different settings of the sextupole fields. The red points were recorded with MXS=32% and MXG=0%; the black points with MXS=MXG=0%.

the heating but also the change of the machine tunes Q_x and Q_y could modify the depth of the first drop. This characteristic together with the observed “repolarization” after the first drop, might have a possible explanation in the crossing of a third order spin resonance. Another cause of the double shape behavior could be related to the special shape of the target. Another possible solution might be a non uniform heating of

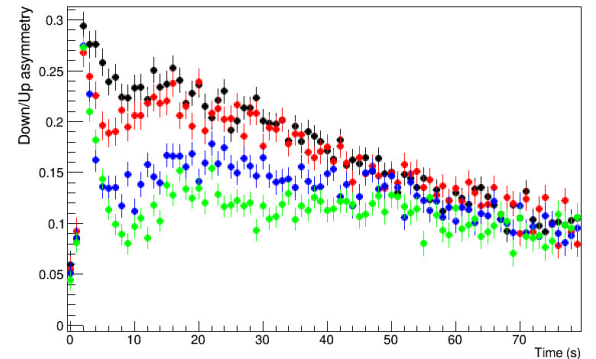


Fig. 4: The four lines shows the double-slope behavior as a function of the heating applied. Starting from the red data and progressing toward the green data, the heating and thus the horizontal profile of the beam increases. The larger the heating, the faster is the drop. The second drop is featureless since in all four cases the fractional decay rate is the same. The four sets of data were recorded with MXG=5% and MXS=0%

the beam which generates an external halo with a short SCT and a core with a longer SCT. The new ridge target could contribute in the extraction of different parts of the beam due to its shape.

The set of data collected in the case of a large $(\Delta p/p)^2$ did not show the double slope behavior. The dependence of the spin coherence time on $(\Delta p/p)^2$ is not clear yet but

most probably the emittance template curves will not work on this new set of data. The templates are based on an initial Gaussian distribution of spins in the horizontal plane but this assumption is not valid for the spin tune spread caused by $(\Delta p/p)^2$. The second order momentum spread comes from the synchrotron motion within the bunch which is described by the solution of a sinusoidal potential rather than a parabolic one.

The spin coherence time measurements started in 2012 clearly proved that sextupole fields are a powerful tool to increase the horizontal polarization lifetime. Because of the correlation between the decoherence sources ($(\Delta p/p)^2$ and emittance) and the best SCT values, it was not possible to find sextupole settings that could remove simultaneously these two contributions. Serious theoretical efforts are needed to understand the connections between these two sources of decoherence. New issues appeared in the SCT measurements with a wide horizontal beam. The origin of the double slope is an open question being addressed in ongoing offline analysis. Finally, it is crucial to understand the dependence of the spin coherence time on the second order contribution from the momentum spread in order to clarify how this decoherence source affects the spin coherence time.

Noise measurements at COSY

K. Grigoryev^a, H.-J. Krause^b, and H. Soltner^c for the JEDI collaboration

The future studies of the permanent electric dipole moment of the proton at COSY require development of high precision measurement tools, like beam current transformers (BCT), beam position monitors (BPM), and polarimeters. Extremely sensitive devices, like low-temperature SQUIDs, will increase the sensitivity of the measurement. These devices must be installed inside the vacuum pipe and have to be shielded not only from the room temperature, but also from the other noise source: circulating beam, vacuum environment, and surrounding electronics. In this case, the noise studies are obligatory.

First measurements of the noise at the COSY storage ring were carried out at the ANKE experimental area using a fluxgate for Hz–kHz range and two room temperature pick-up coils for different frequency ranges (500 windings for kHz–MHz range, 1 winding for MHz–GHz range). The fluxgate was installed outside of the vacuum, while both coils were in the vacuum at a distance of about 50 mm from the beam (see Fig. 1). The signals from coils and the fluxgate were amplified directly on the air side and processed with signal analyzers HP35665 and HP8596E. The spectra obtained during different stages of the beam formation at COSY were monitored online and stored on the PC for further analysis.

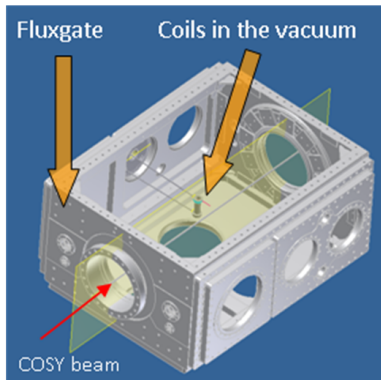


Fig. 1: Position of the fluxgate and pick-up coils at the ANKE target chamber.

Several attempts to look for noise in the measurement range were done during the JEDI run weeks in July and September 2013. During the first week several stable noise frequencies were identified:

- sharp signal up to -40 dBm at 2 Hz from cryo-pumps (strong signal, because one pump was installed directly on the target chamber);
- a wide range of the noise frequencies below -70 dBm

from different turbo-molecular pumps all over the COSY ring in the range of 300 – 1000 Hz;

- -80 dBm noise at 900 MHz induced on the BNC cables by the cellphone;
- -77 dBm (just 4 dBm above the background noise) noise from the circulating proton beam at 750 MHz. The frequency of the COSY beam for the current beamtime was 750 309 Hz;
- unknown -60 dBm noise at 323 MHz (it could be connected with specific configuration of memory and motherboard in one of PC around signal analyzers).

The noise frequencies obtained during the JEDI beamtime were reproducible and stable in time. Furthermore, it was possible to monitor decreasing of the COSY beam intensity during one cycle due to the beam-target interaction. Reduction of the number of particles in the ring from $2.9 \cdot 10^9$ to $1.2 \cdot 10^9$ during 3 minutes cycle, measured with COSY BCT, was similar to the change of the noise strength from -77 dBm to -80 dBm (see Fig. 2) measured at the beam frequency of 750 kHz.

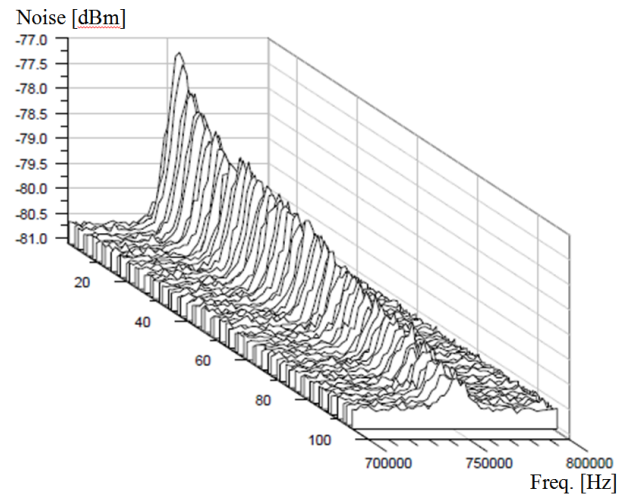


Fig. 2: Dependence of the beam intensity on the noise strength at 750 kHz during one cycle.

Low beam energy of the JEDI beamtime does not allow to discover the most challenging noise for all kind of experiments. When the beam energy was higher than some threshold (about 700 MeV/c) the 50 Hz noise up to 1 dBm was dominating (see Fig. 3). A problem with grounding loop at one of the steerer power supplies was solved by the accelerator crew. During the next JEDI beamtime in September 2013, the 50 Hz problem was not present during COSY operation

at different beam energies, but was back in stand-by mode. It means, there are more problems to identify and solve for the future experiments.

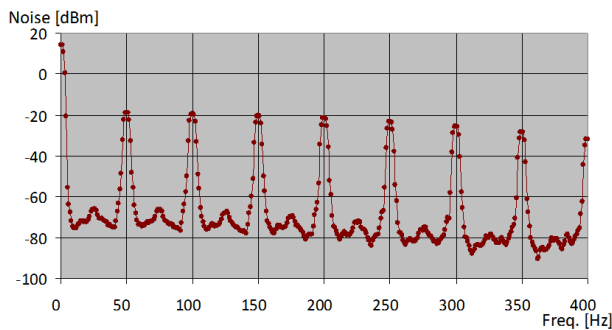


Fig. 3: 50 Hz noise at the middle energy of COSY.

^a Physikalisches Institut III B, RWTH Aachen University, Aachen, Germany

^b Peter Grünberg Institute / Institute of Complex Systems (PGI-8/ICS-8), Forschungszentrum Jülich, Germany

^c Zentralinstitut für Engineering, Elektronik und Analytik (ZEA-1), Forschungszentrum Jülich, Germany

Systematic error studies of storage ring EDM searches at COSY using an RF Wien filter, and the dependence of the beam polarization on the harmonics of a radio-frequency spin rotator*

A. Saleev^a for the JEDI collaboration

Future experiments to search for proton and deuteron electric dipole moments (EDMs) in a conventional magnetic storage like COSY will employ E/B -fields to drive the EDM-induced spin precession. One of the options is the use of a so-called radio-frequency (RF) Wien-filter. It exerts zero Lorentz force on the beam, is EDM-transparent, but rotates the magnetic dipole moment (MDM) of the beam particles and generates a frequency modulation of the spin tune. This modulation causes a coupling to the EDM precession in the constant motional electric field of the machine, which would allow one to accumulate the EDM signal on resonance.

The troubling issue is that, alongside with the radial motional E -field, the so-called imperfection, radial and longitudinal B -fields from misaligned magnets abound in the ring. The RF Wien-filter frequency modulation of the spin tune couples the MDM to the magnetic field imperfections in precisely the same manner as the EDM couples to the motional electric fields in the machine, therefore imperfection magnetic fields emerge as one of the principal sources of systematic background to the EDM signal.

The challenge one faces is to disentangle the true EDM signal from the MDM induced signal and to compensate for imperfection fields.

Another option is the use of an MDM-transparent RF spin flipper in which the B -field is compensated for by the motional E -field. In this case, the resulting EDM rotation of the spin is free of background from imperfection fields, but unfortunately, this combination of the E/B fields excites unwanted coherent betatron oscillations.

During the upcoming JEDI beamtime the role of imperfection fields at COSY will be investigated. Two static solenoid magnets, each located in one of the straight sections, will mimic the imperfection fields. Fine tuning the imperfection strength and the spin kicks, one would minimize the spin tune $v_s = G\gamma$ (G is the anomalous magnetic moment, and γ the relativistic Lorentz factor). Modification of the spin tune by two local imperfections with spin kicks χ_1 and χ_2 , is given by $v_s = \frac{1}{\pi} \arccos [\cos(\pi G\gamma) \cos(\frac{\chi_1}{2}) \cos(\frac{\chi_2}{2}) - \sin(\frac{\chi_1}{2}) \sin(\frac{\chi_2}{2})]$. More realistically, for non-vanishing intrinsic ring imperfections, the saddle point of the surface shown in Fig. 1 is located off the origin of the $\chi_1 - \chi_2$ plane. Studies at COSY show that the spin tune can be measured to an accuracy of 10^{-9} , which provides a suppression of the imperfection strength to the level of 10^{-6} .

An important issue for all RF spin resonance approaches is the spin decoherence caused by synchrotron oscillations. The idea by Lehrach, Lorenz, Morse, Nikolaev, and Rathmann is to fine tune the harmonics of the RF field and the beam energy. Specifically, one could compensate decoherence effects from the phase slip in the idle precession of the horizontal spins and from the phase slip of the RF spin rotator due to

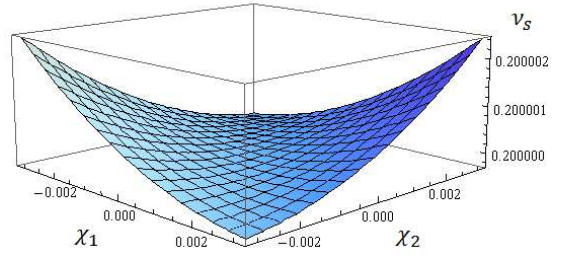


Fig. 1:

Spin tune map produced by two solenoids with spin kicks χ_1 and χ_2 for deuterons at $T = 747$ MeV, and an unperturbed spin tune of $G\gamma = 0.2$.

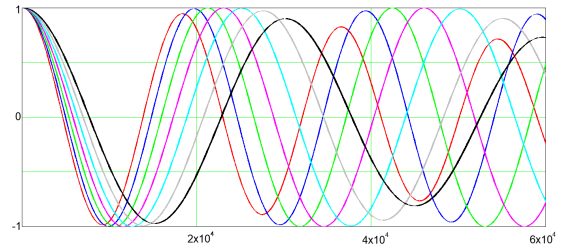


Fig. 2:

Simulation of the EDM resonance with RF Wien filter of harmonic $K = 1$ for vertically polarized deuterons as function of turn number, for different energies $T = 1000$ and 1700 MeV, showing that near $\simeq 1300$ MeV (green, magenta, and cyan), spin decoherence is suppressed ($C_{SD} \simeq 0$).

the time of arrival at the RF field. A crucial point is that both phase slips are of common origin. Analytical and numerical calculations confirm that one could enhance the spin coherence time when the harmonic number K and the slip factor η satisfy the condition

$$C_{SD} = 1 - \frac{\eta}{\beta^2} \left(1 + \frac{K}{G\gamma} \right) = 0,$$

β and γ denote the relativistic Lorentz factors of the beam. Tests performed during the JEDI September 2013 run with a deuteron beam at a momentum of 970 MeV/c with an RF solenoid showed that damping of vertical polarization oscillations depends on the harmonic number K of the RF-solenoid (see Fig. 2).

^a Institut für Kernphysik, Forschungszentrum Jülich, Germany, and Landau Institute, Chernogolovka, Russia.

* supported by the COSY-FFE program under contract number COSY-125.

Machine Development for Spin-filtering Experiments at COSY

C. Weidemann for the PAX collaboration

During the past years the PAX collaboration identified spin filtering based on the spin-dependent part of the nucleon-nucleon interaction as the most promising method to produce a first intense beam of polarized antiprotons for the future FAIR facility [see PAX Collaboration Technical Proposal at http://collaborations.fz-juelich.de/ikp/pax/public_files/proposals/techproposal20060125.pdf]. The successful spin-filtering experiment in 2011 with a transverse polarized hydrogen target at COSY [W. Augustyniak et al. Phys. Lett. B 718, 64 (2012)] experimentally proved spin filtering as viable method for proton beams and confirmed the present theoretical understanding of the mechanism.

The polarization build-up in the stored, circulating beam due to the spin-dependent removal of particles as function of time is given by

$$P(t) = \frac{N^\uparrow(t) - N^\downarrow(t)}{N^\uparrow(t) + N^\downarrow(t)} = \tanh\left(\frac{t}{\tau_1}\right) \approx Q d_t f \tilde{\sigma}_1 \cdot t, \quad (1)$$

where N^\uparrow (N^\downarrow) denote the number of beam protons with spin orientation parallel (antiparallel) to that of the target spins. In order to maximize the achievable beam polarization the target nuclear polarization Q and the areal target gas density d_t have to be large. The beam-revolution frequency f is determined by the beam momentum and the ring circumference. The effective polarizing cross section $\tilde{\sigma}_1 = \sigma_1(\Theta > \Theta_{\text{acc}})$ depends on the machine acceptance as well as the beam lifetime τ_b , which has to be sufficiently long to achieve reasonable polarizations.

H^0 atoms in a single hyperfine-state, prepared by an atomic beam source, are injected into a thin-walled storage cell, which forms the interaction region of beam and target. The utilization of a storage cell of $d = 9.6$ mm diameter and $l = 400$ mm length on the one hand increases the areal density of the polarized gas target by about two orders of magnitude, but on the other hand restricts the machine acceptance and thus reduces the beam lifetime. Given that single Coulomb scattering is the dominating particle loss mechanism and assuming small acceptance angles Θ_{acc} (typically 1 – 10 mrad) the beam lifetime is proportional to Θ_{acc}^2 and thus inversely proportional to the betatron function $\beta_{x,y}$ ($\tau_b \propto \Theta_{\text{acc}}^2 \propto \beta_{x,y}^{-1}$). Decreasing the β -function at the location of the target by about one order of magnitude and thereby improving the beam lifetime was realized by the installation of a low- β section around the target, which comprises two pairs of additional quadrupole magnets. Determining the achieved β -functions at the position of the magnets was accomplished by a measurement of the working point Q as function of the focusing strength of a quadrupole [C. Weidemann, Ph.D. thesis, University Cologne (2011), available from http://collaborations.fz-juelich.de/ikp/pax/public_files/theses/thesisCh.Weidemann.pdf].

The reasonable agreement of the measurement at the magnet position with model calculations (see Fig. 1) confirms that β -functions of $(\beta_x, \beta_y) = (0.38 \text{ m}, 0.36 \text{ m})$ are achieved at the center of target region. The machine acceptance angle and the beam widths at the target were determined using a dedicated movable frame system [K. Grigoryev et. al. Nucl. Instrum. Meth. A599, 130 (2009)]. The acceptance

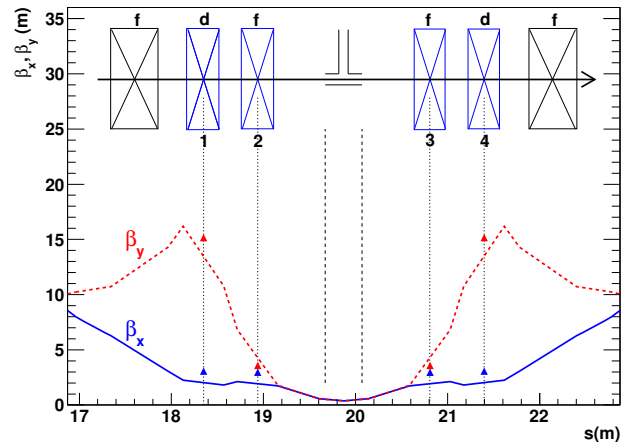


Fig. 1: Model calculation of the β -functions at the PAX-TP and measured values of β_x and β_y at the magnet positions. In blue the four new PAX quadrupole magnets are indicated, where magnet 1 and 4 form the defocusing (d) pair and magnets 2 and 3 are the focusing (f) pair. In addition the storage cell and the beam direction are shown.

angle amounts to $\Theta = (6.13 \pm 0.17)$ mrad, and the beam widths to $(2\sigma_x, 2\sigma_y) = (1.07 \pm 0.01 \text{ mm}, 1.13 \pm 0.01 \text{ mm})$. With the achieved β -functions, the horizontal and vertical 2σ beam emittances were $\epsilon_x = (1.86 \pm 0.06) \mu\text{m}$ and $\epsilon_y = (2.82 \pm 0.07) \mu\text{m}$.

Since single Coulomb scattering is the dominating particle loss mechanism special care of the vacuum conditions was taken. The installation of a sophisticated pumping system in and around the target chamber together with flow limiters at the entrance and exit of the chamber provided very satisfying residual gas conditions. The beam lifetime caused by the target region with an injected gas flow of $3.3 \cdot 10^{16} \text{ H}^0/\text{s}$ contributed by only one third to the total beam lifetime of $\tau_b = 8000 \text{ s}$, while the contribution of the machine itself is twice as large.

Operating the strong quadrupoles of the low- β section requires orbit correction as well as a good setting of the working point. Both procedures showed significant improvement of the beam lifetime and became standard tools to set up a beam for spin-filtering experiments. Besides the regular adjustment of the electron cooler to provide phase-space cooling, it was found that tilting of the electron beam with respect to the proton beam improved the beam lifetime by about 50%. This space-charge effect could be explained by a betatron amplitude-dependent detuning or tune spread. For large tune spreads caused by a small beam emittance, more betatron resonances in the tune diagram are covered.

The interplay of the investigations presented here fulfilled the demanding beam conditions for the first spin-filtering experiment at COSY. The presented results comprise a recipe about how to set up a beam for spin filtering experiments in a storage ring.

More information about the experimental setup and the results of the spin-filtering experiment have already been presented in recent annual reports.

Construction of a test station for beam current measurement devices

S. Kirfel¹, S. Mikirtychians^{1,2}, R. Schleichert¹, and Yu. Valdau^{1,3}, for the PAX collaboration

A Time Reversal Invariance test is planned at COSY (TRIC) as a transmission experiment [1]. In this experiment, a polarized proton beam will interact with a tensor polarized deuterium gas target. The total cross sections of the normal and time-mirrored reactions are compared using a T-odd P-even null observable $A_{y,xz}$. The time-mirrored situation in this experiment is realized by flip of the polarization direction either of beam or target. The number of protons circulating in the accelerator decreases due to interaction of the beam with the target. A beam current change will be determined using a high precision beam current measurement system. The slope of this decrease determines the total cross-section asymmetry $A_{y,xz}$, which is a genuine T violation observable. Thus, the development of a high precision beam current measurement system is mandatory for realization of the TRIC experiment. To test a performance of different devices, suitable for the beam current measurement, and their response on a different shape of bunches and beam positions, a dedicated test station has been designed and constructed. Three different measurement devices, available at COSY, are implemented into the test station:

- A standard COSY Beam Position Monitor (BPM) [2] integrated into an 854 mm long standard COSY steel tube. Usually BPMs are used for the beam position determination, but, in principle, they can also be used for the beam current determination.
- The Parametric Current Transformer (BCT) [3] is a toroidal detector with an inner diameter of 184 mm. A copy of this device is used at COSY for the beam current determination.
- The Integrating Current Transformer (ICT) [4] is also a toroidal detector with an inner diameter of 122 mm. This device has been used at the extraction line of COSY for the bunched beam current determination.

The BPM represents a basic tube of the test station (see Fig. 1). The BCT is mounted directly to the BPM tube. Due to the smaller diameter of the ICT, it is fixed to an extension tube with an outer diameter of 104 mm. The tubes are connected by welded steel CF flanges at both sides of the tube. This enables an easy extension of the test station and can provide a vacuum tightness in case it is necessary in future. The support of the test station consists of standard aluminum profiles with a squared base and a side length of 50 mm. These profiles are fixed by screws, which makes them easily adaptable to changing conditions.

A 50 μm thick gold plated tungsten wire alloyed with 3% rhodium [5] simulates the particle beam. The wire is straightened inside the tube by a permanent weight, which is connected to it by a fishing line. The conducting wire is positioned between two windings of a 0.5 mm thick enameled copper wire, which is wound around one of the axis of the tension system. The second axis in the tension system is used for redirecting a vertical gravitation force, using a fishing line, in to the horizontal direction. This method of conductive wire positioning is very simple, reliable and does not require precise machining.

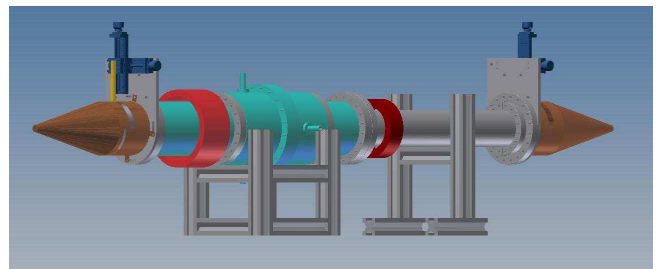


Fig. 1: The test station for the beam current measurement devices. It incorporates three different beam current measurement devices: BPM (cyan blue), BCT (light red), and ICT (dark red). A wire inside the tube is moved using a XY tables (blue) mounted on both sides of the system. The wire tension system is covered inside the tapers (copper colored)

In order to enable a movement of the wire in the tube, an aluminum bar connects the tension system to XY-tables on both sides of the station Fig. 1. The XY-tables are installed vertically with the help of aluminum plates fixed to the flanges at the tube ends. Each XY-table consists of two linear stages LT45-110 from OWIS [6].

The precision of the wire position mainly depends on three factors: wire tolerances, wire catenary and precision of the XY-tables. The tolerances of the conducting wire [5] and the copper wire [6] cause a tolerance $\Delta_h = 26\mu\text{m}$ and $\Delta_v = 18\mu\text{m}$ in horizontal and vertical direction, respectively. Using a weight of 400 g, used in the tension system, and a self-weight of the wire of 4×10^{-5} kg/m [5], the maximum catenary for the conductive wire is estimated to be $\Delta_{max} = 32\mu\text{m}$ [7]. A position precision of the XY-tables is $\Delta_{XY} = 10\mu\text{m}$ [6]. The resulting tolerance of the horizontal wire positioning is $\Delta_{h,total} = \Delta_h + \Delta_{XY} = 36\mu\text{m}$, while the tolerance of the vertical wire positioning is $\Delta_{v,total} = \Delta_v + \Delta_{max} + \Delta_{XY} = 60\mu\text{m}$. The test station is readout using DAQ from the ZEA and can be easily implemented into any of the DAQs at COSY. Main parts of the test station are compatible with a vacuum, hence in case it is necessary, it can be upgraded to have a vacuum inside. Due to the use of the CF flanges in all the connections, the test station can easily be extended to accommodate new devices. The test station can also be used to study the performance of standard COSY-BPM's, as well as study of possible new BPM prototypes which are in preparation for the JEDI experiment.

References:

- [1] P.D. Eversheim, B. Lorentz and Y. Valdau, COSY Proposal #215
- [2] KFKI-MSzKI, Department of Laboratory Automation, Budapest, Project Cosy Beam Position Monitor (1992).
- [3] J. Bergoz, Crozet, France, Parametric Current Transformer KFA-Jülich, Instruction Manual (1989).
- [4] Bergoz Instrumentation, Beam charge Monitor Integrate-Hold-Reset, User Manual, rev. 1.8.1 (2010).
- [5] Luma Metall AB, Kalmar, Sweden, URL <http://bamboo.pv.infn.it/2007-02/ref/Luma-Cat.pdf>

- [6] Owis GmbH, Staufen, Germany, URL http://www.owis.eu/fileadmin/user_upload/owis.eu/products/pdf/03_Man_Pos_kapitel_web_01.pdf
- [7] S. Holler, C. Butenweg, E. Hake (2005), Baustatik in Beispielen, Berlin, Heidelberg: Springer-Verlag

¹ Institut für Kernphysik, Forschungszentrum Jülich, 52425 Jülich, Germany

² High Energy Physics Department, Petersburg Nuclear Physics Institute, 188350 Gatchina, Russia

³ Helmholtz-Institut für Strahlen- und Kernphysik, Nussallee 14-16, D-53115 Bonn, Germany

Analysing powers of the $\vec{d}p \rightarrow \vec{d}p$ reaction at 1.2 and 2.27 GeV*

D. Mchedlishvili^{a,b}, A. Kacharava^a, and C. Wilkin^c for the ANKE collaboration

The vector and tensor analysing powers of the $\vec{d}p \rightarrow \vec{d}p$ reaction were evaluated using the ANKE data from the 2006 beam time. The main purpose of this experiment was to measure the deuteron charge-exchange process on hydrogen, though useful data were obtained on various other reactions including the deuteron-proton elastic scattering. Measurements were performed using eight different configurations of the polarised ion source at COSY. The deuteron beam was prepared at two energies, $T_d = 1.2$ and 2.27 GeV. Several measurements of the analysing powers of the $d p$ elastic process exist close to 1.2 GeV. These include old ANKE measurements at 1170 MeV, Saturne at 1198 MeV and Argonne at 1194 MeV. New ANKE results at 1.2 GeV are in good agreement with that obtained from these experiments. This therefore provides a check of the COSY beam polarimetry. Despite the fact that the COSY ion source was not optimised to measure the $\vec{d}p \rightarrow \vec{d}p$ reaction, polarised states were successfully combined in a way to measure the A_y and A_{yy} separately (see details in the ANKE internal report).

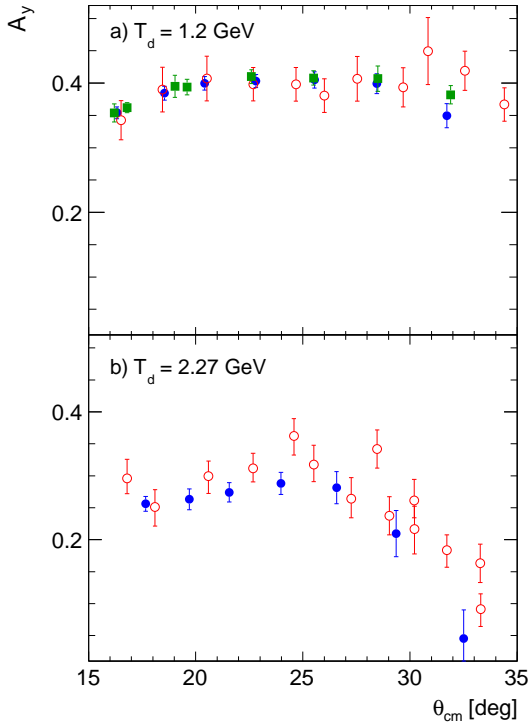


Fig. 1:

Vector analysing power of the $\vec{d}p \rightarrow \vec{d}p$ reaction at two energies. New results (points) are compared with existing measurements at close energies including Argonne at 1194 and 2000 MeV (circles) and ANKE at 1170 MeV (squares).

Results are presented in Fig. 1 and 2 as functions of deuteron θ_{cm} angle together with other data, obtained at close en-

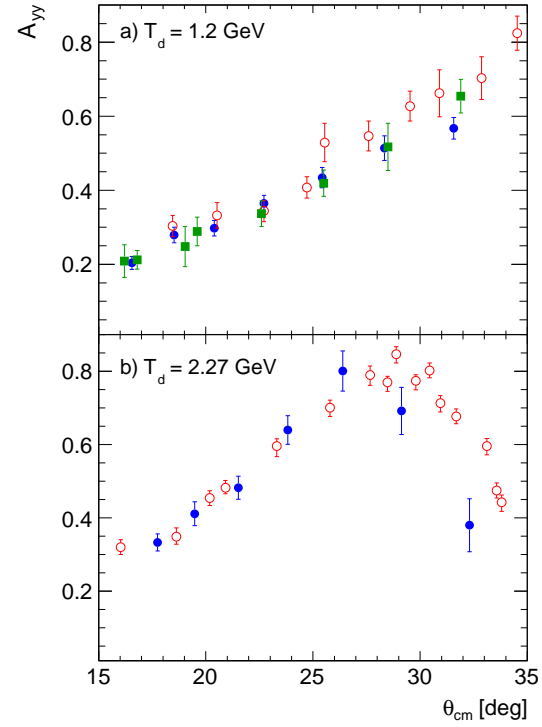


Fig. 2:

Tensor analysing power of the $\vec{d}p \rightarrow \vec{d}p$ reaction at two energies. New results (points) are compared with existing measurements at close energies including Argonne at 1194 and 2000 MeV (circles) and ANKE at 1170 MeV (squares).

ergies. The vector analysing power signal at 2.27 GeV is significantly smaller than at 1.2 GeV, and is also smaller than that measured at Argonne at 2 GeV. This is in agreement with Argonne data at 1.2, 1.6 and 2 GeV, that clearly show a dilution of the vector analysing power signal as energy increases. Due to a very asymmetric acceptance of the ANKE forward detector it was not possible to measure the A_{xx} analysing power with reasonable accuracy. Hence, only the A_{yy} was obtained. Similarly to A_y , the new results for A_{yy} well agrees with existing data at 1.2 GeV. At 2.27 GeV, the difference from the Argonne data at 2 GeV is negligible, at least up to 27° in CM, if the error bars are taken into account. It should be noted, that the zero-crossing point tends to move towards the smaller angles as energy increases. This effect can be easily observed in the Argonne data at 1.2, 1.6 and 2 GeV, and by new ANKE results.

^a IKP FZJ, Germany

^b HEPI Tbilisi State University, Georgia

^c University College London, U.K.

* supported by the COSY-FFE program

First results on A_y analyzing power measurements in $\vec{p}p$ elastic scattering experiment*

Z. Bagdasarian^{a,b}, S. Barsov^c, D. Chiladze^{a,b}, S. Dymov^{a,d}, A. Kacharava^a, G. Macharashvili^{b,d}, D. Mchedlishvili^{a,b}, S. Merzliakov^{a,d}, S. Mikirtychyants^{a,c}, N. Lomidze^b, M. Tabidze^b, S. Trusov^a, R. Schleichert^a, H. Ströher^a, and C. Wilkin^e for the ANKE collaboration

The ANKE beam time in April 2013 was proposed to investigate nucleon-nucleon (NN) interactions [1]. The polarized beams and targets at COSY-ANKE facility allow a substantial contribution to the existing database by measuring various observables for both proton-proton (pp) and proton-neutron (pn) systems. The experiment was carried out at ANKE using a transversely polarized proton beam incident on an unpolarized hydrogen (for pp investigations) or deuterium cluster-jet target (for pn studies). Six beam energies of $T_p = 0.796, 1.6, 1.8, 1.965, 2.157$ and 2.368 GeV were used. The aim of this contribution is to report on the preliminary results for the analyzing power A_y of the pp elastic scattering at the above mentioned kinetic energies in the $4^\circ < \theta_{cm} < 29^\circ$ scattering angle range. θ_{cm} will be referred to as just θ in the following.

The scattered protons were detected at the ANKE spectrometer using the **Forward Detector** (FD) and two **Silicon Tracking Telescopes** (STT) placed symmetrically around the cluster target. FD comprises one drift chamber, two multi-wire proportional chambers and three-plane scintillation hodoscopes, consisting of the vertically oriented counters (8 in the first plane, 9 in the second and 6 in the third one). Each STT consists of three layers of the double-sided micro-structured silicon strip detectors, that are placed close to the target inside the vacuum chamber. These layers (1st layer: 70 μm thick, 2nd- 300 μm and 3rd - 5000 μm) were placed 2.8, 4.6 and 6.2 cm away from the target, covering laboratory angles $75^\circ < \theta_{lab} < 140^\circ$. Data at ANKE was taken with the following triggers: STT alone and in coincidence with FD.

The criteria for pp elastic process identification were based on the missing mass and the scattering angle reconstruction. For the protons that passed the third layer of the STT system, the kinetic energy was reconstructed using the neural network method [3]. The proton scattering angle used in the analysis was calculated from its kinetic energy, because the geometrical angle is measured with larger uncertainties.

In order to make use of the so-called cross-ratio method [4], the beam polarization was reversed for every subsequent cycle. This technique allows to eliminate first-order systematic errors. Forming the geometrical means of the yields to the left $L = \sqrt{L_1 L_2}$ and to the right $R = \sqrt{R_1 R_2}$ with respect to the beam polarization direction, the asymmetry and its statistical uncertainty are estimated as

$$\varepsilon(\theta) = \frac{L(\theta) - R(\theta)}{L(\theta) + R(\theta)} = P \langle \cos \phi \rangle A_y(\theta) \quad (1)$$

$$\sigma_\varepsilon(\theta) = \frac{LR}{(L+R)^2} \sqrt{\frac{1}{L_1} + \frac{1}{L_2} + \frac{1}{R_1} + \frac{1}{R_2}} \quad (2)$$

in each θ scattering angle interval. P denotes the beam polarization. Hence, the analyzing power A_y is calculated as

$$A_y(\theta) = \frac{\varepsilon(\theta)}{P \langle \cos \phi \rangle} \quad (3)$$

with the uncertainty

$$\sigma_{A_y} = \sqrt{\left(\frac{\sigma_\varepsilon}{\varepsilon}\right)^2 + \left(\frac{\sigma_P}{P}\right)^2} \quad (4)$$

The details on the estimate of the second-order systematic uncertainties are given in the ANKE report [3] and it is concluded that they are negligible for the final result.

As seen from Eq. 3 besides asymmetry calculation, one essential point for the analyzing power measurement was the determination of the absolute beam polarization. That was achieved by using the EDDA (Excitation Function Data Acquisition Designed for Analysis of Phase Shift) detector.

The EDDA experiment was conceived to provide high-precision elastic-scattering data in the COSY energy range (0.5-2.5 GeV) [6], but later has been modified to be used as the internal polarimeter. The thick carbon fiber target was inserted into the EDDA section for the last 20 seconds of each 3-minute COSY cycle. The EDDA detector is comprised of the long scintillator bars, that run parallel to the beam and the scintillator rings. Each of the ring-shaped scintillators of the EDDA detector cover a fixed polar angle range. Hence it is possible to compare count rates in the left and right semi-rings for each θ_{lab} range, while averaging over ϕ in every semi-ring. The details on the validity of that scalar method are given in [5].

The $p - {}^{12}\text{C}$ -inclusive measurements let us obtain the beam polarization from the correlated trigger rates, without the full reconstruction of the events. The kinematic trigger makes a rough check whether the protons are elastically scattered ones. The triggers are generated for each semi-ring and counted in the so-called scalers. The time-marking system uses a clock to provide a precise time for each event trigger. The effective analyzing powers for the individual scintillator rings, measured earlier by the EDDA-collaboration were used in our analysis.

The polarization was measured individually in each pair of the semi-rings, and then using the independence of the

polarization on the polar angle, the weighted average is presented as the final result for P .

$$P = \sum_{i=1}^n \frac{P_i}{\sigma_i^2} / \sum_{i=1}^n \frac{1}{\sigma_i^2} \quad (5)$$

with the statistical uncertainty

$$\sigma_P^2 = 1 / \sum_{i=1}^n \frac{1}{\sigma_i^2} \quad (6)$$

where i is the ring number. The beam polarization systematic uncertainties, estimated up to 5% [5] dominate the analyzing power result uncertainties.

Preliminary results for the analyzing power at all the six energies are shown in Fig. 1 along with the existing experimental data and the SAID (Scattering Analysis Interactive Dial-in) predictions [2]. The error bars of our data points show the statistical uncertainties only. The analysis of the data from Forward Detector is still in progress. The good agreement between the data from previous experiments and our results at 796 MeV serves as an additional confirmation of the validity of our measurements. Moreover, such a close coincidence to the data of the other experiments indicates that actually the systematic uncertainty in P measurement by EDDA is probably less than 5%. Our results greatly extend the existing experimental data: analyzing power for pp elastic scattering has been measured for the first time in the $T_p = 1.6 \div 2.4$ GeV beam kinetic energy and $4^\circ < \theta < 24^\circ$ angular range.

References:

- [1] Z. Bagdasarian et al, *COSY Proposal #212* (2012); available from http://collaborations.fz-juelich.de/ikp/anke/proposal/prop2012_v4.pdf
- [2] *SAID data base*
available from <http://gwdac.phys.gwu.edu>
- [3] G. Macharashvili, *ANKE internal report #24*, 2013; available from http://collaborations.fz-juelich.de/ikp/anke/internal_notes/TechNote24.pdf
- [4] G.G. Ohlsen and Jr.P.W. Keaton, *Nuclear Instruments and Methods* 109(8):41-59, 1973
- [5] E. Weise, *EDDA internal report #00=01*, 2000
- [6] M. Altmeier, *Phys. Rev. Lett.* 85: 1819-1822, 2000

^a IKP FZJ, Jülich, Germany

^b HEPI TSU, Tbilisi, Georgia

^c PNPI, Gatchina, Russia

^d LNP JINR, Dubna, Russia

^e University College London, U.K.

* supported by Shota Rustaveli National Science Foundation of the Republic of Georgia

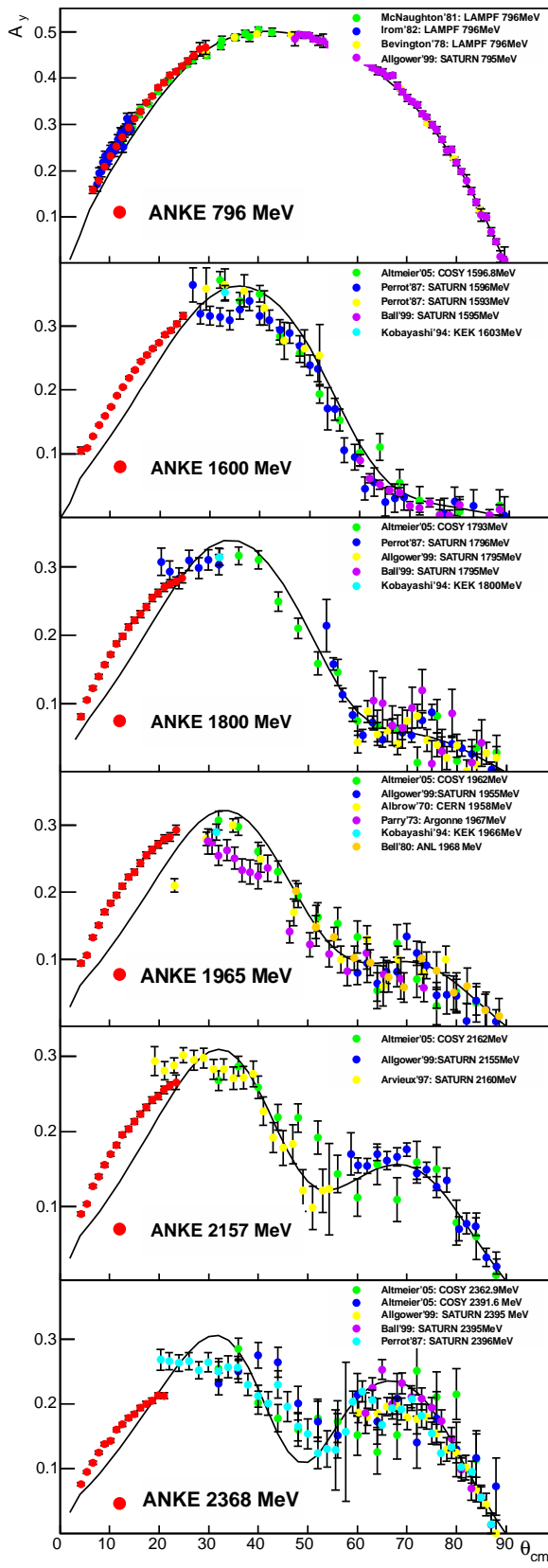


Fig. 1: The preliminary values of the analysing powers for elastic pp scattering measured with the ANKE STT at several energies (red circles) are compared to published data. Also shown are curves corresponding to the SAID 2007 partial wave solution.

S. Barsov¹, Z. Bagdasarian^{2,3}, D. Chiladze^{2,3}, S. Dymov^{2,4}, A. Kacharava², G. Macharashvili^{3,4}, S. Merzlyakov^{2,4}, S. Mikirtychyants^{1,2}, R. Schleichert², S. Trusov² for the ANKE collaboration

As discussed in [1], the nucleon-nucleon interaction amplitudes extracted by the phase-shift analysis are of general importance for study of any hadronic process at intermediate energies. Since the reliability of phase-shift analysis strongly depends on the set of available data, it must be a priority at any facility to fill in any gaps in the data base. The significant contribution to a small angle domain of the np elastic scattering has been done at ANKE during last years by measuring the interaction of deuteron beam with the hydrogen target [2]. However, in this case the beam energy is limited by 1.15 GeV/nucleon. To approach the higher energy domain, where data are very scarce, measurements were performed at ANKE using the polarized proton beam and unpolarized deuterium cluster target. Here we report the current status of analysis of data obtained in the April 2013 beamtime.

Measurements were done at 6 proton beam energies of 0.8, 1.6, 1.8, 2.0, 2.2 and 2.4 GeV. The orientation of beam polarization along Y-axis was changing every 3 minutes. The value of polarization was measured by the EDDA polarimeter. Two Silicon Tracking Telescopes were installed at 3cm distance to the left (STT1) and the right (STT2) from the deuterium target to detect low energetic particles in coincidence with fast particles going into the ANKE Forward detector (Fd). It must be noted that other data on the pd [3] and quasi-free NN elastic scattering [4], which can be used for comparison with our results, exist at $T_p = 0.8$ GeV only.

Having a proton identified in one of STT, the missing mass distribution of $pd \rightarrow ppX$ reaction was obtained (Fig. 1). Peaks corresponding to the quasi-free NN elastic scattering are well positioned at the neutron mass.

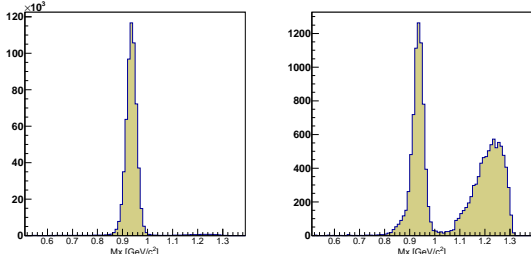


Fig. 1: Missing mass of two protons at $T_p = 0.8$ GeV. One proton is detected in the Fd and other one either in the STT1(left panel) or in the STT2(right panel).

The simulation results of $pd \rightarrow ppn_{sp}$ and $pd \rightarrow pnp_{sp}$ reactions are presented in Fig. 2. It was performed using the GEANT program package. The Fermi motion of nucleons inside deuteron and the differential cross section given by the SAID were included. In framework of the “spectator” model supposed, the quasi-free pp elastic scattering turns to be kinematically suppressed in the STT2 due to the asymmetric Fd acceptance.

Under the given experimental conditions, one has to derive polarization observable from the simple asymmetry of counts corresponding to different orientations of the beam polarization. It is well known that such asymmetry is very sensitive to the relative normalization of counts measured, in fact, at different luminosity and different beam polarization values. Moreover, in this particular experiment the cluster target den-

sity was changing in time which makes the normalization of data rather complicated.

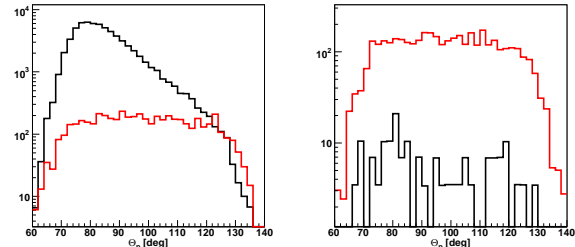


Fig. 2: The acceptance for $pd \rightarrow ppn_{sp}$ (black lines) and $pd \rightarrow pnp_{sp}$ (red lines) reactions simulated in the framework of “spectator” model at $T_p = 0.8$ GeV. One proton is detected in the Fd and other one either in the STT1 (left panel) or in the STT2 (right panel).

To verify the normalization procedure, the $\vec{p}d$ elastic scattering was selected by the detection of deuteron in the STT1 in coincidence with the scattered proton detected in the Fd. The angular dependence of asymmetry was obtained to be in a good agreement with the angular dependence of the analyzing power $A_y(\Theta_{cm})$ measured in [3]. (Fig. 3) Furthermore, the average beam polarization value determined from the asymmetry is found to be of **0.513+-0.001(stat)** while the same value measured by the EDDA polarimeter is equal to **0.4890+-0.0003(stat)+/-0.015(sys)**.

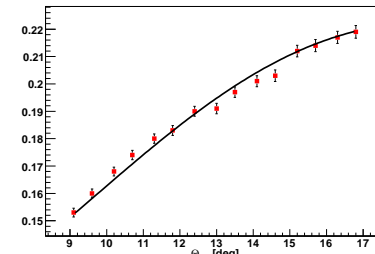


Fig. 3: The $\vec{p}d$ elastic scattering asymmetry (points) versus Θ_{cm} angle is shown together with the $A_y(\Theta_{cm})$ from [3] (line) scaled with the only parameter equal to the average beam polarization at $T_p = 0.8$ GeV.

Despite the consistent result achieved for $\vec{p}d$ elastic scattering, the analyzing power for the quasi-free $\vec{p}n$ elastic scattering derived in the same way from the same set of data was found to be about 30% smaller than the $A_y(\Theta_{cm})$ obtained in [4]. The further data analysis is in progress to find out the origin of this discrepancy.

References:

- [1] Proposal COSY-212 (2012)
- [2] D.Mchedishvili, PhD thesis (2013)
- [3] F.Irom et al., Phys.Rev. C 28, 2380 (1983)
- [4] M.L.Barlett et al., Phys.Rev. C 27, 682 (1983)

1 PNPI, 188350 Gatchina, Russia

2 IKP, FZ Jülich, 52425 Jülich, Germany

3 HEPI TSU, 0186 Tbilisi, Georgia

4 JINR, 141980 Dubna, Russia

* supported by the COSY-FFE programme

The cross section angular dependences of the $pp \rightarrow \{pp\}_s \pi^0$ reaction at several energies in the $\Delta(1232)$ excitation range*

D. Tsirkov¹, S. Dymov^{1,2}, V. Komarov¹ for the ANKE collaboration

The study of the reaction $pp \rightarrow \{pp\}_s \pi^0$ at intermediate energies at ANKE [1, 2] revealed that the forward cross section energy dependence exhibits a clear peak associated with the $\Delta(1232)$ resonance excitation. The angular slope of the cross section for the data collected at the beam energies of 500, 550 and 700 MeV [2] turned out to be very sensitive to small uncertainties in ANKE positioning, in contrast to the cross section at $\theta_{pp}^{\text{cm}} = 0$, that is relatively stable. Thus to obtain the cross section angular dependence a procedure of tuning the known setup geometry was developed. That stabilised the slope, and the resulting cross section angular dependences are provided in fig. 1.

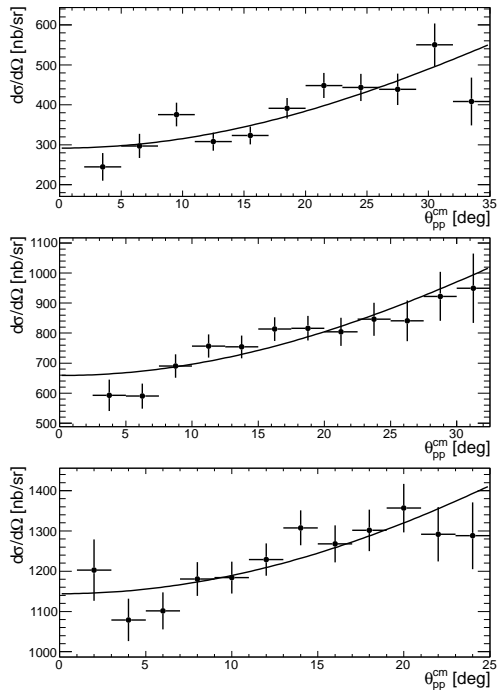


Fig. 1: The cross section angular dependences for the 500, 550 and 700 MeV beam energies, the lines represent fits linear over $\sin^2 \theta_{pp}^{\text{cm}}$.

The vector analysing power for the energies in question has been measured as well [3], allowing a simple partial wave analysis to be done, similar to that made earlier for 353 MeV [4], with the following differences. Firstly, phases were not fixed using the Watson theorem. Secondly, it was assumed that the two transitions M_s^P and M_d^P dominate, and others were neglected, by analogy with the SAID partial wave analysis of the similar $pp \rightarrow d\pi^+$ reaction[5]. With these assumptions, the equations (8) and (9) from [4] give:

$$\begin{aligned} \frac{d\sigma}{d\Omega} \cdot \frac{4p}{k} &= \left(s^2 + \frac{4}{3}sd \cos \phi + \frac{4}{9}d^2 \right) + \\ &\quad + \left(-2sd \cos \phi - \frac{1}{3}d^2 \right) \sin^2 \theta, \\ A_y \frac{d\sigma}{d\Omega} \cdot \frac{4p}{k} &= (sd \sin \phi) \sin 2\theta, \end{aligned}$$

where $s = |M_s^P|$, $d = |M_d^P|$, and ϕ is the difference of their phases. For each energy the combined fit of the cross section and analysing power angular dependences with these equations provides interchangeable two sets of values for the amplitudes and phase difference (fig. 2), each resulting in exactly the same shape of fitting functions. Additional considerations are needed to select one of them.

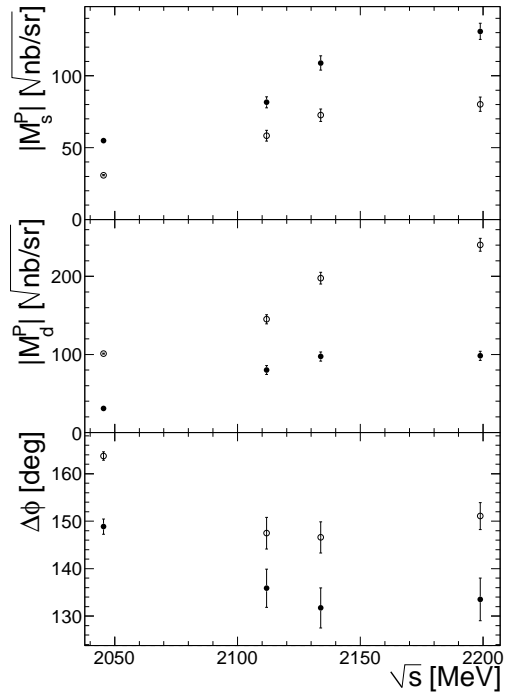


Fig. 2: The amplitudes and phase difference for the M_s^P and M_d^P transitions. The c.m. energies correspond to the beam energies of 353, 500, 550 and 700 MeV. Two solutions for each energy are represented with either filled or blank circles.

Besides the ANKE forward detector, employed in obtaining the presented results, the positive side detector collected some data as well. Due to the problems with the trigger system, these data were not used in the analysis. There are some hints that this trigger inefficiency could be quantitatively estimated. In this case the available acceptance could be extended to cover the polar angles up to 90°, providing the full cross section angular dependence.

References:

- [1] V. Kurbatov *et al.*, Phys. Lett. B **661** (2008) 22
- [2] D. Tsirkov *et al.*, ANKE annual reports 2011
- [3] D. Tsirkov *et al.*, ANKE annual reports 2010
- [4] D. Tsirkov *et al.*, Phys. Lett. B **712** (2012) 370
- [5] R. A. Arndt *et al.*, Phys. Rev. C **56** (1997) 635
<http://gwdac.phys.gwu.edu>

¹ LNP JINR, RU-141980 Dubna, Russia

² Phys. Inst. II, UEN, D-91058 Erlangen, Germany

* supported by COSY-FFE

The quasi-free reaction $p + d \rightarrow d + \eta + p_{\text{sp}}$ close to threshold at ANKE*

D. Schröer[†], C. Fritzsch, A. Khoukaz, M. Mielke, M. Papenbrock, M. Rump, A. Täschner for the ANKE-Collaboration

Recently the reaction $p + d \rightarrow d + \eta + p_{\text{sp}}$ was measured near the production threshold at ANKE in order to extract total and differential cross sections [1]. Based on these information the $d\eta$ scattering length $a_{d\eta}$ will be measured which will shed new light on the examination of mesic nuclei. For this purpose two beam momenta ($p_{\text{beam}} = 2.09 \text{ GeV}/c$ and $p_{\text{beam}} = 2.25 \text{ GeV}/c$) have been used. The deuteron target is used as an effective neutron target with a spectator proton. Because of the Fermi-motion of the nucleons inside the target-deuteron these data allow to investigate the cross section in an excess energy range from 0 MeV up to 100 MeV. As the reconstruction of the η meson in this reaction will be achieved via the missing mass method, it is important to clearly identify the spectator proton in the Silicon Tracking Telescopes (STT) and the deuteron in the ANKE Forward system (Fd).

A particle hit in the Fd detector is selected using energy loss (ΔE) versus momentum (p) plots. In the case of the deuteron this task is very challenging because the proton and deuteron bands are located very close together (Fig. 1 (left)). This can also be seen in the projection of $\Delta E \cdot \beta^2$ (Fig. 1 (right)) with the relativistic velocity β . In this case there is a huge proton peak with a small deuteron shoulder at the right tail so that a clean deuteron identification is difficult. To improve the situation two complementary methods are applied.

If one investigates the energy loss in a Fd counter as a function of the y-momentum of the detected particle it is obvious that the energy loss is not constant (Fig. 2). This is caused by two effects. First, the particle has to pass a larger distance in the hodoscope if the y-momentum is higher. Secondly, there are two energy loss measurements for each counter of the Fd system, one at the top and one at the bottom and they have to be calibrated accordingly. The energy loss in each counter can be described by a second order polynomial. After the correction with this function the energy loss is independent of the y-momentum and the proton and the deuteron bands are significantly narrower.

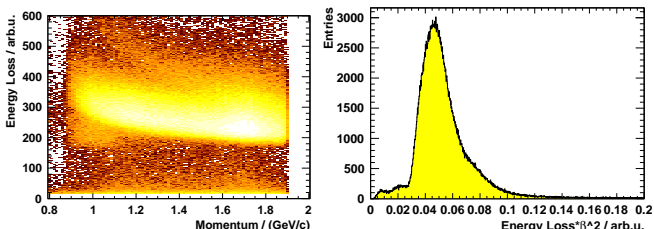


Fig. 1: Energy loss versus momentum (left) in the Fd system before applying cuts on the time-of-flight and before correcting for the y-momentum. A broad proton band and a deuteron band on top of it is visible. Associated $\Delta E \cdot \beta^2$ -spectrum (right) with a dominating proton peak and a small deuteron shoulder on the right hand tail.

Additionally, a special trigger, combining the Positive (Pd) and the Fd system, was used during the beam time. By de-

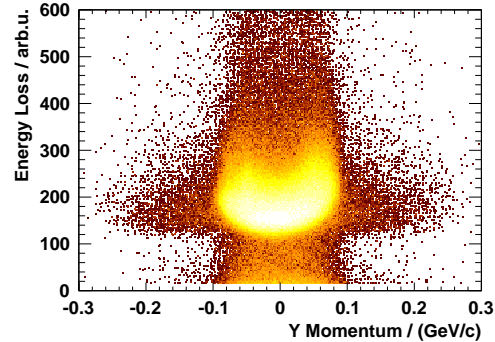


Fig. 2: Energy loss versus the y-momentum of the measured particles in one counter of the Forward system.

tecting a π^+ in the Pd detector, which can be identified easily via the low energy loss compared to protons, and another particle in the Fd system, one can compute the Time-of-Flight (ToF) difference of these two particles and distinguish between protons and deuterons in the Fd detector. The results of this method are shown in Fig. 3. A deuteron band in the ΔE -vs- p -spectrum is clearly visible (left) and enables a separation in the $\Delta E \cdot \beta^2$ -spectrum (right), where a deuteron peak can be identified so that deuterons can be selected by cutting on this peak [2].

The cut parameters, obtained in this way, can be used for the following analysis and will allow to reduce the proton background in the reaction $p + d \rightarrow d + \eta + p_{\text{sp}}$ drastically. The further analysis of the data is in progress with the next step being the identification and reconstruction of the spectator protons in the Silicon Tracking Telescopes.

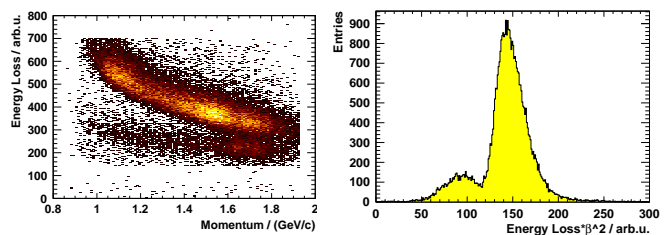


Fig. 3: Energy loss versus momentum (left) in the Fd system after applying ToF-cuts. The deuterons (upper band) are clearly visible while the protons are suppressed. $\Delta E \cdot \beta^2$ -spectrum (right) in the Fd system with ToF-cuts resulting in a clean deuteron peak with a few remaining protons at the left hand tail.

References:

- [1] A. Khoukaz et al, Measurement of the quasi-free $pn \rightarrow d\eta$ cross section at ANKE, 2012 , <http://www2.fz-juelich.de/ikp/anke/en/proposals.shtml>
- [2] M. Rump, bachelor thesis, 2013, Westfälische Wilhelms-Universität Münster

*Supported by COSY-FFE

[†]Institut für Kernphysik, Westfälische Wilhelms-Universität, 48149 Münster, Germany

Double differential cross sections for $d + p \rightarrow {}^3\text{He} + \pi^+ + \pi^-$ *

M. Mielke[†], C. Fritzsch[†], A. Khoukaz[†], M. Papenbrock[†], D. Schröer[†], A. Täschner[†], and C. Wilkin,[‡]
for the ANKE collaboration

Two pion production in nuclear scattering processes has been the subject of intensive research for many years, in particular due to the appearance of the so-called ABC effect [1]. Though distinct progress in its understanding has been made, there are still important questions to be solved. Especially the role of the Roper resonance in double pionic fusion is so far only poorly examined. In the $dp \rightarrow {}^3\text{He} \pi^+ \pi^-$ reaction its influence manifests itself through a difference between the $M_{^3\text{He}\pi^+}$ and $M_{^3\text{He}\pi^-}$ distributions, as already seen in [2]. The reason for this can be found in the difference between the Clebsch-Gordan coefficients for the decay channels $N^* \rightarrow \Delta\pi^- \rightarrow N\pi^+\pi^-$ and $N^* \rightarrow \Delta\pi^+ \rightarrow N\pi^-\pi^+$. With the benefit of the good momentum resolution of the ANKE detector, the resulting differences in the $M_{^3\text{He}\pi}$ invariant mass spectra could be quantified. The experiment was carried out at an excess energy of 265 MeV with respect to the reaction threshold. Events with coincident hits of ${}^3\text{He}$ nuclei in the forward detection system and at least one of the pions in the negative or positive detection system were used for the analysis. After the identification of the reaction with $\Delta E/p$, time-of-flight, and missing-mass selections, the residual background does not exceed 0.5%. For the resulting clean data sample the undetected pions were reconstructed through the missing momentum. A restriction to ${}^3\text{He}$ angles in centre-of-mass system (CMS) from 143° to 173° was imposed, because in this kinematical region there is practically a full coverage of the $dp \rightarrow {}^3\text{He} \pi^+ \pi^-$ Dalitz plot.

The limited ANKE acceptance at high excess energies, and the fact that the ABC effect causes a strong deviation from a phase-space behaviour, made it necessary to perform an accurate acceptance correction. This could be achieved by using Monte Carlo simulations with the following ansatz:

$$\sigma \propto \left| [(m_\pi)^2 + \alpha \vec{k}_1 \cdot \vec{k}_2] (3\Delta^{++} + \Delta^0) \right|^2, \quad (1)$$

where $\alpha = 0.2 + i0.3$ is a fitted value, \vec{k}_i are the pion momenta in CMS, and Δ^{++} and Δ^0 are Breit Wigner functions of the respective nucleon excitation. The factors 3 and 1 reflect different isospin couplings coming from the Roper decay. The systematic uncertainties of this method were estimated through comparison to correction factors obtained with variants of Eq. (1). The model-dependence of the acceptance correction was also studied by using a multidimensional matrix method.

Figure 1 shows the measured double-differential cross sections for the three possible two-particle invariant mass combinations, compared with phase space distributions and Monte Carlo simulations according to Eq. (1). All the uncertainties shown are of a purely statistical

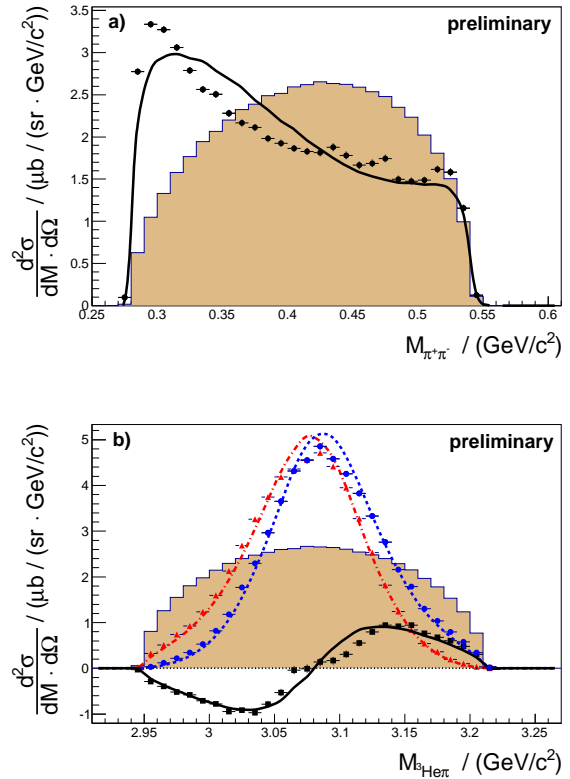


Figure 1: Centre-of-mass double-differential cross sections for the $dp \rightarrow {}^3\text{He} \pi^+ \pi^-$ reaction averaged over $143^\circ < \vartheta_{^3\text{He}}^{CMS} < 173^\circ$ in terms of (a) $M_{\pi^+ \pi^-}$ and (b) $M_{^3\text{He} \pi^+}$ (blue circles) and $M_{^3\text{He} \pi^-}$ (red triangles). The differences between the two $M_{^3\text{He} \pi}$ distributions are plotted as black squares. The lines represent Monte Carlo simulations corresponding to Eq. (1). For comparison, the shaded areas show the phase space distributions.

nature. An evaluation of the systematics is currently in progress.

The $M_{\pi^+ \pi^-}$ spectrum shows a strong enhancement at low masses, which is characteristic for the ABC effect. Clear signs of Δ excitation are visible in the $M_{^3\text{He}\pi^+}$ and $M_{^3\text{He}\pi^-}$ distributions. Also shown is the difference between the $M_{^3\text{He}\pi}$ combinations. This feature, and the gross structure of the $M_{\pi^+ \pi^-}$ distribution, can be described with the presented ansatz that includes the assumed imbalance of Δ^{++} and Δ^0 resonances. Based on this the $\pi\pi$ isospin-one contribution to the $dp \rightarrow {}^3\text{He} \pi^+ \pi^-$ reaction associated with the Roper excitation is currently studied in more detail.

References

- [1] A. Abashian et al., Phys. Rev. **132**, 2296 (1963).
- [2] M. Bashkanov et al., Phys. Lett. B **637**, 223 (2006).

*supported by the COSY FFE programme

[†]Institut für Kernphysik Westfälische Wilhelms-Universität, 48149 Münster, Germany

[‡]University College London, U.K.

Commissioning of the polarized deuterium gas target at ANKE*

Boxing Gou^{1,2} for the ANKE collaboration

In order to extend the spin programme [1] up to the highest energy at COSY, a polarized deuterium gas target has been commissioned at the ANKE spectrometer using an unpolarized proton beam of 600 MeV provided by the COoler SYnchrotron (COSY). Four polarization states (Table 1) and an unpolarized target were used in this experiment.

The reaction $p\vec{d} \rightarrow p\vec{d}$ is used as a polarimetry due to its high cross section and well measured analyzing powers within the ANKE acceptance at this energy ($T_p = 600$ MeV) [2-4]. Most of the deuterons from this reaction were detected by two STTs placed along the left and right sides of the target cell, which is confirmed by the missing mass spectrum of $p\vec{d} \rightarrow dX$ showing a peak at the proton mass. The particles are identified using the information about energy deposit in different layers of STT. With the target polarization axis pointing perpendicular to the accelerator plane, the polarized differential cross section of $p\vec{d} \rightarrow p\vec{d}$ is given by [5]

$$\frac{d\sigma}{d\Omega}^P(\theta, \phi) = \frac{d\sigma}{d\Omega}^0(\theta) \{1 + \frac{3}{2}Q_y A_y(\theta) \cos \phi + \frac{1}{4}Q_{yy} [A_{yy}(\theta)(1 + \cos 2\phi) + A_{xx}(\theta)(1 - \cos 2\phi)]\} \quad (1)$$

where $\frac{d\sigma}{d\Omega}^0(\theta)$ is the unpolarized differential cross section, $A_y(\theta)$ and $A_{yy}(\theta)$ are the vector and tensor analyzing powers respectively. To extract the polarizations, following cross ratio is defined:

$$CR = \frac{N_L^P N_R^0 - N_R^P N_L^0}{N_L^P N_R^0 + N_R^P N_L^0} \quad (2)$$

where $N_{L/R}^{P/0}$ denotes the number of events with polarized/unpolarized target and with deuterons detected in the left/right STT. Restricting ϕ close to 0 and π , taking into account that the ratio of the left and right STT efficiency $\frac{\varepsilon_L}{\varepsilon_R}$ does not change over the time, this cross ratio can be simplified as:

$$CR(\theta) \approx \frac{-\frac{3}{2}Q_y A_y(\theta)}{1 + \frac{1}{2}Q_{yy} A_{yy}(\theta)} \quad (3)$$

It allows to extract both vector (Q_y) and tensor (Q_{yy}) polarizations in one step, unless the vector analyzing power is too small. Fig. 1 shows the results of the fits, and the polarization values are presented in Table 1. However for state 3 (0, -2) and state 4 (0, +1) the tensor polarization (Q_{yy}) can not be determined due to reduced signals caused by the small vector polarization (Q_y). On the other hand the smallness of the vector polarization allows to determine the tensor polarization (Q_{yy}) via a counting rate ratio between polarized and unpolarized states.

$$\frac{N^P(\theta, \phi)}{N^0(\theta)} \approx R_{Lum.} [1 + \frac{1}{4}Q_{yy} A_{yy}(\theta)(1 + \cos 2\phi)] \quad (4)$$

Here $R_{Lum.} = \frac{Lum.}{Lum.0}$ is luminosity ratio between polarized and unpolarized states. By fitting counting rate ratio with eq. (4), following results were

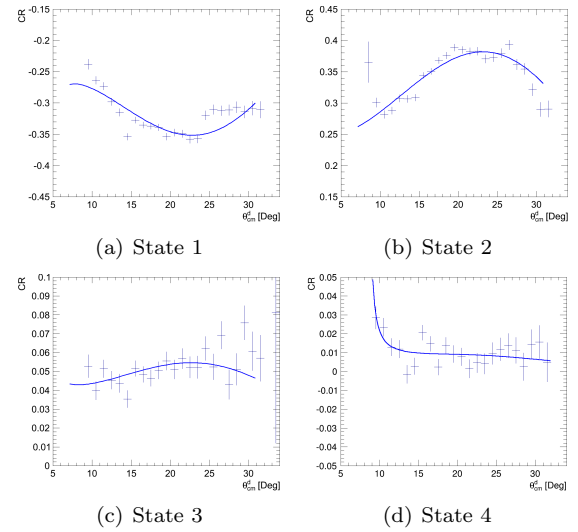


Fig. 1: Preliminary results of cross ratio (CR) as a function of deuteron scattering angle for all the four states, fitted by eq. (3).

obtained: $R_{Lum.}^3 = 0.697 \pm 0.003$, $Q_{yy}^3 = -1.24 \pm 0.023$ and $R_{Lum.}^4 = 0.702 \pm 0.004$, $Q_{yy}^4 = 0.3032 \pm 0.026$ (Fig. 2).

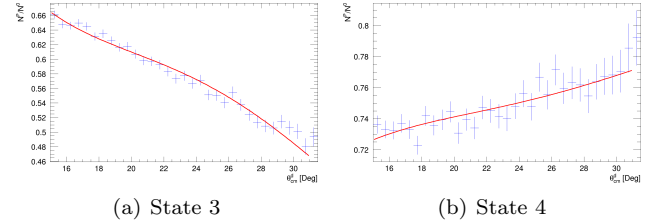


Fig. 2: Preliminary results of counting rate ratio (N^P/N^0) as a function of deuteron scattering angle for state 3 and 4, fitted by eq. (4).

Both ideal and measured polarizations of the four polarized states are summarized in Table 1.

Table 1: Polarized target states.

States	Ideal polarizations		Measured polarizations	
	Q_y	Q_{yy}	Q_y	Q_{yy}
State 1	+1	+1	0.719 ± 0.005	0.951 ± 0.054
State 2	-1	+1	-0.716 ± 0.007	0.738 ± 0.068
State 3	0	-2	-0.101 ± 0.003	-1.24 ± 0.023
State 4	0	+1	-0.014 ± 0.003	0.3032 ± 0.026

References:

- [1] A. Kacharava et al., *COSY proposal 152*.
- [2] J. Arvieux et al., *Nucl. Instr. Meth. A* **273** 48.
- [3] M. Haji-Saied et al., *Phys. Rev. C* **36** 2010.
- [4] D. Chiladze et al., *Phys. Rev. ST-AB*, **9** 050101.
- [5] G.G. Ohlsen, *Rep. Prog. Phys.* **35** 717.

¹ IKP, Forschungszentrum Jülich, 52425 Jülich, Germany

² IMP, CAS, Lanzhou 730000, China

* Supported by the CSC programme

Data analysis of the Silicon Tracking Telescope for the $pn \rightarrow nK^+\Lambda$ reaction

N. Savderova^{1,2}, S. Barsov^{1,2}, S. Trusov² and Yu. Valdau^{1,2,3} for the ANKE collaboration

The energy dependence of the total cross section for the Λ , Σ^0 and Σ^+ production in proton-proton collisions has been studied using various installations at COSY [1, 2, 3]. In contrast to that, there is almost no data on K^+ production in proton-neutron collisions available in literature. There were several attempts to explore difference between K^+ production on the proton and neutron using different nuclear targets and beams [4], but direct information can be obtained from the analysis of the experimental data collected using ANKE magnetic spectrometer in March 2011 [5].

In this experiment the $pd \rightarrow nK^+\Lambda p_{sp}$ reaction has been investigated using proton beam and deuteron as an effective neutron target. Two particles in the final state has been identified in the ANKE detector systems, the K^+ in the range telescopes and spectator proton p_{sp} in Silicon Tracking Telescope (STT). The energy of the proton beam is chosen such that kaons and protons, associated only with Λ production, can be detected in ANKE. Hence, detailed analysis of the ANKE STT is crucial for determination of the energy dependence of the total cross section for the $pn \rightarrow nK^+\Lambda$ reaction. For the spectator protons detection two (left and right) STT's have been used [6]. Two types of data, with and without zero suppression, has been collected from the STT during this experiment. To reduce amount of data written from the STT a special mode (zero suppression mode) of readout electronics has been used. In this mode, position of zero of the scale for each individual channel of the QDC has been determined during experiment and, together with threshold, has been loaded in to the readout electronics. In the data stream only data from channels with amplitude, which is higher then the sum of pedestal and threshold values, has been accumulated. For calibration purposes, in a zero suppression mode, one event out of thousand is written in to the data stream without pedestal suppression.

The STT data analysis includes [6]: definition of pedestal position and its correction, selection of nonstable segments, control of the energy calibration, reduction of the coincidence background. At the first stage of the STT data analysis, definition of pedestal positions and its correction has been performed for the data with and without zero suppression separately.

In addition to the traditional methods of pedestal position determination, a new technique for the identification and selection of the nonstable segments was used in the analysis. Using a dedicated software, all the runs were analyzed and information about pedestal position and its width (RMS) has been stored in the text files. This information has been studied as a function of time, taking one run as a time interval, and conclusion about instability of individual channels of the detector has been made run by run. List of nonstable segments, obtained within this analysis, is in agreement with the results of traditional analysis. This method can be used in future for the identification of nonstable channels using a simple, based on a formal criteria, method.

Besides pedestal position analysis, all the steps of the analysis necessary for the spectator proton identification has been done. Due to the possible instabilities in gain for individual detector sides charge accumulated on positive and negative side of individual detector can be different. Special correc-

tion procedure has been used to correct for this effect and reconstruct the energy losses.

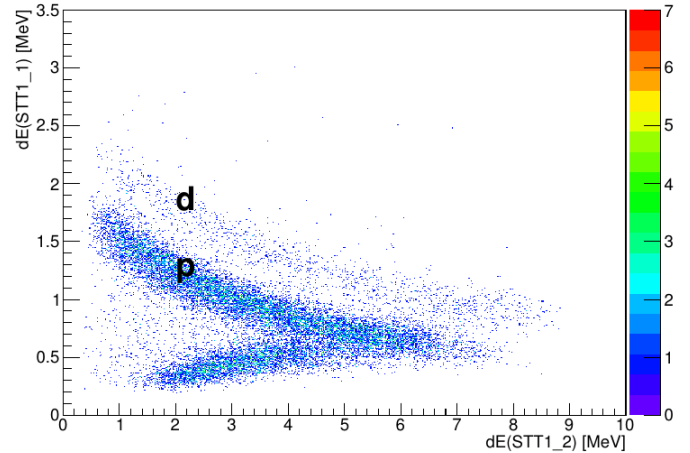


Fig. 1: Energy loss spectra in a first layer as a function of energy loss in a second layer in STT1 reconstructed for one run. Protons and deuteron's are well separated.

Because of the relatively high luminosity during beam time, it is necessary to use time information from the individual detector sides to reduce the coincidence background. Time calibration curve, obtained from the experimental data, has been used to select a genuine tracks in STTs. As a result, a clean identification of the protons and deuteron in the telescopes has been obtained (see Fig. 1).

On a last stage, using preselected K^+ data and reconstructed spectator proton four-momentum, the number of counts as a function of excess energy in $pn \rightarrow nK^+\Lambda$ reaction has been reconstructed. Obtained statistic is sufficient for the determination of the total cross section for the $pn \rightarrow nK^+\Lambda$ reaction with planned accuracy.

References:

- [1] J. Balewski *et al.*, Phys. Lett. B **388** (1996) 859.
- [2] S. Abd El-Samad *et al.*, Phys. Lett. B **632** (2006) 27; W. Eyrich, Prog. Part. Nucl. Phys. **50** (2003) 547.
- [3] Yu. Valdau *et al.*, Phys. Lett. B **652** (2007) 245.
- [4] Yu. Valdau *et al.*, Phys. Rev. C **84** (2011) 0055207.
- [5] A. Dzyuba, V. Koptev, Yu. Valdau, COSY Prosopal #203 (2010).
- [6] A. Mussgiller, "Identification and tracking of low energy spectator protons", PhD thesis, Universität zu Köln, 2005.

¹ High Energy Physics Department, Petersburg Nuclear Physics Institute, 188350 Gatchina, Russia

² Institut für Kernphysik, Forschungszentrum Jülich, 52425 Jülich, Germany

³ Helmholtz-Institut für Strahlen- und Kernphysik, Nussallee 14-16, D-53115 Bonn, Germany

Improvement in position and spatial resolution determination of the COSY-TOF Straw-Tube-Tracker

Sedigheh Jowzaee^a for the COSY-TOF collaboration

The Straw-Tube-Tracker (STT) is a main tracking detector in the COSY-TOF spectrometer, which is used to provide precise position information of charged particle tracks because of its higher resolution compared to other detectors in the COSY-TOF spectrometer. Precise determination of the track parameters depends on the accuracy in positioning and spatial resolution of the straw double layers and calibration in the COSY-TOF detector. The geometrical location of the straws in each double layer is known very well due to its structure in which 208 straw tubes are glued to each other in the form of a double layer. Therefore, the main uncertainty is the positioning error of a double layer. The geometrical location of double layers was studied and the improvement in the spatial resolution with the new calibration was checked. To obtain a precise calibration, some corrections including selection of first hit, signal width cut and electronics offset correction were done on the single straw raw TDC spectrum, and the $r(t)$ curve which is the correlation between the drift time and the isochrone radius was determined with the so-called “self-calibrating” method. For details see [1, 2]. The $r(t)$ curve was used in the next step of calibration to find the most probable correlation between drift times and track to wire distance with an iterative procedure which is called “autocalibration” using the reconstructed track parameters [1, 3].

To find the exact position of each double layer, the track reconstruction was done with a method called “unbiased”. In this method, the double layer which is studied will not be taken into account for track reconstruction, and the track refits are based on the information from other double layers. The distance of track to wire information for the ignored

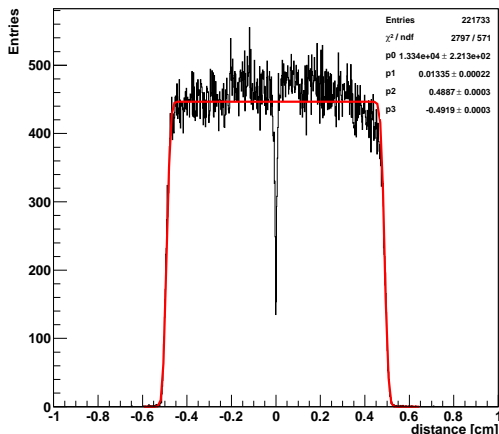


Fig. 1: The closest distance of track to wire distribution fitted with a convolution of a box and gaussian function (red line).

double layer is calculated with this refitted track, and this process is repeated for all double layers. This distance information is the most appropriate track parameter to study the shifts in the position of the double layer perpendicular to the wire direction. Any shift in the double layers position can be seen in the track to wire distance of right and left side of the straw wire. Hence, the closest distance of tracks to wire for each double layer was plotted and a box function convoluted with a gaussian function was fitted on the distribution as

shown in Figure 1. The reduction in number of entries at 0 cm is due to the minimum isochrone radius around the wire that tracks can not be recorded less than it. Because when the tracks pass so close to the wire in the avalanche area, the ionized electrons do not have sufficient path length to produce secondary ionized pairs and there is a systematic shift in TDC spectrum for these tracks. This minimum is usually in the range of 10-20 μm . The difference in the fit parameters of left and right side of the distribution was used to calculate the shift of each straw double layer. This is an iterative process which takes the geometry information of the mechanical installation of STT in beginning and starts with correction of the double layer with higher shift and iterates up to setting the shift of all double layers less than 50 μm . The positioning of the STT was improved by 50 % compared to the former work [4].

After determination of the final value for the position correction of each double layer, the resolution of the straw double layers was studied. To find the resolution, the “residual”,

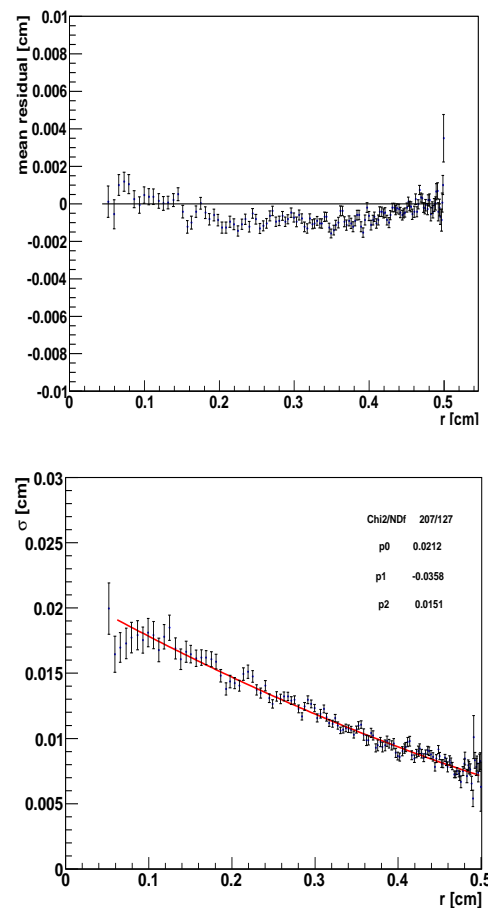


Fig. 2: (Top) The mean residual distribution versus isochrone radius after five iterations. (Bottom) Sigma of the residual distribution to isochrone radius which is fitted with a second order polynomial function (red line). The resolution is worse close to the wire because of the primary ionisation spacing and higher drift velocity. The resolution improves near the wall of the tubes and is limited to 70 μm by diffusion of the electrons.

which is the difference in the distance of the fitted track to

the wire and the isochrone radius, was calculated. With a precise calibration, the mean residual should be zero at all radii as shown in Figure 2 (top) for the new calibration. This residual distribution is significantly improved compared to earlier results [4]. The spatial resolution of STT is the width of the residual distribution of the reconstructed tracks. It is shown in Figure 2 (bottom) for the new calibration. The resolution at a radius of 0.25 cm averaged over all double layers obtained with the new calibration is $142 \pm 9\text{ }\mu\text{m}$. This is an improvement of about 20% compared to the former one. This calibration can improve the reconstruction efficiency and the identification of the delayed vertex at shorter distances from the primary vertex, which are under study to analyze of hyperon production with the COSY-TOF STT in the $pp \rightarrow pK^+\Lambda$ reaction.

We acknowledge support by the Foundation for Polish Science-MPD program, co-financed by the European Union within the European Regional Development Fund and by the FFE grants of the Research Center Jülich.

References:

- [1] PANDA collaboration, Technical Design Report for the PANDA (AntiProton Annihilations at Darmstadt) Straw Tube Tracker, Eur. Phys. J. A. 49: 25, arXiv:1205.5441v1, 2013.
- [2] S. Jowzaee for the COSY-TOF collaboration, IKP Research Center Juelich, Annual Report 2012.
- [3] S. Jowzaee for the COSY-TOF collaboration, Calibration of a Modular Straw-Tube-Tracker for the COSY-TOF Experiment, Acta Physica Polonia B Proceedings Supplement. 6, 1067-1072, 2013.
- [4] M. Röder, PhD Dissertation, University of Bochum, 2011.

^a Jagiellonian University, Krakow, Poland

Study of the beam polarization with COSY-TOF

Florian Hauenstein^a for the COSY-TOF collaboration

In the measurement of the $\vec{p}p \rightarrow pK^+\Lambda \rightarrow pK^+p\pi^-$ reaction with the COSY-TOF detector a polarized proton beam is used. This allows to study various polarization observables like analyzing powers or depolarization. The strength of the beam polarization was determined with elastic scattered events.

The extraction of elastic events is done with a cut on the coplanarity and missing energy distribution which is shown in Figure 1. To separate the elastic events in the peak from

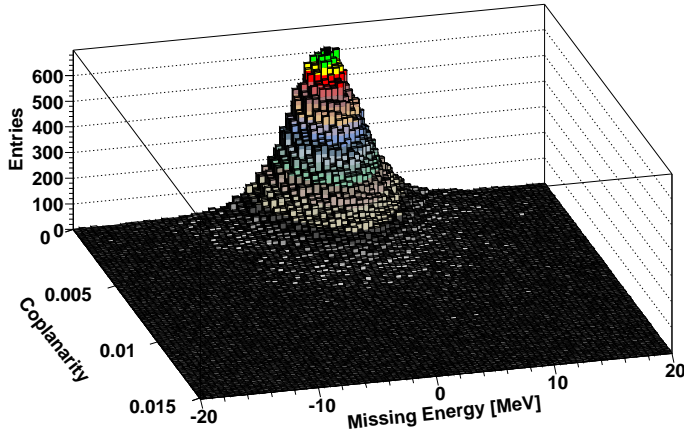


Fig. 1: Missing energy versus coplanarity for two track events. The peak corresponds to the elastic events.

the background a circular cut around the peak is used. This results in a clean data sample with a background contribution of less than 0.5 % (for further details see also [1]).

The averaged polarization for both spin directions is calculated with the method described in [1]:

$$P_B = \frac{\varepsilon_{LR}(\theta_p^{CMS}, \phi)}{\cos(\phi) \cdot A(\theta_p^{CMS})} = \frac{\bar{\varepsilon}(\theta_p^{CMS})}{A(\theta_p^{CMS})} \quad (1)$$

Here $A(\theta_p^{CMS})$ is the mean analyzing power in one bin of proton scattering angle in CMS system (θ_p^{CMS}) taken from the partial wave analysis SAID [2]. $\varepsilon_{LR}(\theta_p^{CMS}, \phi)$ is the measured left-right asymmetry caused by the polarization and analyzing power. $\bar{\varepsilon}(\theta_p^{CMS})$ is the averaged asymmetry in one scattering angle bin. The asymmetry can be determined from the count rates according to

$$\varepsilon_{LR}(\theta_p^{CMS}, \phi) = \frac{L(\theta_p^{CMS}, \phi) - R(\theta_p^{CMS}, \phi)}{L(\theta_p^{CMS}, \phi) + R(\theta_p^{CMS}, \phi)} \quad (2)$$

with

$$L(\theta_p^{CMS}, \phi) = \sqrt{N^+(\phi) \cdot N^-(\phi + \pi)} \quad (3)$$

$$\text{and } R(\theta_p^{CMS}, \phi) = \sqrt{N^+(\phi + \pi) \cdot N^-(\phi)} \quad (4)$$

$N^\pm(\phi)$ are the number of events for the azimuthal angle ϕ with a spin up (+) or spin down (-) polarized beam, respectively. Multiplying the events on one detector side with the number of events on the other side with opposite spin cancels

out systematic effects from an azimuthal asymmetric detector acceptance to first order.

The resulting asymmetry calculated with Equation 2 is fitted with $a * \cos(\phi)$. a corresponds to the averaged asymmetry $\bar{\varepsilon}(\theta_p^{CMS})$. The polarization is determined for each θ_p^{CMS} bin using the analyzing power from SAID [2]. The polarization as a function of scattering angle is plotted in Figure 2 (upper frame) for the data taken with 2.95 GeV/c beam momentum. The mean value is $(61.2 \pm 2.2)\%$.

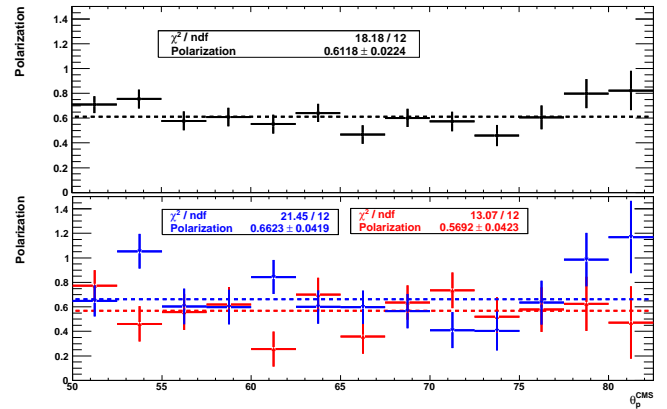


Fig. 2: Beam polarization as a function of proton scattering angle θ_p^{CMS} for data at 2.95 GeV/c. Upper frame: Average polarization from whole data. Lower frame: Up (red) and down (blue) polarization from corresponding data samples.

In addition to the determination of the averaged polarization it is also possible to get the degree of polarization separately for both spin directions. The data is separated into two samples according to each spin direction. This information is obtained from a tag of the polarized proton source. For both spin directions the asymmetry is calculated with

$$\varepsilon_{LR}^\pm(\theta_p^{CMS}, \phi) = \frac{N^\pm(\phi) - N^\pm(\phi + \pi)}{N^\pm(\phi) + N^\pm(\phi + \pi)} \quad (5)$$

Since any detector asymmetry in the azimuthal distributions results in a systematic error when determining $\varepsilon_{LR}^\pm(\theta_p^{CMS}, \phi)$ an acceptance correction is applied to the ϕ distributions. This correction is determined with an unpolarized measurement under the same conditions as the polarized measurement. Because the ϕ distribution must be constant without polarization any deviation is a result from detector asymmetries. Thus a correction for these asymmetries can be extracted. This is applied for each θ_p^{CMS} and ϕ bin. The $N^\pm(\phi)$ are the corrected number of events for the corresponding azimuthal angle ϕ .

The $\varepsilon_{LR}^\pm(\theta_p^{CMS}, \phi)$ distribution is fitted with $a * \cos(\phi)$. The magnitude of up and down polarization is obtained (red and blue crosses in Fig. 2 lower frame, respectively) using the mean analyzing power from SAID [2]. Since the analyzing power and the statistics are very low in the θ_p^{CMS} range from 82° to 90° and the acceptance of the COSY-TOF detector

drops above 60° lab angle (corresponding to angles smaller than 50° in CMS frame), only the range between 50° and 82° is fitted with a constant function. The result for the magnitude of the up polarization is $(57 \pm 4.2)\%$ and of the down polarization $(66 \pm 4.2)\%$. Both values are within their error bars compatible with the average polarization of $(61.2 \pm 2.2)\%$ calculated with Eq. 2.

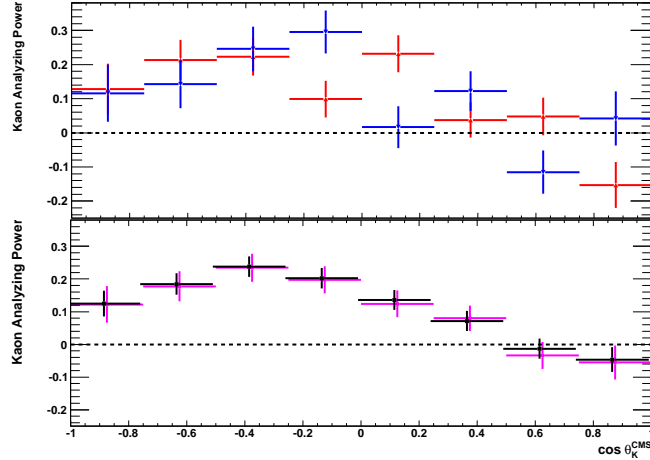


Fig. 3: Kaon analyzing power as a function of cosine of the Kaon scattering angle θ_K^{CMS} for data at 2.95 GeV/c. Upper frame: Kaon analyzing power from spin up sample (red) and spin down sample (blue) with additional acceptance correction from the unpolarized measurement. Lower frame: Average Kaon analyzing power from two methods: Mean value of spin up and down Kaon analyzing power calculated separately (violet) and from full data sample taking the average beam polarization (black). The black points are shifted horizontally for better visualisation

Further studies of the influence of the difference for up and down polarization are performed on the Kaon analyzing power. It is determined in an analogous way as for the beam polarization. To get the Kaon asymmetry, Equation 2 is used in the case of the whole data sample and Equation 5 for the up and down samples, respectively. The ϕ distributions of the Kaon are corrected with the results from the unpolarized measurement. The asymmetries are divided by the corresponding polarization i.e. the Kaon asymmetry from the spin up sample is divided with the up polarization of $(57 \pm 4.2)\%$. The results separated for up and down can be seen in Fig. 3 as the red and blue crosses in the upper part.

The mean value of the spin up and down analyzing power (Fig. 3 violet crosses in the lower part) is compared with the values determined by the full data sample taking the average beam polarization (result see Fig. 3 black points in lower part). The differences of the values are less than 30% of a standard deviation and so negligible to first order in further calculations.

With the methods described above the magnitude of the polarization can be determined separately for both spin directions. The results can be used to check for systematic errors in the determination of other polarization observables from the averaged polarization value. Therefore they will be applied to the analysis of further COSY-TOF data.

References:

- [1] M. Roeder, PhD Thesis, University Bochum, 2011
- [2] <http://gwdac.phys.gwu.edu>

^a Physikalisches Institut, Friedrich-Alexander-Universität Erlangen-Nürnberg, 91058 Erlangen, Germany

New Results of Studies on Piezoelectric Nozzle Units for Pellet Targets*

K. Demmich[†] F. Bergmann[†] P. Goslawski[†] P. Hüsemann[†] N. Hüskens[†] F. Schepers[†] A. Täschner[†] and A. Khoukaz[†]
for the WASA-at-COSY-Collaboration

The WASA pellet target is currently the only pellet target in operation at an accelerator experiment. It provides the high luminosities which are necessary for the investigations of rare meson decays, one focus of the WASA-at-COSY physics program. In order to improve the performance and reliability of the target operation several optimizations have been done since the target device was transferred from Uppsala to Jülich. One important aspect is the nozzle production process at the ZEA-1 of the FZ Jülich, where improved filter designs are used and several cleaning steps and quality checks are carried out to each nozzle to avoid a blocking during operation [1]. An additional nozzle test station has been developed in Münster to perform stress tests with gas throughput and oscillating piezo and, moreover, to examine the electrical and mechanical properties of the piezo nozzle system [2]. These measures improved the reliability of the target operation significantly. Thus, the test station is optimized to drive this progress forward.

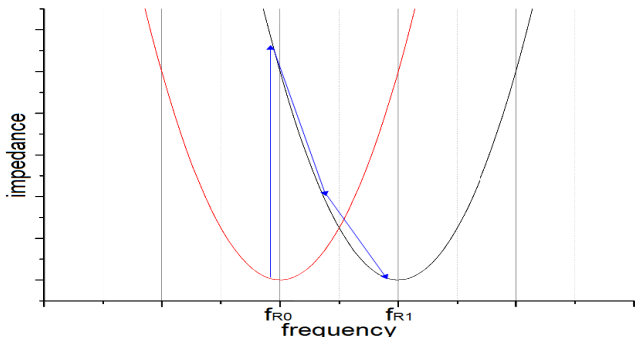


Figure 1: Schematic: Resonance curve (left) and resonance frequency f_{R0} at the beginning of a measurement and shifted curve after a few days (right). The software finds the minimum and sets the new driving frequency f_{R1} [4].

Measurements with the existing nozzle test station in Münster revealed a shift of the resonance frequency within a few days, which can be observed during target operation as well [3]. In order to further investigate this effect, a new software has been developed which allows for a periodical measurement of the piezo impedance spectrum close to the working point and adjusts – if necessary – the driving frequency according to the shifted resonance, identified by the minimum impedance (see figure 1 and 2). This advancement improves the nozzle test by stimulating the maximum stressing conditions as they are present during the target operations. Furthermore, this system might be implemented in the pellet target control to reduce the necessity of manual readjustments during the operation.

The droplet production process taking place at the pellet generator and especially the influence of parameters like the piezo voltage and frequency are not fully in-

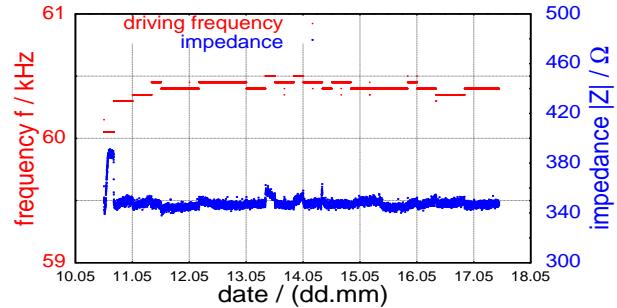


Figure 2: Impedance (blue) measured over one week and changes of the resonance frequency (red) [4].

vestigated yet. Beside the measurements of mechanical and electrical properties of the holder-nozzle system, a setup has been developed in Münster which gives the opportunity to study directly the droplet production. In order to generate droplets without any temperature or vacuum requirements, liquid n-pentane instead of hydrogen is pressed through a glass nozzle formerly used at the pellet target. Here, a stable stream of pentane droplet can be observed quite similar to the hydrogen droplet beam produced at the pellet target (figure 3). First studies reveal the same correlation between piezo resonances and droplet quality. Future measurements will head towards the widening of the convenient frequency bands with stable droplet productions by increasing the driving voltage and testing different nozzle and piezo designs.



Figure 3: The pentane beam right behind the nozzle breaking up into a regular flow of droplets, illuminated by stroboscopical light [4].

The presented optimizations during the nozzle production as well as the nozzle test station in Münster improved the reliability of the target operation significantly as blocking nozzles or damaged piezos can be rejected before installation. The studies on the pentane droplets promise a deep understanding of the production process which is not only important for WASA but, moreover, gives important inputs for future pellet targets like for PANDA at HESR/FAIR, Darmstadt.

References

- [1] A. Winnemöller et al., *The WASA-at-COSY pellet target*, Jülich (2007), annual report
- [2] F. Bergmann et al., *Studies on Piezoelectric Nozzle Units for Pellet Targets*, Jülich (2011), annual report
- [3] F. Schepers, *Untersuchungen zum Düsensystem des WASA-at-COSY Pellettargets*, Münster (2013), bachelor thesis
- [4] P. Hüsemann, *Betrieb und Erweiterung eines Düsenteststands sowie Untersuchung von Pentandandroplets*, Münster (2013), bachelor thesis

*Supported by COSY-FFE

[†]Institut für Kernphysik Westfälische Wilhelms-Universität, 48149 Münster, Germany

Implementation of pellet tracking in physics experiments - initial studies at WASA

A. Pyszniak^{a,b}, H. Calén^a, K. Fransson^a, V. Hejny^{c,d}, Z. Rudy^b, M. Wolke^a, P. Wüstner^{e,f}
for the pellet tracking group and for the WASA-at-COSY collaboration

Introduction

A pellet tracking (PTR) system for PANDA has been designed in Uppsala [1]. With such a system one can reconstruct the positions of the individual pellets at the time of a hadronic interaction in the offline event analysis. This gives information on the position of the primary interaction vertex with an accuracy of a few hundred microns, which is very useful e.g. for reconstruction of charged particle tracks and secondary vertices and for background suppression.

The PTR data will be collected by a standalone system that is synchronized with the main DAQ, since it takes about 100 ms to collect all measurement data relevant for reconstructing a pellet track and this time scale is very different from the time scale handled by a hadron physics experiment DAQ (parts of ns to a few μ s). To get experience of how to synchronize and use PTR information in data analysis, information from a long-range (LR) TDC, read out by a standalone system working in parallel to the WASA DAQ, was processed. This LR TDC system operates with a similar time scale as pellet tracking (between some μ s and several seconds). The synchronization was achieved by writing a common time stamp (and event number) to both DAQ systems.

This study gives a simple demonstration of one possibility with pellet tracking. Using information from pellet tracking, the number of pellets in the accelerator beam region at the time of an interaction can be reconstructed. This information alone allows suppression of effects due to events not originating from accelerator beam - pellet interactions. The suppression can be done in two ways:

Event-by-event: reject events occurring when no pellet was present.

In measurement distributions: use the no-pellet event sample (properly normalized) for background subtraction.

“Empty target” corrections are normally difficult to make in high luminosity internal target experiments. To just switch off the target doesn’t make sense since the presence of the target may influence both the accelerator beam and vacuum conditions significantly.

The LR TDC information

There are pellets in the beam only for some fraction of the time, while events due to rest-gas and beam halo happen all the time. When a pellet is in the beam, it is most probable that the event came from the pellet. The integrated rate of interactions is exploited, to know when there are pellets in the beam. When a pellet passes through the beam, there are more interactions. For this purpose one of the trigger signals for collecting elastic scattering events (originating from the nominal interaction point) was connected to the LR TDC and used to monitor accelerator beam - pellet interactions. A typical 5 ms time spectrum from the LR TDC is shown in Figure 1. It takes $\approx 70 \mu$ s for a pellet to cross the COSY

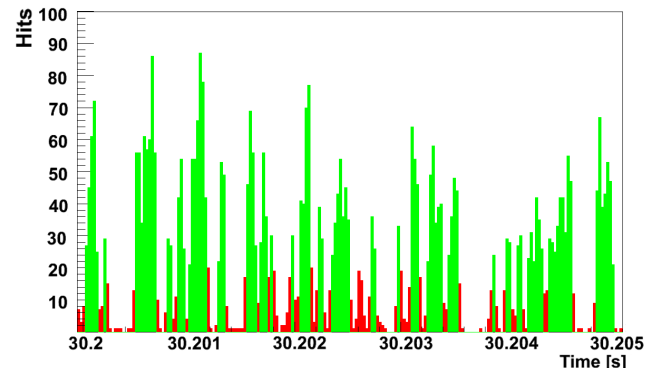


Figure 1. Example of the LR TDC spectrum (over 5 ms) with classification of pellet and non-pellet periods. “Pellet-class” (green) - pellets expected in the beam region, “Non-pellet-class” (red) - no pellet expected in the beam region. On the vertical axis is number of trigger signals per 25 μ s bin.

beam at its center. Structures of such duration are visible in the time spectrum. A simplified classification of time bins, each of length 25 μ s, was done (as indicated in Figure 1):

“Non-pellet-class” = low signal rate 0 - 20 / bin \leftrightarrow probably no pellet in the beam region.

“Pellet-class” = high signal rate > 20 / bin \leftrightarrow probably pellets in the beam region.

The signal rate ranges were adjusted to correct for accelerator beam decay ($\approx 50\%$) during the 50 s period in the accelerator cycle when the beam hit the pellet stream.

To check the feasibility of using a standalone (pellet tracking like) system together with a hadron experiment, a 16 min short test run at WASA was performed. Based on the collected data, the possibility to suppress background events by implementing the LR TDC information in the event analysis was studied. The pellet rate was about 8 k/s and in this case one expects that during 50 % of the time there are no pellets in the beam region.

Data analysis

As test reaction, $pp \rightarrow pp\pi^0 \rightarrow pp\gamma\gamma$ at a beam proton kinetic energy of 0.45 GeV was chosen. Events where both protons hit the forward detector and the two gammas hit the very forward part of the electromagnetic calorimeter (nominal scattering angles $\Theta = 20^\circ - 40^\circ$) were specially studied since it is fairly easy to see effects from rest-gas interactions in this kind of events. Figure 2 shows $\gamma\gamma$ invariant mass and p-p missing mass distributions for events collected during LR TDC “Non-pellet-class” time intervals and Figure 3 shows the same for events during LR TDC “Pellet-class” time intervals. Expectations from WASA Monte-Carlo (WMC) simulations, including rest-gas according to a realistic distribution, are also shown.

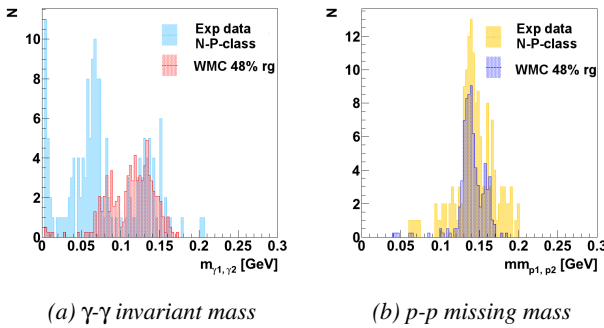


Figure 2. Distributions of events from the “Non-pellet-class” sample compared with WMC events from a sample with 48 % of the events originating from interactions in the rest-gas

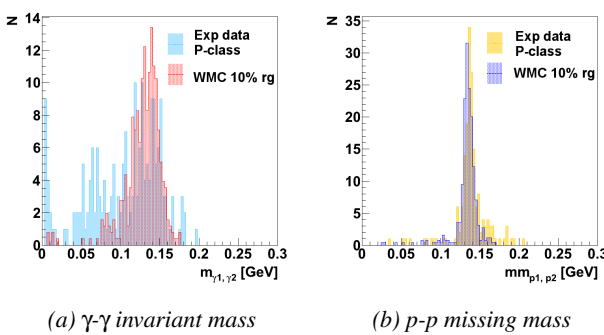


Figure 3. Distributions of events from the “Pellet-class” sample compared with WMC events from a sample with 10 % of the events originating from interactions in the rest-gas

As anticipated, the “Pellet-class” event sample (Figure 3) is in good agreement with WMC with a low rest-gas contribution, while the “Non-pellet-class” event sample (Figure 2) contains many more events originating in rest-gas, beam pipe walls and other background events not coming from the nominal interaction region. The structure in experimental data at low $\gamma\gamma$ invariant mass, most clearly seen in Figure 2a is probably due to beam-halo interactions in the beryllium

beam pipe walls, an effect that is not included in the WMC simulations. This structure is strongly suppressed in the “Pellet-class” event sample.

The method, using the integrated rate of interactions to know when there are pellets in the beam, could well be exploited in real experiments. Compared to pellet tracking it has some drawbacks, e.g. the monitoring signals and the reactions under main study, both contain contributions from background. Due to this and limited statistics it may be difficult to separate “Pellet” from “Non-pellet” time intervals.

Summary

Initial studies on how to synchronize and implement pellet tracking information in a hadron physics experiment has been done at WASA. A detailed comparison between π^0 event candidates from different time intervals confirms that this works according to expectations.

The project is supported by COSY-FFE, EC FP7, Swedish Research Council, Foundation for Polish Science (MPD program) and Polish National Science Center.

References

[1] A. Pyszniak, H. Calén, K. Fransson and Z. Rudy, *Design Simulations for Pellet Tracking Systems*, IKP Annual report, 2012.

^a Department of Physics and Astronomy,
Uppsala University, SE-75120, Uppsala, Sweden

^b Institute of Physics, Jagiellonian University,
PL-30-059 Cracow, Poland

^c Institut für Kernphysik, Forschungszentrum Jülich,
52425 Jülich, Germany

^d Jülich Center for Hadron Physics,
Forschungszentrum Jülich, 52425 Jülich, Germany

^e Zentralinstitut für Engineering, Elektronik und Analytik,
Forschungszentrum Jülich, 52425 Jülich, Germany

^f Physikalisches Institut, Friedrich-Alexander-Universität
Erlangen-Nürnberg, Erwin-Rommel-Str. 1,
91058 Erlangen, Germany

ABC effect and Resonance Structure in the Double-Pionic Fusion to ${}^3\text{He}$

E. Perez del Rio, M. Bashkanov, and H. Clement, *for the WASA-at-COSY Collaboration*

In 1960 Abashian, Booth and Crowe published their measurements of the reaction $pd \rightarrow {}^3\text{He} X$ in the energy range $T_p = 624 - 743$ MeV ($\sqrt{s} = 3.21 - 3.28$ GeV). Since they used just a single-arm magnetic spectrometer as detector, their measurement was inclusive, *i.e.* single and double pion production could be identified and separated only kinematically. Nevertheless, they were able to observe an unusual enhancement right at the kinematic threshold of the two-pion phase space. In subsequent experiments at various places it could be shown that such a low-mass enhancement in the $\pi\pi$ -invariant mass spectrum shows up generally in the fusion to light nuclei, if an isoscalar pion pair is produced. Later-on extensive single-arm measurements at Saclay demonstrated that in case of the double-pionic fusion to ${}^3\text{He}$ the maximal threshold enhancement occurs at $T_p \approx 0.9$ GeV ($\sqrt{s} \approx 3.36$ GeV) and fades away beyond 1 GeV ($\sqrt{s} > 3.4$ GeV). Since there was no satisfying theoretical explanation for this phenomenon, it finally was called ABC effect after the initials of the first authors, who reported about this phenomenon.

In exclusive and kinematically complete measurements of the reaction $pn \rightarrow d\pi^0\pi^0$, $pn \rightarrow d\pi^+\pi^-$ and $dd \rightarrow {}^4\text{He}\pi^0\pi^0$ with WASA at COSY we have demonstrated recently that the ABC effect is tightly correlated with a narrow resonance structure of $I(J^P) = 0(3^+)$ in the total cross section. In the basic reaction, the fusion to the deuteron, the structure – denoted in the following by d^* – appears at $\sqrt{s} = 2.37$ GeV with a width of $\Gamma \approx 70$ MeV. In the ${}^4\text{He}$ case the structure appears at the same energy above threshold, but with an increased width, which may be understood as being due to the Fermi motion in initial and final nuclei (collision damping).

In order to complete our ABC studies on light nuclei we investigated now also the ${}^3\text{He}$ case with WASA by measuring the $pd \rightarrow {}^3\text{He}\pi^0\pi^0$ reaction at $T_p = 1.0$ GeV ($\sqrt{s} = 3.4$ GeV) and the $dd \rightarrow {}^3\text{He}\pi^0\pi^0 + n_{\text{spectator}}$ reaction at $T_d = 1.7$ GeV. The latter covers the energy range $\sqrt{s} = 3.2 - 3.5$ GeV, *i.e.* the full range of the ABC effect.

Fig. 1 exhibits some of our preliminary results. On top the energy dependence of the total cross section is displayed. At the bottom we show the $\pi^0\pi^0$ -invariant mass ($M_{\pi^0\pi^0}$) spectrum at two different energies. Again we observe a resonance-like structure in the total cross section, which is correlated with the appearance of the ABC effect. However, the detailed analysis shows that the resonance-like structure is made of two Lorentzians. The higher-energetic, large one (long-dashed curve in Fig. 1) is due to the conventional t -channel $\Delta\Delta$ process, which produces both a low-mass and and high-mass bump in the $M_{\pi^0\pi^0}$ spectrum, whereas the lower-energetic one, which is correlated with the proper ABC effect is substantially smaller. This is understood from the fact that in the ${}^3\text{He}$ case the isovector $\Delta\Delta$ process is very strong.

In retrospect it may have been fortunate that the

Berkeley cyclotron did not deliver higher energies, so that Abashian, Booth and Crow could only reach the low-energy region of the resonance structure, where the ABC effect turns now out to be most pronounced.

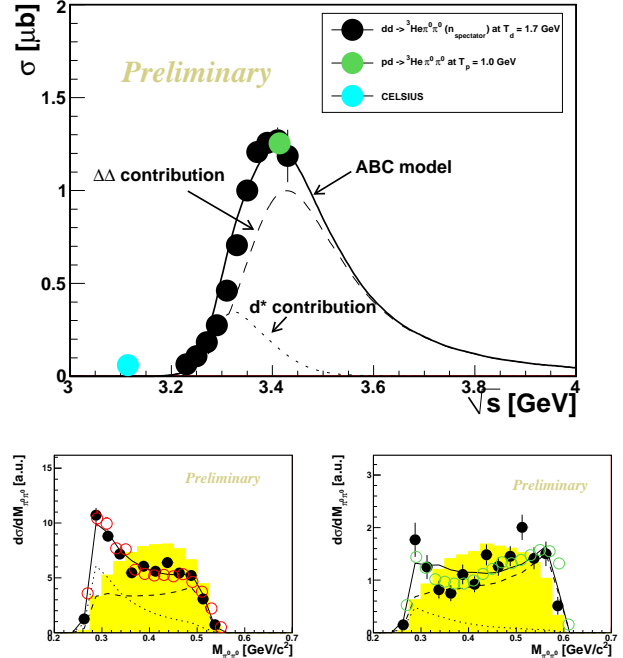


Fig. 1: Preliminary results for the $pd \rightarrow {}^3\text{He}\pi^0\pi^0$ reaction. Top: Energy dependence of the total cross section. The black filled circles denote the results from the analysis of the $dd \rightarrow {}^3\text{He}\pi^0\pi^0 + n_{\text{spectator}}$ reaction, the green filled circle originates from the analysis of $pd \rightarrow {}^3\text{He}\pi^0\pi^0$ measurement at $T_p = 1$ GeV. The blue solid circle gives a measurement at CELSIUS. Dashed and dotted curves denote calculations of the t -channel $\Delta\Delta$ process and of the d^* resonance process, respectively. The solid curves gives the sum of both processes. Bottom: Distributions of the $\pi^0\pi^0$ -invariant mass $M_{\pi^0\pi^0}$ at $\sqrt{s} = 3.34$ GeV (left), where the ABC effect is at maximum, and at $\sqrt{s} = 3.40$ GeV (right), where already the t -channel $\Delta\Delta$ process is dominant. The open circles on the left denote results of a CELSIUS/WASA measurement. The open circles on the right panel give the result of the $pd \rightarrow {}^3\text{He}\pi^0\pi^0$ measurement at $T_p = 1$ GeV. The meaning of the curves is the same as above.

B. Kłos¹ and I. Ciepał² for the WASA-at-COSY Collaboration

The experiment to investigate the $^1\text{H}(\vec{d}, pp)n$ breakup reaction using the deuteron beam of 340, 380 and 400 MeV and the WASA detector has been successfully performed at the Cooler Synchrotron COSY-Jülich in January 2013. The main goal of the experiment was the detailed study of various aspects of few-nucleon dynamics in the medium energy region, with a particular emphasis on relativistic effects and their interplay with three nucleon forces. Calculations including different pieces of nucleon-nucleon dynamics like the three nucleon force 3NF, the long-range Coulomb interaction or relativistic effects, predict their influence to reveal with different strength at different parts of the phase space. The cross section is expected to be very sensitive to all these effects. Previous measurements of the cross sections at different deuteron beam energies have demonstrated that an inclusion of 3N and Coulomb forces in the theoretical calculations improves the description of the experimental data [1]. In recent years the relativistic treatment of the breakup reaction in 3N systems was developed using the NN potential [2] and this approach has also been extended for calculations including 3NF [3]. It was shown that in some particular regions of the breakup phase space, relativistic effects can increase or decrease the calculated breakup cross sections by up to 60%. At the same time the effects of 3NF may change certain observables by a similar factor. The relativistic effects and their interplay with 3NF become more important with increasing available energy in the three nucleon system. Therefore, investigations at relatively high energies are important to confirm the theoretical predictions for relativistic effects and to unambiguously fix the relevance of the 3NF.

In the experiment the trigger conditions allowed for selection of a single particle or two coincident charged particles. The following reaction channels were measured: dp elastic scattering, $dp \rightarrow ppn$ breakup and the electromagnetic processes: $dp \rightarrow ^3\text{He} + \gamma$, $dp \rightarrow dp\gamma$. During the measurement the beam intensity was about $(1.3\text{-}1.4) \cdot 10^8$ deuterons in the flat top. The total input trigger rate was about 60 kHz, while the accepted trigger rate was about 30 kHz. Our triggers were designed to include all possible classes of coincidences of two charged particles in order to avoid any bias in measurement of the breakup reaction. The luminosity was $\sim 10^{29}/\text{s/cm}^2$ and we collected 20.1 TB data during 1.5 weeks of measurements. The preliminary results obtained with use the WASA detector are presented.

The first step of data analysis consists of selecting interesting particles *i.e.* two protons from the breakup process and deuteron-proton pairs from elastic scattering channel. Identification of protons and deuterons in Forward Detector is performed with the ΔE - E technique. In the whole range of energies, a clear separation between the loci of protons and deuterons is observed in the Forward Detector. Almost all deuterons from elastic dp scattering are stopped in the fourth plane of the Forward Range Hodoscope (FRH). The breakup and elastic scattering events belong to three classes, where the first one consists of events registered in Forward Detector. The second class of events constitutes one particle in the Forward Detector and the second in the Central Detector. Both particles detected in the Central Detector belong to the third class of events. After the selection of the proton-proton

coincidences and having performed the energy calibration, any kinematical configuration of the breakup reaction within the angular acceptance of the detection system can be analyzed. The configuration is defined by the emission angles of the two outgoing protons: two polar angles θ_1 and θ_2 and the relative azimuthal angle ϕ_{12} . The choice of the angular ranges for integration of events depends on statistics and, on other hand, variations of the observable within this range. The kinematical spectra E_1 versus E_2 are shown in Fig. 1, left panel. Events for configurations of interest are projected onto the kinematical curve corresponding to the point-like, central geometry. Only events lying along kinematical curve within the band of D values ranging from -12 MeV to 12 MeV were taken into account. The D denoting the distance of the (E_1, E_2) point from the kinematical curve. The rate of events is obtained as function of the arc-length S measured along the kinematic curve (Fig. 1, right panel). These rates have to be normalized using rates of the elastic scattering events, the known cross-section for this process [4] and the detector efficiency.

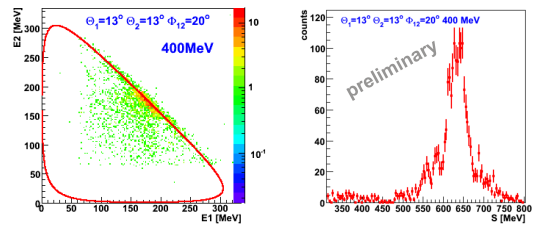


Fig. 1: *Left panel:* E_1 - E_2 coincidence spectra of the two protons registered at one kinematical configuration ($\theta_1=13^\circ \pm 1^\circ$, $\theta_2=13^\circ \pm 1^\circ$, and $\phi_{12}=20^\circ \pm 5^\circ$) in measurements at 400 MeV deuteron beam energy. The solid line shows a three-body kinematical curve, calculated for the central values of the experimental angular ranges. *Right panel:* an example of the preliminary non-normalized rate of breakup events obtained for the chosen kinematical configuration (see left panel) are presented as a function of the S value (arc-length along the kinematics with the starting point at the E_2 minimum).

The data analysis is continued with the aim to determine the differential cross sections for the the deuteron breakup process in the $d+p$ system at energies of 340, 380 and 400 MeV. The data will be compared to the relativistic theoretical calculations as soon as they become available for the $^1\text{H}(\vec{d}, pp)n$ breakup reaction.

We acknowledge support by the Polish National Science Center through grant No. 2012/05/E/ST2/02313 and by the FFE funds of the Forschungszentrum Jülich.

¹University of Silesia, PL-40007 Katowice, Poland

²Jagiellonian University, PL-30059 Kraków, Poland

References:

- [1] S. Kistryn and E. Stephan, *J. Phys. G: Nucl. Part. Phys.* **40**, 063101 (2013)
- [2] H. Witała H., R. Skibinski and J. Golak, *The European Physical Journal A* **30**, 369 (2006)
- [3] H. Witała et al., *Phys. Rev. C* **83**, 044001 (2011)
- [4] K. Ermisch et al., *Rev. C* **68**, 051001(R) (2003)

Measurement of total and differential cross sections of $p + d \rightarrow {}^3\text{He} + \eta$ with WASA-at-COSY*

F. Bergmann¹, K. Demmich¹, P. Goslawski¹, P. Hüsemann¹, N. Hüskens¹, A. Khoukaz¹, A. Passfeld¹, F. Schepers¹, and A. Täschner¹

While for $p + d \rightarrow {}^3\text{He} + \eta$ a rich data set exists for energies close to threshold [1, 2, 3, 4, 5] the situation is different for higher excess energies where only a few data points exist. In this regime of higher energies, i.e. $Q = 20 - 120$ MeV, the ANKE and WASA/PROMICE data show a plateau in the excitation function [6, 7]. Although still consistent with this cross section plateau when considering the statistical and systematic uncertainties, the one single data point of the GEM experiment at 48.8 MeV might hint for an increase of the cross section [8]. Fig. 1 shows the total cross sections for $p + d \rightarrow {}^3\text{He} + \eta$ at 0 – 120 MeV excess energy.

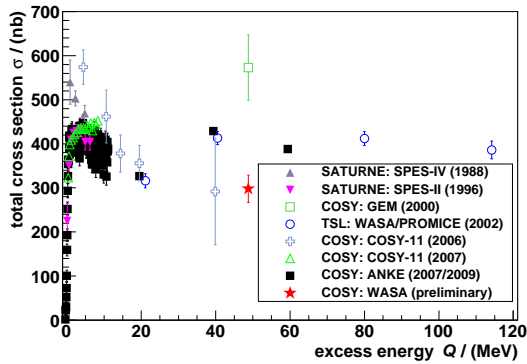


Fig. 1: Total cross section of $p + d \rightarrow {}^3\text{He} + \eta$ as a function of the excess energy. All shown uncertainties are without systematic uncertainties from absolute normalization.

Calculations based on either a one-step or a two-step model fail to explain the observed total cross section and forward peaked angular distributions of this reaction at the same time. Therefore, new calculations based on a boson exchange model were proposed, for which new high quality data at intermediate excess energies are required [9].

Thus, data for the reaction $p + d \rightarrow {}^3\text{He} + \eta$ have been taken using the WASA-at-COSY installation to determine the total and differential cross sections at $Q = 48.8$ MeV ($T_p = 980$ MeV) and 59.8 MeV ($T_p = 1000$ MeV) [10]. The emitted ${}^3\text{He}$ of the two particle reaction $p + d \rightarrow {}^3\text{He} + \eta$ are identified via their energy loss in two different layers of the WASA-at-COSY Forward Detector. The ${}^3\text{He}$ missing mass distribution is fitted by a Monte Carlo cocktail considering the reaction of interest as well as multi-pion production channels. After background subtraction the number of ${}^3\text{He}-\eta$ events for 25 equally spaced $\cos \vartheta_{\text{CMS}}^{\eta}$ bins is determined. To minimize the systematic uncertainties the absolute normalization has been performed using the ANKE data point at $Q = 59.4$ MeV while a relative normalization of the new data has been done using the $p + d \rightarrow {}^3\text{He} + \pi^0$ reaction. A preliminary cross section ratio for the η meson production at $Q = 48.8$ MeV was determined to:

$$\frac{\sigma_{980 \text{ MeV}}^{\eta}}{\sigma_{1000 \text{ MeV}}^{\eta}} = \frac{\sigma_{980 \text{ MeV}}^{\pi^0}}{\sigma_{1000 \text{ MeV}}^{\pi^0}} \cdot \frac{N_{1000 \text{ MeV}}^{\pi^0}}{N_{980 \text{ MeV}}^{\pi^0}} \cdot \frac{N_{980 \text{ MeV}}^{\eta}}{N_{1000 \text{ MeV}}^{\eta}} = 0.77 \pm 0.06. \quad (1)$$

Here the numbers $N_{T_p}^i$ correspond to the acceptance corrected meson yields. Fig. 1 shows the preliminary result for

the total cross section at $Q = 48.8$ MeV. The displayed uncertainty includes statistics as well as systematics, the latter originating from the slightly different shapes of the differential cross sections of WASA-at-COSY and ANKE at 59.8 MeV. Fig. 2 shows the determined differential cross sections for $Q = 48.8$ MeV and $Q = 59.8$ MeV compared to existing data from ANKE and GEM (scaled by 0.52). While the excitation function is almost constant at excess energies above 60 MeV the new data point indicates the presence of a cross section variation in the region of 20 – 60 MeV excess energy.

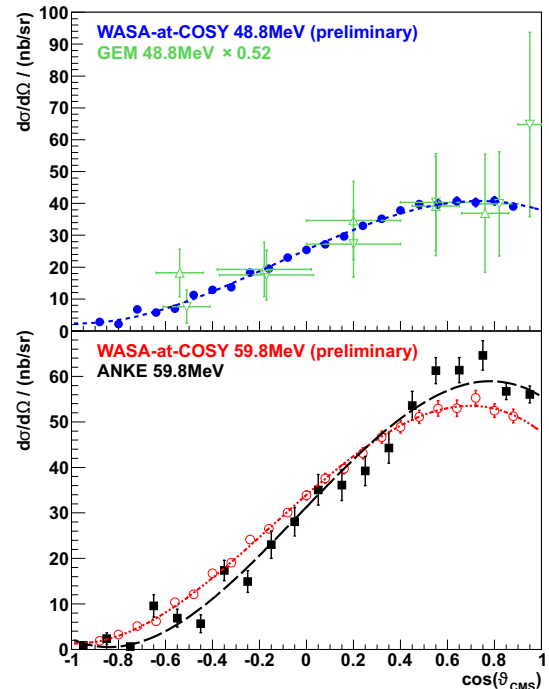


Fig. 2: Differential cross sections for $Q = 48.8$ MeV and $Q = 59.8$ MeV. The results from WASA-at-COSY are compared to those from ANKE and GEM (scaled by 0.52).

References:

- [1] T. Mersmann *et al.*, Phys. Rev. Lett. **98**, 242301 (2007).
- [2] J. Smyrski *et al.*, Phys. Lett. B **649**, 258 (2007).
- [3] J. Berger *et al.*, Phys. Rev. Lett. **61**, 919 (1988).
- [4] B. Mayer *et al.*, Phys. Rev. C **53**, 2068 (1996).
- [5] H.-H. Adam *et al.*, Phys. Rev. C **75**, 014004 (2007).
- [6] T. Rausmann *et al.*, Phys. Rev. C **80**, 017001 (2009).
- [7] R. Bilger *et al.*, Phys. Rev. C **65**, 044608 (2002).
- [8] M. Betigeri *et al.*, Phys. Lett. B **472**, 267 (2000).
- [9] N. G. Kelkar *et al.*, Rep. Prog. Phys. **76**, 066301 (2013).
- [10] A. Passfeld, diploma thesis, Westfälische Wilhelms-Universität Münster, Germany, (2010).

* Supported by COSY-FFE

¹ Institut für Kernphysik, Westfälische Wilhelms-Universität Münster, 48149 Münster, Germany

Investigation of the $p + d \rightarrow {}^3\text{He} + \eta'$ reaction at WASA-at-COSY*

N. Hüsken,[†] F. Bergmann,[†] K. Demmich,[†] P. Goslawski,[†] P. Hüsemann,[†] A. Khoukaz,[†] F. Schepers,[†] and A. Täschner[†]
for the WASA-at-COSY-Collaboration

The η' (958) meson is of special interest, because its higher mass compared to other pseudoscalar mesons is directly related to the $U_A(1)$ problem of QCD. Recent theoretical works discuss studies on the formation of η' -mesic nuclei as a possibility to investigate an in-medium modification of the η' mass [1]. Such a modification could shed light on the η' mass generation mechanism.

With the WASA-at-COSY setup two test beam times on proton-deuteron collisions were carried out at proton kinetic energies of $T_p = 1800$ MeV and $T_p = 1850$ MeV respectively to investigate the possibility to perform studies on the η' production in the proton-deuteron fusion at this installation.

Since the production cross section for the $p + d \rightarrow {}^3\text{He} + \eta'$ reaction is estimated to be rather small compared to the expected multi-pion background, an exceptionally careful calibration of the WASA Forward Detector was performed.

The two data sets were analysed using the missing mass technique, for which the four momenta of the ${}^3\text{He}$ nuclei were measured with the WASA Forward Detector. This was done by measuring the azimuthal and polar scattering angles ϕ and ϑ with the Forward Proportional Counter (FPC), matching the tracks in the Forward Hodoscopes and calculating the kinetic energy of the ${}^3\text{He}$ particles by measuring the deposited energy in the Forward Range Hodoscope (FRH).

To identify the ${}^3\text{He}$ particles, cuts on the energy loss in various layers of the forward detector were used, starting from the first layer of the Trigger Hodoscope up to third layer for the FRH.

In a next step the resulting missing mass spectra were analysed for different bins of $\cos \vartheta_{cm}^{{}^3\text{He}}$ and for stopping of the ${}^3\text{He}$ particles in different layers of the FRH. The background resulting from multi-pion production in the missing mass interval between $0.90 \text{ GeV}/c^2$ and $0.98 \text{ GeV}/c^2$ was found to be lowest for stops in layer two of the FRH and for $\cos \vartheta_{cm}^{{}^3\text{He}}$ values between -0.3 and 0.3 . This is also the region where the WASA detector provides the best missing mass resolution.

In Fig. 1 corresponding missing mass plots are shown, which were fitted with a polynomial, excluding the region in which the η' -meson would be expected. In case of both excess energies signals from the η' meson production are obtained with a significance of 4.3σ and 5.1σ respectively. Combining both analyses, the level of significance can be raised to 7.0σ .

In order to gain information on the production cross section for the $p + d \rightarrow {}^3\text{He} + \eta'$ reaction, the production of the $\omega(782)$ meson can be used for normalization purposes. The number of $p + d \rightarrow {}^3\text{He} + \omega$ events can be extracted for $\cos \vartheta_{cm}^{{}^3\text{He}}$ from -1 to -0.4 (-0.5 respectively) (see Fig. 2). Extrapolating these to $\cos \vartheta_{cm}^{{}^3\text{He}} = -1$, the data from Ref. [2] allow for the determination of the luminosity and therefore for a normalization as well as for the extraction of differential cross sections for the ω production.

Applying this normalization on the η' candidate events will

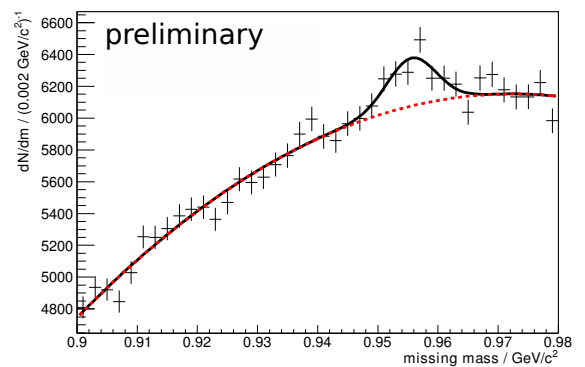
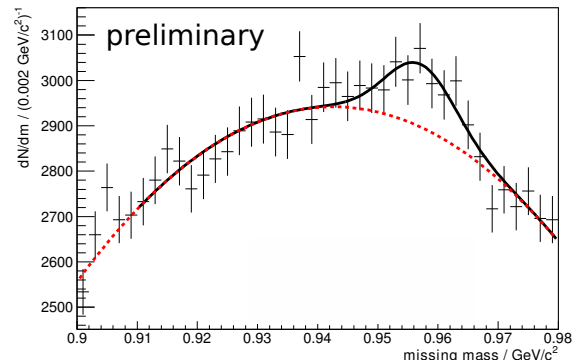


Figure 1: Missing mass plots for $T_p = 1800$ MeV (top) and $T_p = 1850$ MeV (bottom). Dashed lines represent polynomial fits.

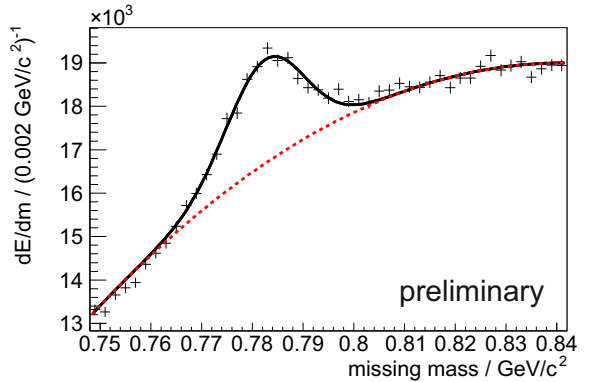


Figure 2: Missing mass plot for $T_p = 1800$ MeV for $-1 \leq \cos \vartheta_{cm}^{{}^3\text{He}} < -0.4$. Dashed line represents a polynomial fit.

allow to extract ${}^3\text{He} + \eta'$ production cross sections in the $\cos \vartheta_{cm}^{{}^3\text{He}}$ -interval from -0.3 to 0.3 for both excess energies.

References

- [1] H. Nagahiro *et al.*, Phys. Rev. C **85**, 032201(R), (2012).
- [2] R. Wurzinger *et al.*, Phys. Rev. C **51**, 443-446, (1995).

*Supported by COSY-FFE

[†]Institut für Kernphysik Westfälische Wilhelms-Universität, 48149 Münster, Germany

Search for ${}^4\text{He}-\eta$ bound state via $dd \rightarrow {}^3\text{He}\eta\pi^-$ and $dd \rightarrow {}^3\text{He}\eta\pi^0$ reaction with the WASA-at-COSY facility

M. Skurzok^a, W. Krzemien^a and P. Moskal^a for the WASA-at-COSY collaboration

In November 2010, the search for a ${}^4\text{He}-\eta$ bound state was performed by measuring the excitation function of the $dd \rightarrow {}^3\text{He}\eta\pi^0 \rightarrow {}^3\text{He}\eta\gamma\gamma$ and $dd \rightarrow {}^3\text{He}\eta\pi^-$ reactions in the vicinity of the η production threshold. The measurement was carried out using a ramped beam technique. The beam momentum was varying continuously from 2.127 GeV/c to 2.422 GeV/c which corresponds to a range of excess energies $Q \in (-70, 30)$ MeV.

Independent analyses for the $dd \rightarrow {}^3\text{He}\eta\pi^0 \rightarrow {}^3\text{He}\eta\gamma\gamma$ and $dd \rightarrow {}^3\text{He}\eta\pi^-$ reactions were carried out. The ${}^3\text{He}$ for both cases was identified in the Forward Detector based on the ΔE - E method. The neutral pion π^0 was reconstructed in the Central Detector from the invariant mass of two gamma quanta originating from its decay while the π^- identification in Central Detector was based on the measurement of the energy loss in the Plastic Scintillator combined with the energy deposited in the Electromagnetic Calorimeter. Neutron and proton were identified via the missing mass technique. The appropriate spectra with applied cuts are presented in Fig. 1.

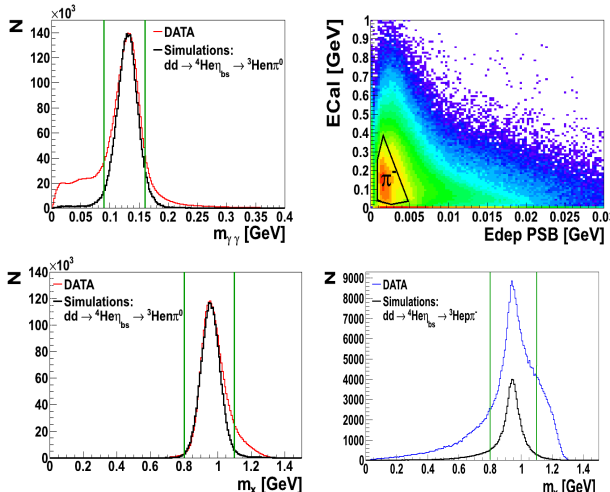


Fig. 1: π^0 and π^- identification (upper panel). Proton and neutron identification (lower panel). The data were marked with red and blue lines, the Monte Carlo simulations of the signal are marked with the black line, while the applied cuts are marked in green.

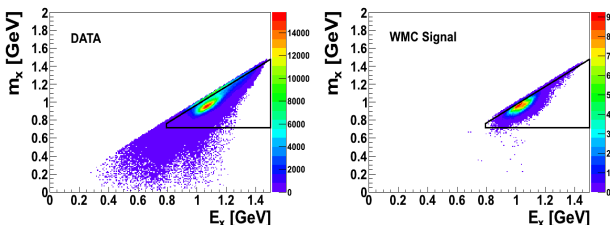


Fig. 2: Missing mass m_x vs. missing energy E_x for data (left panel) and Monte Carlo (right panel). The applied cut is marked in black.

In case of the $dd \rightarrow {}^3\text{He}\eta\pi^0$ reaction, before particle identification, an additional cut on the $m_x(E_x)$ spec-

trum was applied as shown in Fig. 2 (left). The cut is based on Monte Carlo simulations and is presented in Fig. 2 (right).

In case of the $dd \rightarrow {}^3\text{He}\eta\pi^-$ reaction an additional coplanarity cut was applied. As a measure of the coplanarity the angle between the vector $\vec{p}_{beam} - \vec{p}_{{}^3\text{He}}$ and the cross product of the vectors \vec{p}_1 and \vec{p}_2 : $\theta_{k,1x2} = \angle(\vec{p}_{beam} - \vec{p}_{{}^3\text{He}}, \vec{p}_1 \times \vec{p}_2)$ was defined. In the case of coplanarity $\theta_{k,1x2} = 90^\circ$. In data we applied a cut $\theta_{k,1x2} \in (90 \pm 5)^\circ$ which is presented in Fig. 3.

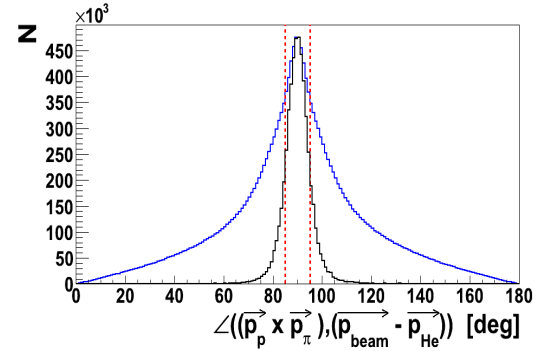


Fig. 3: Distribution of the coplanarity observable determined for simulations of $dd \rightarrow {}^3\text{He}\eta\pi^-$ (black line) and for experimental data (blue line). The cut applied to the data - $\theta_{k,1x2} \in (90 \pm 5)^\circ$ - is marked by the vertical dotted red lines.

In order to select events corresponding to the production of bound states, cuts in the ${}^3\text{He}$ CM momentum, nucleon CM kinetic energy, pion CM kinetic energy and the opening angle between nucleon-pion pair in the CM were applied based on Monte Carlo simulations. These cuts are presented in Fig. 4.

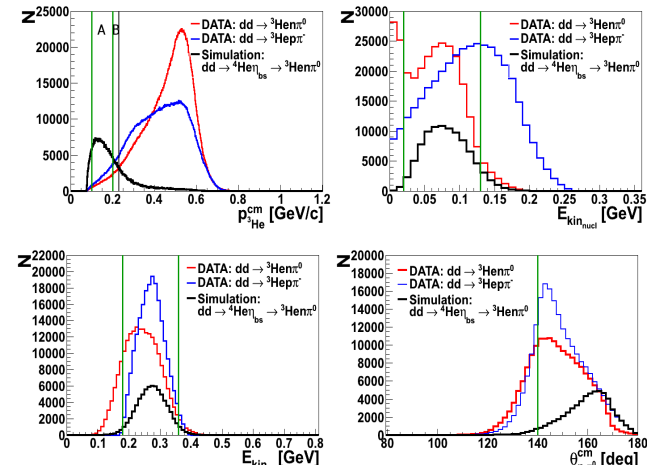


Fig. 4: Spectrum of $p_{{}^3\text{He}}^{cm}$ (left upper panel), $E_{kin_{nucl}}^{cm}$ (right upper panel), $E_{kin_\pi}^{cm}$ (left lower panel) and $\theta_{nucl,\pi}^{cm}$ (right lower panel). Data are shown in red and blue for $dd \rightarrow {}^3\text{He}\eta\pi^0$ and $dd \rightarrow {}^3\text{He}\eta\pi^-$ reaction, respectively. Monte Carlo simulations of signal are shown in black, while the applied cuts are marked with the green lines.

The excitation functions for both reactions were determined for a "signal rich" region corresponding to momenta of the ${}^3\text{He}$ in the CM system with $p_{{}^3\text{He}}^{\text{cm}} \in (0.1, 0.2)\text{GeV}/c$ and for a "signal poor" region with $p_{{}^3\text{He}}^{\text{cm}} \in (0.2, 0.23)\text{GeV}/c$ which are marked with (A) and (B) in the left upper panel in Fig. 4, respectively. The excitation functions for the $dd \rightarrow {}^3\text{He}\pi^0$ and $dd \rightarrow {}^3\text{He}\pi^-$ reactions are presented in Fig. 5.

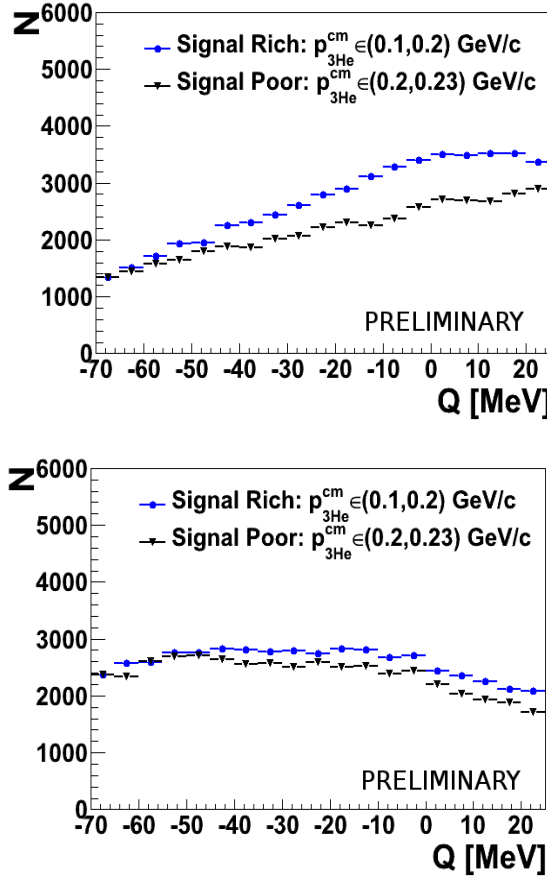


Fig. 5: Excitation function for the $dd \rightarrow {}^3\text{He}\pi^0$ reaction (left panel) and the $dd \rightarrow {}^3\text{He}\pi^-$ reaction (right panel). The "signal rich" region is shown in blue while the "signal poor" region normalized to the first bin of the "signal rich" region is shown in black. The analysis is based on the whole data sample.

The preliminary results presented in Fig. 5 reveal no structure which could be interpreted as a signature of a bound state. The shape of the spectra in the "signal rich" and "signal poor" regions differs from each other. A detailed studies of the background and signal channels are in progress.

We acknowledge support by the Foundation for Polish Science - MPD program, by the Polish National Science Center through grant No. 2011/01/B/ST2/00431 and by the FFE grants of the Forschungszentrum Jülich.

^a M. Smoluchowski Institute of Physics, Jagiellonian University, 30-059 Cracow, Poland

Studies of Systematic Uncertainties of Polarization Estimation for Experiments with the WASA Detector at COSY

I. Ozerianska^a, P. Moskal^a, M. Hodana^a for the WASA-at-COSY collaboration

The production mechanism of the η meson and meson-nucleon final state interaction for the $\vec{p}p \rightarrow pp\eta$ reaction can be studied via measurements of the analyzing power $A_y(\theta)$. Up to now, only three experiments [1–4] investigated A_y and the results have poor statistics and large uncertainties.

For a precise study of the η meson production in terms of $A_y(\theta)$, in November 2010 a high statistics sample of $\vec{p}p \rightarrow pp\eta$ has been collected using the azimuthally symmetric WASA-at-COSY detector [5]. The measurement was performed using polarized protons for two beam momenta corresponding to excess energies of 15 MeV and 72 MeV. Monitoring of the beam polarization, the luminosity and the detector performance, was done using the $\vec{p}p \rightarrow pp$ reaction. Additionally, in order to control the effects caused by potential asymmetries in the detector setup the beam direction of the polarization was flipped from cycle to cycle.

The degree of polarization was determined based on the analysis of elastic scattering reaction, for which the values of the analyzing power have been extracted from the EDDA [7] results. After the identification of protons the number of events corresponding to the $\vec{p}p \rightarrow pp$ reaction, has been determined for each angular bin $N(\theta, \varphi)$ separately. The polarization, $P(\theta)$, can be written as

$$P(\theta) \equiv \frac{1}{A_y(\theta) \cdot \cos(\varphi)} \cdot \epsilon(N(\theta, \varphi), N(\theta, \varphi + \pi)), \quad (1)$$

where ϵ denotes the asymmetry, which is defined as:

$$\frac{N(\theta, \varphi) - N(\theta, \varphi + \pi)}{N(\theta, \varphi) + N(\theta, \varphi + \pi)} \equiv \epsilon(N(\theta, \varphi), N(\theta, \varphi + \pi)). \quad (2)$$

The data analysis shows that the polarization was stable during the whole measurement time, but its value differs for the spin up and the spin down mode. In the part of the measurement where the unpolarized beam was used, the calculated value of the polarization slightly deviates from zero. The systematic uncertainty in the determination of the polarization might be due to the false number of events in the individual θ_{CM} ranges, originating from the possible misalignment of the beam's and/or target's position.

One of the ways to control the location of the vertex position in the experiment was proposed in [6]. Using this method we have extracted the average vertex position x_v, y_v, z_v for each run. To learn how the vertex position influences the determination of the polarization we have implemented in the simulations a shift of the vertex coordinate. The distribution of the polarization as a function of the applied shift is done for each of three coordinates separately and the result is shown in Fig. 1 (left).

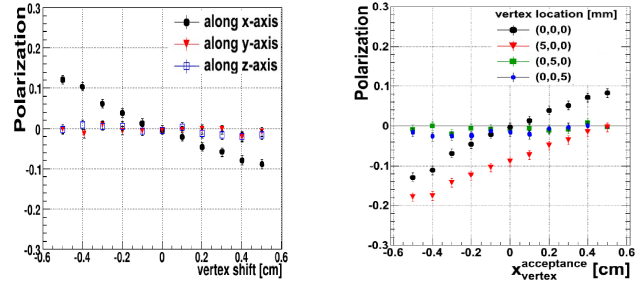


Fig. 1: Left: Polarization as function of vertex shift along the x-, y- and z-axis (see legend). Right: Polarization as function of the vertex position corrected for acceptance. Vertex positions are given in the legend.

The simulated data for each vertex position (as indicated in the legend), have been acceptance corrected assuming different values of the x_v coordinate, $x_{vertex}^{acceptance}$. The analysis shows that a change of the y_v or z_v coordinates does not affect the result of the polarization. However, the polarization strongly depends on a change in the x_v coordinate. Figure 1 (right) shows that to achieve uncertainties of the polarization of about 0.03 the accuracy of the vertex position has to be controlled with a precision of better than 1mm. Furthermore, the analysis shows that a shift of a given coordinate within a [-0.5, 0.5] cm window does not affect the extraction of remaining coordinates [8]. From Fig. 2 it can be seen at once that the vertex position in both coordinates x and y is stable.

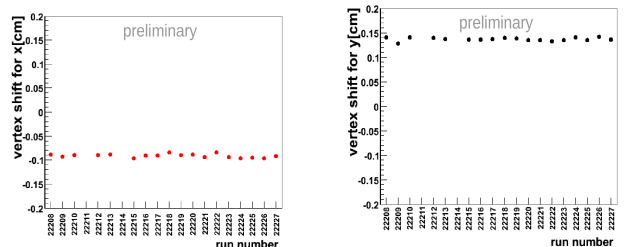


Fig. 2: Vertex position extracted from the experimental data. Each plot shows a different coordinate, calculated with the method adopted from [6].

The distribution of the polarization as a function of the scattering angle of the forward going proton calculated in the center of mass system, θ_{CM} , made for different vertex positions (x - coordinate of the vertex) is shown in Fig. 3. One can see that for a higher θ_{CM} angle ($\theta_{CM} > 38^\circ$), the polarization starts to deviate from expected value of zero when the vertex is shifted by more than 0.5 cm along the x-direction.

Furthermore, the influence of the tilt of the beam on the polarization value has been studied. The maximum allowed range of tilts of the beam at WASA-at-COSY is between -0.05 mrad and 0.05 mrad (symmetrically

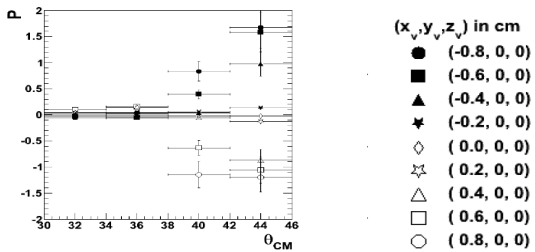


Fig. 3: Distribution of the polarization as a function of the θ_{CM} angle.

around the z-axis) [9]. In Fig. 4, the polarization as a function of the tilt angle α in x and y is shown. There are no effects observed in the studied range of α ($\alpha \in [-0.5; 0.5]$ mrad) except that the polarization slightly differs from zero (up to 0.01).

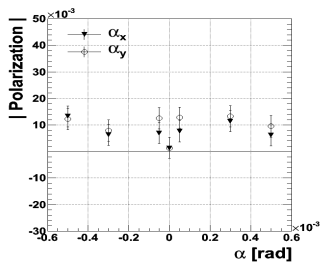


Fig. 4: The value of the polarization as a function of the tilt of the beam tilt angle α .

In this report methods to monitor the location of the vertex have been demonstrated and it was shown how the mis-location of the vertex impacted the obtained degree of polarization. The study concluded that in order to have the systematic uncertainty of the polarization smaller than 0.01, we need to control the position of the interaction point with a precision better than 1 mm. Due to the high sensitivity of the result to the scattering angle it is better to calculate the polarization taking into account only scattering angles smaller than $CM_s = 38^\circ$. Furthermore, the investigation shows that the tilt of the beam does not influence the degree of polarization significantly.

We acknowledge support by the Polish National Science Center through grant No. 2011/03/B/ST2/01847, by the FFE grants of the Forschungszentrum Juelich, by the EU Integrated Infrastructure Initiative Hadron-Physics Project under contract number RII3-CT-2004-506078 and by the European Commission under the 7th Framework Programme through the Research Infrastructures action of the Capacities Programme, Call: FP7- INFRASTRUCTURES-2008-1, Grant Agreement N. 227431.

References:

- [1] R. Czyżkiewicz et al., Phys. Rev. Lett. **98** (2007) 122003.
- [2] F. Balestra et al., Phys. Rev. **C 69** (2004) 064003.
- [3] P. Winter et al., Eur. Phys. J. **A 18** (2003) 355.
- [4] P. Winter et al., Phys. Lett. **B 544** (2002) 251258.
- [5] P. Moskal, M. Hodana, J.Phys.Conf.Ser.295:012080, 2011.
- [6] L. Demirors, PhD Hamburg University (2005)
- [7] M. Altmeier et al., Phys. Rev. Lett. **85** (2000).
- [8] M. Hodana et al., Acta Phys. Polon. Supp. **6** (2013) 1041-1052
- [9] D. Prashun, private communication (2013)

^a M. Smoluchowski Institute of Physics, Jagiellonian University, 30-059 Cracow, Poland

Energy Calibration of the WASA-at-COSY Forward Detector*

K. Demmich[†] F. Bergmann[†] P. Goslawski[†] P. Hüsemann[†] N. Hüskens[†] F. Schepers[†] A. Täschner[†] and A. Khoukaz[†]
for the WASA-at-COSY-Collaboration

The WASA-at-COSY detector setup allows for detailed studies on neutral and charged decays of the η meson. In beam times between 2008 and 2012 a large data set of η events has been measured in proton proton collisions ($pp \rightarrow pp\eta$) at an excess energy of 55.2 MeV. This data set provides the opportunity to study rare decays as well as forbidden ones like $\eta \rightarrow \pi^0 + e^+ + e^-$. While each analysis relies on a well calibrated detector to obtain exact kinematic information, this is especially true for investigations of forbidden decays.

The protons scattered in an η production process are detected with the WASA forward detector system and the kinetic energy is reconstructed on the basis of the deposited energies within the particular layers of the Forward Range Hodoscope (FRH). Hence, a careful energy calibration of this detector part is crucial for a proton identification and the separation of background events and η events.

The reconstruction of the energy loss ΔE in one detector element is performed via a calibration function which takes into account angular effects and a second function correcting non linearities of the detector system. The calibration parameters are determined by comparing measured and simulated proton bands in energy loss plots, where for each particle the deposited energy ΔE in one layer is plotted versus the energy loss in another layer (Fig. 1). Assuming an ideally calibrated detector, the simulated and measured proton bands should be identical. In order to quantify the deviation between these two distributions, in a first step polynomial fits $f_{MC}(x)$ are applied to the simulated data. A standard fitting method is based on minimizing the averaged squared distance along the ordinate – normalized to the standard deviation – between the data points and the fitting function:

$$\chi^2_{\text{red}} = \frac{1}{\text{Ndof}} \sum_{\text{Points}} \delta_i^2 / \sigma^2 \quad (1)$$

with $\delta_i = (y_i - f_{MC}(x_i))$. x, y may represent any combination of $\Delta E_{\text{FRH}1,2,3,4,5}$.

For the fitting of the energy loss histograms, this method has to be adjusted:

- The standard deviation $\sigma(x)$ is energy dependent and has to be obtained for each x-bin by a gaussian fit to a projection along the y-axis.
- To reduce the effect of background events with large δ_i^2 as considered in equation (1) this value is limited to a predefined maximum like $(n \cdot \sigma)^2$, i.e., just an $n\sigma$ environment around the function is effectively fitted, as points being far away from the expected distribution just contribute with a constant value.
- The data sets are represented by histograms rather than single points. Each histogram bin i with the

content w_i is handled as w_i data points located at the bin center (x_i, y_i) .

Considering these aspects leads to the following definition:

$$\chi^2_{\text{red}} = \frac{1}{\text{Ndof}} \sum_{\text{Bins}} w_i / \sigma^2(x_i) \cdot \min(\delta_i^2, n^2). \quad (2)$$

By minimizing this value a function f_{MC} is fitted to the distribution (Fig. 1).

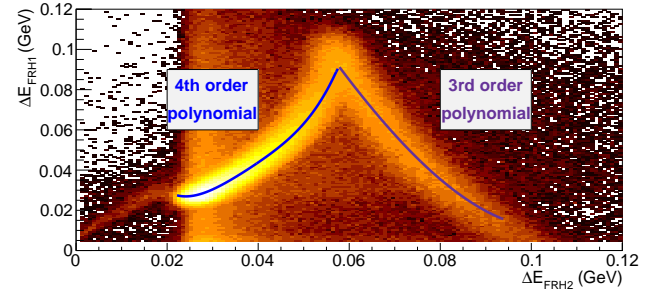


Figure 1: Energy loss plot for the first two FRH layers and fit function (Monte Carlo simulations).

In the second step, the calibration parameters are varied to find a set, where the calibrated real data are described best by the corresponding function f_{MC} . The fitting software provides a graphical user interface (Fig. 2) which gives a comfortable opportunity to find appropriate start parameters. The data are recalibrated in real time and plotted in a second frame (not shown here). For each layer combination the quality of the matching is quantified by the same χ^2_{red} algorithm as used before (equation 2) in order to compensate potential systematic effects. An averaged χ^2_{red} value is calculated which allows for a simultaneous optimization of the calibration parameters of each detector layer by a fitting routine.

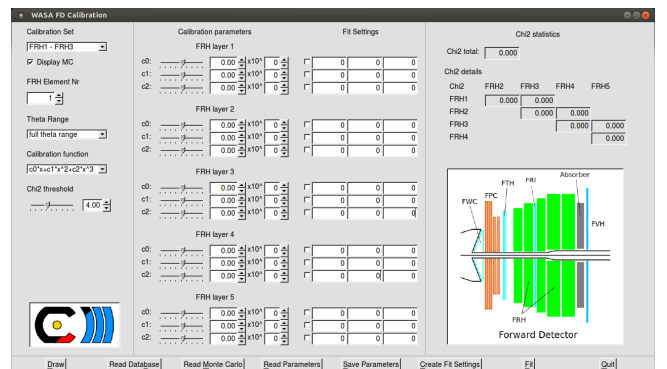


Figure 2: Interface for the new calibration software.

This software package allows for a very fast and accurate calibration of the main energy detector of the forward system which is a keystone for the analysis of rare and forbidden eta decays.

*Supported by COSY-FFE

[†]Institut für Kernphysik, Westfälische Wilhelms-Universität, 48149 Münster, Germany

Study of the $\eta \rightarrow \pi^+ \pi^- \pi^0$ decay in $p - p$ collisions with WASA-at-COSY

W. Bardan* for the WASA collaboration

Study of the $\eta \rightarrow \pi^+ \pi^- \pi^0$ decay allows for precise tests of C parity conservation [1, 2, 3], makes possible to set constraints on the u and d as well as s and d quark mass ratios and can be used for a verification of the predictions of the Chiral Perturbation Theory (ChPT) [4]. The $\eta \rightarrow \pi^+ \pi^- \pi^0$ decay was measured with high statistics by the KLOE collaboration which built the Dalitz plot containing about $1.3 \cdot 10^6$ events [1]. Results of the KLOE experiment show a deviation from ChPT predictions and no evidence for the C parity violation. The WASA-at-COSY collaboration conducted analogical studies with η -mesons produced in pd and pp collisions in experimental runs in 2008. This report presents preliminary results of the ongoing analysis of the pp data collected with the WASA-at-COSY during 8 weeks of the COSY beam time in 2010 with approximately $2 \cdot 10^8$ η mesons produced. During the experiment the momentum of the proton beam was fixed to $2.142 \text{ GeV}/c$ which corresponds to an excess energy $Q=55 \text{ MeV}$ with respect to the threshold of the η meson production. The two outgoing protons from the $pp \rightarrow pp\eta$ reaction were registered in the Forward Detector of the WASA-at-COSY facility. The three pions originating from the $\eta \rightarrow \pi^+ \pi^- \pi^0$ decay were measured in the Central Detector. Only events with two positive tracks in the Forward Detector, at least two charged and at least two neutral tracks in the Central Detector were selected for the further analysis. Next, proper conditions for time differences between registered tracks and for energy deposits of particles were applied. The protons in the Forward Detector were identified by the $\Delta E - E$ method with a cut applied on the energy loss in the first layer of the Forward Range Hodoscope (FRH) vs. energy deposit in all layers of the FRH (see Fig. 1).

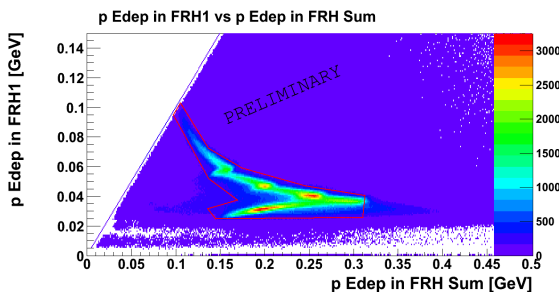


Fig. 1: Energy loss in the first layer of FRH vs. total energy deposited in all layers of FRH.

The charged pions were identified using the $\Delta E - p$ method, where the energy loss ΔE was measured in the Plastic Scintillator Barrel and the momentum p was determined based on a curvature of track in the magnetic field of the solenoid registered with the Mini Drift Chamber (see Fig. 2). In the further analysis only events with exactly one π^+ and one π^- were taken into account. For the π^0 identification, only gamma pairs with opening angle in the center of mass of the beam and target protons larger than 60° were selected and a cut was applied on the invariant mass spectrum as shown in Fig. 3.

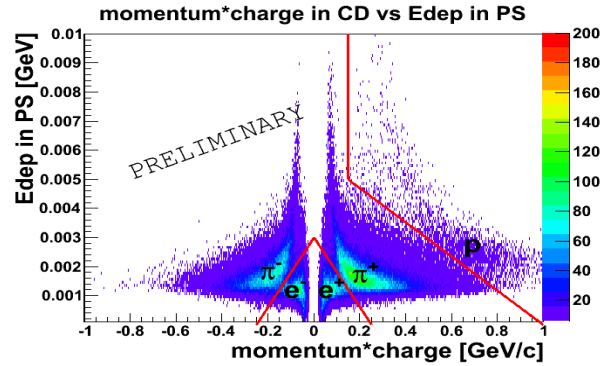


Fig. 2: Energy loss ΔE in the Plastic Scintillator Barrel vs. momentum p multiplied by charge.

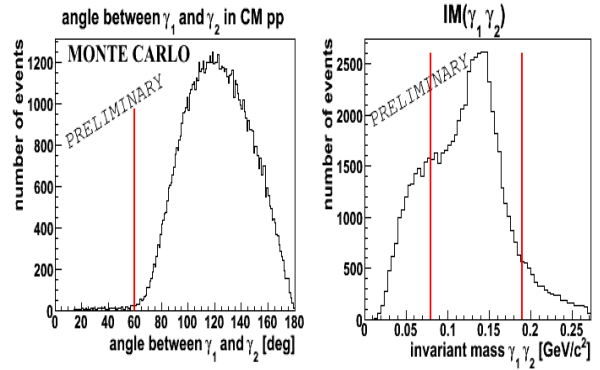


Fig. 3: Left: Opening angle between gamma pairs in the center of mass of the beam and target protons from $\eta \rightarrow \pi^+ \pi^- \pi^0$ decay simulations. Right: Invariant mass of two gammas from experimental data with indicated cut for π^0 identification.

For a further background reduction, a 4-constraint kinematic fit (KF) was implemented. In the fit procedure kinematic parameters of two outgoing protons, π^+ , π^- and two gammas were adjusted. For the error parametrisation in the KF, single particles simulations including protons, π^+ , π^- and gammas were performed with kinetic energies and polar angles generated uniformly in proper ranges. For each particle type differences between the reconstructed and generated values of kinetic energies, polar angles and azimuthal angles were plotted as a function of the kinetic energy and polar angle. Example of error parametrisation for kinetic energy of protons is presented in the left panel of Fig. 4.

Probability distribution of χ^2 resulting from the kinematic fit procedure applied to experimental data is shown in the right panel of Fig. 4. For the further analysis only events with probability larger than 0.1 were taken.

After the kinematic fit and a cut on the probability distribution of χ^2 , a background visible in the $pp\pi^+\pi^-$ missing mass squared spectrum in the vicinity of $mm^2 = 0$, originating from the $pp \rightarrow pp\pi^+\pi^-$ reaction, completely disappears (see Fig. 5).

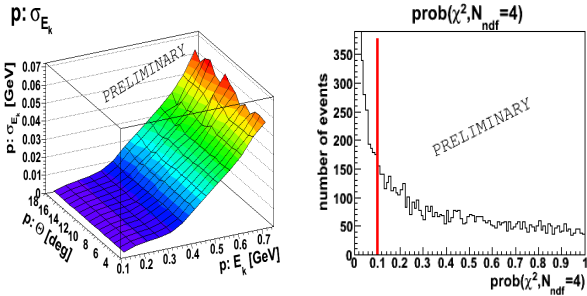


Fig. 4: Left: Errors of kinetic energy of protons as a function of kinetic energy and polar angle. Right: Probability distribution of χ^2 resulting from kinematic fit procedure for 4 degrees of freedom with indicated cut applied on this value.

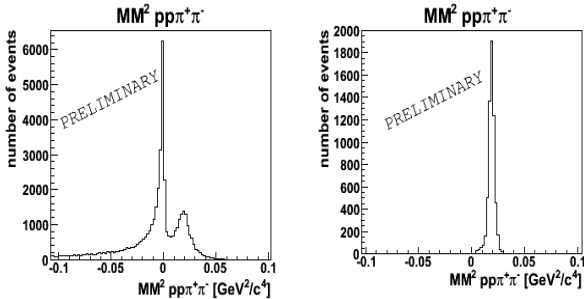


Fig. 5: Missing mass squared of the $pp\pi^+\pi^-$ system before kinematical fit (left) and after kinematical fit and cut on the probability of χ^2 distribution (right).

The kinematic fit reduces also significantly the background under the eta peak in the missing mass of two protons (see Fig. 6).

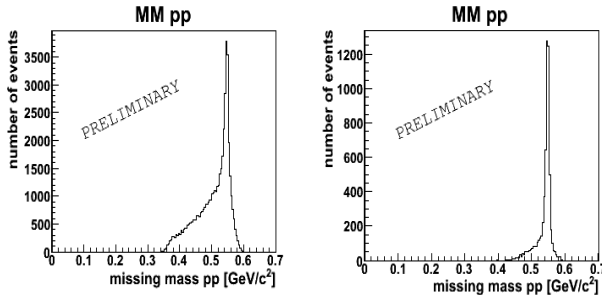


Fig. 6: Missing mass of pp before kinematic fit (left) and after the fit and cut on the probability of χ^2 (right).

Currently, a procedure for background subtraction under the η -peak in the pp missing mass spectra for each bin of the $\pi^+\pi^-\pi^0$ Dalitz plot is being implemented in the data analysis software.

References:

- [1] KLOE Collaboration, F. Ambrosino *et al.*, *Determination of $\eta \rightarrow \pi^+\pi^-\pi^0$ Dalitz plot slopes and asymmetries with the KLOE detector*, JHEP 05 006 (2008), arXiv:0801.2642.
- [2] J. G. Layter *et al.*, *Measurement of the charge asymmetry in the decay $\eta \rightarrow \pi^+\pi^-\pi^0$* , Phys. Rev. Lett. 29 (1972) 316.

- [3] M. R. Jane *et al.*, *A measurement of the charge asymmetry in the decay $\eta \rightarrow \pi^+\pi^-\pi^0$* , Phys. Lett. B 48 (1974) 265.
- [4] J. Bijnens and J. Gasser, *η decays and beyond p^4 in chiral perturbation theory*, Phys. Scripta T99 (2002) 34.

* M. Smoluchowski Institute of Physics, Jagiellonian University, Reymonta 4, 30-059 Cracow, Poland, e-mail: wiktobardan@uj.edu.pl

Analysis of the decay $\eta \rightarrow \pi^+\pi^-\gamma$ with WASA-at-COSY

D. Lersch

The decay $\eta \rightarrow \pi^+\pi^-\gamma$ is suitable to study the chiral anomalies of QCD. While it is solely determined by the box anomaly in the chiral limit [1], at physical meson masses, the triangle anomaly dominates the box anomaly because of the final state interactions between the two pions [2], [3]. Thus, a correct description of this decay can only be achieved by including final state interactions. The experimental observables to test interaction models are:

- i) The relative branching ratio: $\frac{\Gamma(\eta \rightarrow \pi^+\pi^-\gamma)}{\Gamma(\eta \rightarrow \pi^+\pi^-\pi^0)}$
- ii) The photon energy E_γ distribution

In order to measure both quantities in one experiment, the reaction $pp \rightarrow pp[\eta \rightarrow \pi^+\pi^-\gamma]$ has been investigated. The data have been acquired during spring 2010 using the WASA-at-COSY facility [4].

The recent analysis focusses on reconstructing $\eta \rightarrow \pi^+\pi^-\gamma$ events, but also investigates the channel $\eta \rightarrow \pi^+\pi^-\pi^0$. This channel is important for determining the relative branching ratio.

In the following, the basic tools of both analyses (such as particle identification in the forward detector and a least squares kinematic fit) will be discussed briefly.

Figure 1 shows an example for particle identification in the

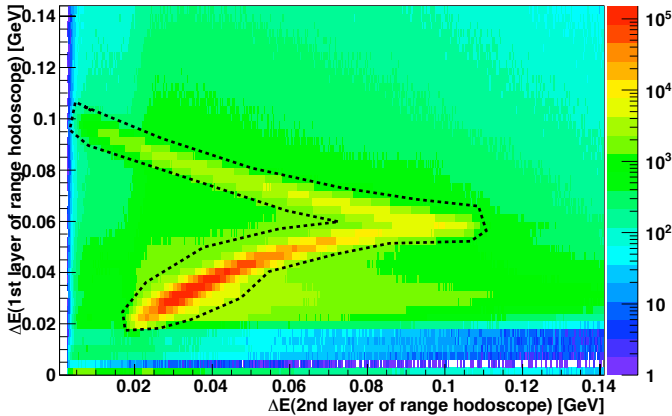


Fig. 1: Deposited energy in layer 1 vs layer 2 of the forward range hodoscope. The black line indicates the graphical selection for proton candidates.

forward detector of WASA. This method is applied to all layer combinations of the forward range hodoscope, which is an essential part of the forward detector.

In order to reduce background related to direct pion production (e.g. $pp \rightarrow pp\pi^+\pi^-\pi^0$) and to select $\eta \rightarrow \pi^+\pi^-\gamma$ events, a least squares kinematic fit with constraint on energy and momentum conservation has been used. Events with a fit probability larger than 30% are accepted (see Fig. 2), because for this value the highest significance is observed. Pions might cause showers in the calorimeter, which are reconstructed as a charged particle and an additional photon. Those wrongly reconstructed photons are located close to the impact point of the charged track in the calorimeter and have small energies. Thus, events with small photon energies and small opening angles between charged and neutral particles are rejected.

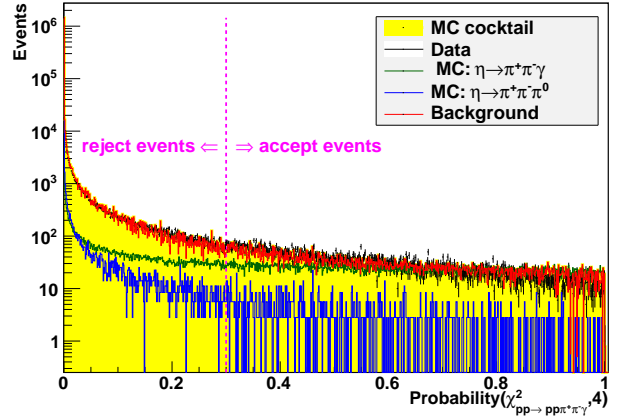


Fig. 2: Probability distribution from a kinematic fit related to reaction hypothesis: $pp \rightarrow pp\pi^+\pi^-\gamma$. The probability distribution obtained from data (black points) is nicely described by MC simulations (yellow area), where the reaction of interest $\eta \rightarrow \pi^+\pi^-\gamma$ (green curve), the reference channel $\eta \rightarrow \pi^+\pi^-\pi^0$ (blue curve) as well as background reactions $pp \rightarrow pp\pi^+\pi^-\pi^0$ (red curve) have been put into a MC cocktail. The purple line indicates the cut to select/reject $\eta \rightarrow \pi^+\pi^-\gamma$ event-candidates.

$\eta \rightarrow \pi^+\pi^-\pi^0$ -events are selected by using a kinematic fit with the same constraints as mentioned above plus the additional constraint: $\pi^0 \rightarrow \gamma\gamma$.

50% of the 2010 data set has been analysed with this analysis chain and the preliminary results for both analyses are shown in Figure 3. In both cases the background has been determined by using a 4th order polynomial folded with a MC simulated phase space distribution of $pp \rightarrow pp\pi^+\pi^-\pi^0$.

In a next step, the relative branching ratio will be calculated (this requires the reconstruction efficiencies for both channels). The photon energy distribution E_γ of $\eta \rightarrow \pi^+\pi^-\gamma$ will be determined as well. For that purpose the missing mass deduced from two protons, after event selection, is plotted as function of E_γ in the η rest-frame (see top of Fig. 4). The photon energy distribution will be binned and the corresponding missing mass distribution (see bottom of Fig. 4) will be background subtracted and corrected for efficiency. This will then lead to the final photon energy distribution. Finally, the systematic effects (e.g. a different cut on the kinematic fit probability) on both observables will be investigated.

References:

- [1] Wess, Zumino, *Phys. Lett.*, **B37**, 95, (1971), Witten, *Nucl. Phys.*, **B223**, 422, (1983)
- [2] B. R. Holstein, "Allowed eta decay modes and chiral symmetry", *Phys. Scripta*, **T99**, 55 (2002)
- [3] F. Stollenwerk, et al. "Model independent approach to $\eta \rightarrow \pi^+\pi^-\gamma$ and $\eta' \rightarrow \pi^+\pi^-\gamma$ ", *Phys. Lett.*, **B707**, 184 (2012)
- [4] H.-H Adam et al., Proposal for the wide angle shower apparatus WASA-at-COSY, (2004)

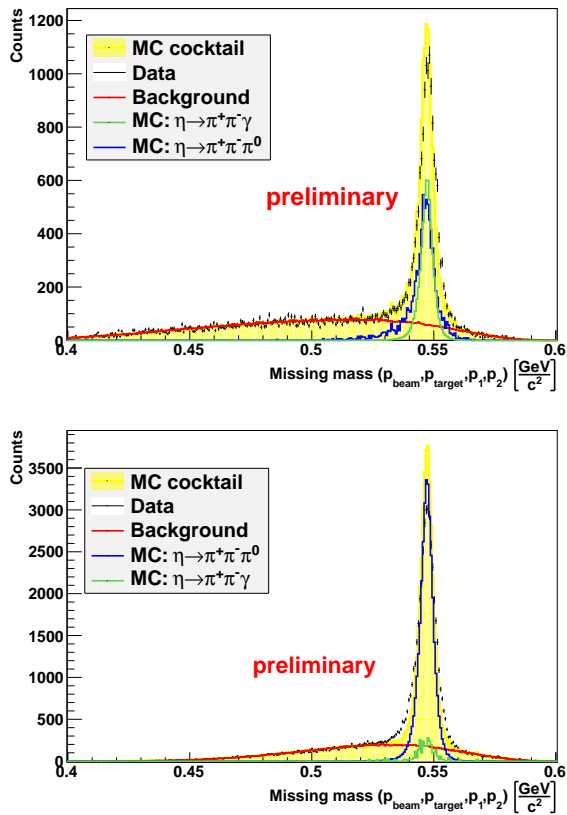


Fig. 3: Missing mass deduced from two protons, reconstructed in the forward part of WASA. Top: Analysis $\eta \rightarrow \pi^+\pi^-\gamma$. Bottom: Analysis of $\eta \rightarrow \pi^+\pi^-\pi^0$

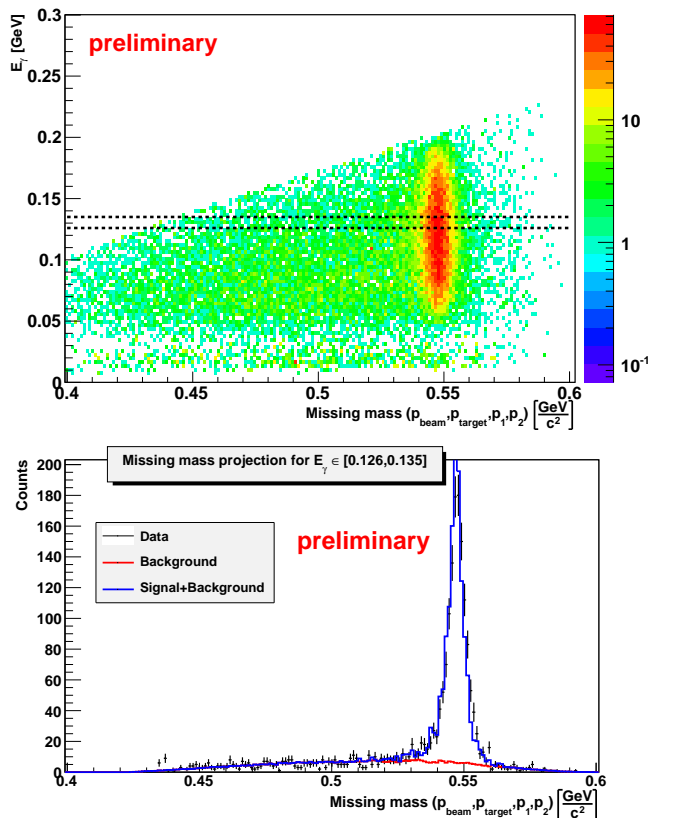


Fig. 4: Top: E_γ distribution in the rest frame of the η -meson as function of the two proton missing mass distributions of two protons after selecting $\eta \rightarrow \pi^+\pi^-\gamma$ -events. The black lines indicate as an example the range of E_γ (0.126GeV - 0.135GeV) that has been selected to investigate the missing mass distribution presented in the lower frame. The data (black points) are described by MC simulations (blue curve), using: $\eta \rightarrow \pi^+\pi^-\gamma$ and $\eta \rightarrow \pi^+\pi^-\pi^0$ for the signal region and $pp \rightarrow pp\pi^+\pi^-\pi^0$ folded with a 4th order polynomial (red curve).

The electromagnetic transition form factor of the $\omega\pi$ transition as determined from the decay $\omega \rightarrow 1^+ 1^- \pi^0$ does not agree with standard vector meson dominance predictions[1, 2, 3]. When theoretical efforts attempt to go beyond vector meson dominance in a systematic way using ChPT [4] and dispersion theory [5] the form factor seems to agree with the data except at large q^2 . Earlier experiments provide results on the electromagnetic transition form factor for the $\omega\pi^0$ vertex in $\omega \rightarrow \mu^+ \mu^- \pi^0$ as found in the review by L.G.Landsberg [1]. Recently, the NA60 collaboration has confirmed the results in AA as well as pA collisions [2, 3]. There is a need of more experimental data from other experimental approaches, especially at higher q^2 . Our goal is to acquire data with an alternative experimental approach using pd and pp collisions with WASA-at-COSY. Here, we detect e^+e^- pairs giving access to the full range of virtual photon mass. Also, we reconstruct the two photons from the π^0 thus including the exclusive reconstruction of the decaying meson.

Two sets of experiments have been performed with WASA at COSY using different reaction mechanisms. The idea is to compare the quality of the data between pd and pp reactions, in the sense of a feasibility and background study for $\omega \rightarrow e^+e^-\pi^0$ decays. For $pd \rightarrow {}^3\text{He}\omega$, two different beam energies $T_p = 1.5$ GeV and 1.45 GeV were used. A pilot experiment for the $pp \rightarrow pp\omega$ reaction has been performed at $T_p = 2.063$ GeV. Although the pp reaction has a bigger cross section, it has significantly more background than pd which makes the on-line and off-line event selection more challenging.

For the pd reaction, particles emitted in the forward direction i.e. ${}^3\text{He}$ are identified using the ΔE - E method in the forward hodoscopes which cover the polar angular range 3° - 18° . The decay particles e^+ , e^- and γ are identified in the central part of the detector, described in more detail in [6].

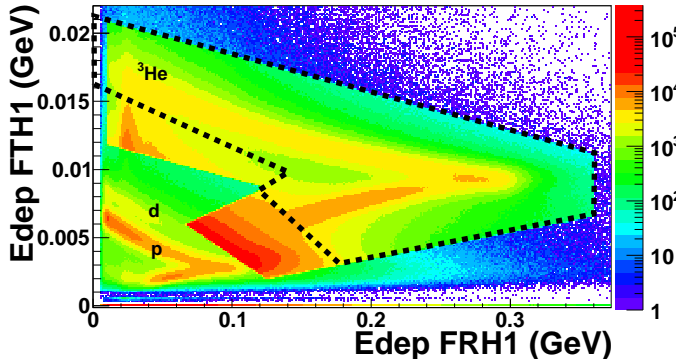


Fig. 1: Particle identification plot for ${}^3\text{He}$. Energy deposited in forward range hodoscope (FRH1) as a function of energy deposited in forward trigger hodoscope (FTH1).

$\omega \rightarrow \gamma\pi^0$ final state: The analysis has been started with the real photon case $\omega \rightarrow \gamma\pi^0 \rightarrow \gamma\gamma$, as a reference channel. ω mesons are tagged via the missing mass deduced from the ${}^3\text{He}$, detected in forward direction as shown in Fig. 1. A ${}^3\text{He}$ based data preselection leads to the appearance of sharp edges in this figure. A clear band of ${}^3\text{He}$ is seen with protons

and deuterons originating from hadron-nucleon interactions and breakup reactions. The events within the black dotted curve are the selected ${}^3\text{He}$ tracks for the further analysis.

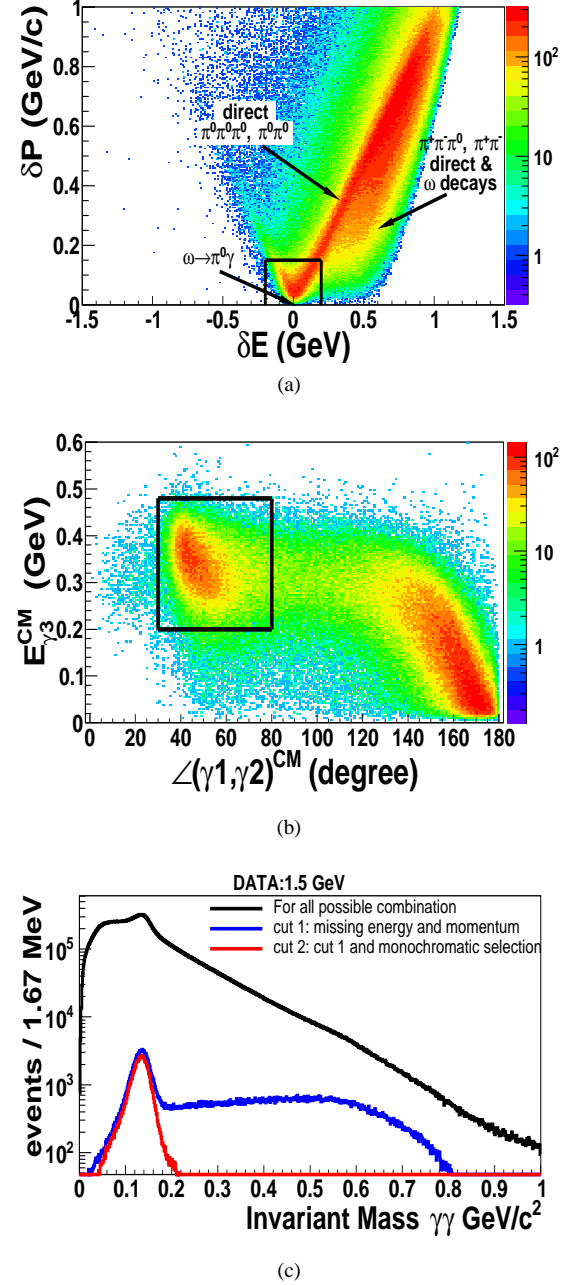
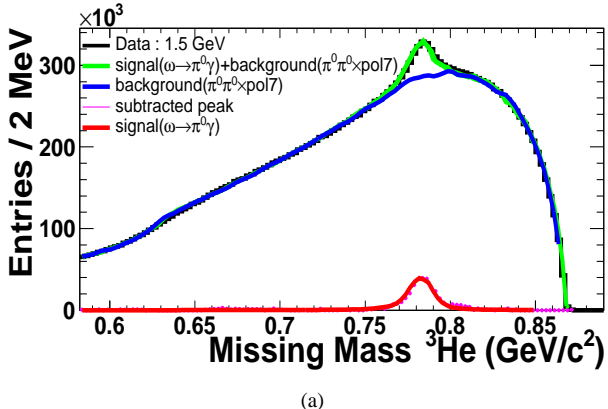
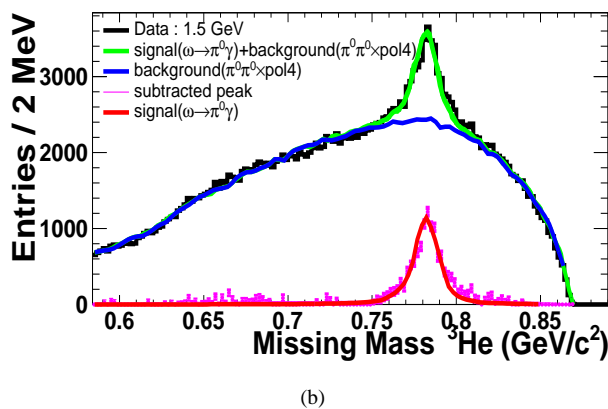


Fig. 2: (a) Plot of the overall missing energy (δE) vs overall missing momentum (δP) of the ${}^3\text{He}$ and ${}^3\gamma$ system. (b) Monochromatic γ plot, shows energy distribution of the third γ in the ω -rest frame $E_{\gamma^3}^{\text{CM}}$ as a function of the angle between the first and second γ in the ω -rest frame $\angle(\gamma_1, \gamma_2)^{\text{CM}}$ for all possible combinations. (c) The black line is the 2γ invariant mass distribution for all combinations. The blue curve is the 2γ invariant mass distribution, after the overall kinematic check for all possible combinations. The red curve is the 2γ invariant mass distribution from π^0 decay, after the monochromatic γ cut.

The $\pi^0\gamma$ final state is fully reconstructed with one ${}^3\text{He}$ track in forward hodoscopes and three neutral tracks in the electromagnetic calorimeter. The overall kinematic check for ${}^3\text{He}$ and 3γ system has been done, as illustrated in Fig. 2a. The events near (0,0) should ideally come from the $\pi^0\gamma$ final state, but due to the detector resolution a dense parabolic feature with the vertex position at (0,0) is seen, along with a huge background from direct pions on the right hand side. The combinations within the black graphical cut have been selected as 3γ from $\pi^0\gamma$. The next check was done using the properties of monochromatic γ and π^0 . Since the $\omega \rightarrow \pi^0\gamma$ is a 2-body decay, the bachelor γ will be monochromatic with $E_{\gamma^3}^{CM} = 0.38 \text{ GeV}$, in the ω rest frame. The angle between the two γ s from π^0 decay will have a range from 40° to 180° , with a dominance around 40° - 80° in the ω rest frame, is seen as the left prominent region in the Fig. 2b. While the angle between the monochromatic γ and the two γ s from π^0 decay will be populated towards 180° , the well pronounced structure on the right hand side of the Fig. 2b. A black rectangular window is used, as shown in Fig. 2b. In order to make sure that the selected 3γ s are the correct $\pi^0\gamma$ combination and to distinguish between the γ from π^0 decay and the bachelor γ . The invariant mass distribution of 2 neutral tracks in the electromagnetic calorimeter is shown in Fig. 2c, after different conditions. In all 3 distributions a peak can be seen at the π^0 mass $0.135 \text{ GeV}/c^2$. The number of combinations is reduced after each consecutive condition. A clean π^0 distribution is seen, as indicated by the red curve.



(a)



(b)

Fig. 3: (a) The inclusive missing mass spectrum of ${}^3\text{He}$. (b) The exclusive missing mass spectrum of ${}^3\text{He}$.

A one-dimensional spectrum of the ${}^3\text{He}$ missing mass (MM) is shown in Fig. 3a after the ${}^3\text{He}$ selection. The MM is calcu-

lated using, $\text{MM}_{{}^3\text{He}} = \sqrt{(E_p + m_d - E_{{}^3\text{He}})^2 - (\vec{P}_p - \vec{P}_{{}^3\text{He}})^2}$, where E , m and \vec{P} are the energy, mass and momentum of the particles, respectively. The black curve is data taken with a beam energy of 1.5 GeV. An enhancement at the ω meson mass $0.782 \text{ GeV}/c^2$ is seen on a smooth continuous background of direct pion production. The green curve is the combined fit of Monte Carlo for $\omega \rightarrow \pi^0\gamma$ and the most prominent direct $\pi^0\pi^0$ production folded with a polynomial. The blue curve is only the background from the combined fit. The background subtracted data has been plotted as magenta points, described by $\omega \rightarrow \pi^0\gamma$ Monte Carlo simulation, with a peak near the ω mass $0.782 \text{ GeV}/c^2$.

In the same way, a one-dimensional spectrum of the ${}^3\text{He}$ missing mass is shown in Fig. 3b after ${}^3\text{He}$ and $\pi^0\gamma$ selection. The signal to background ratio for inclusive MM spectrum is 0.05, which clearly improves to 0.17 for the exclusive spectrum. The peak position $0.782 \text{ GeV}/c^2$ and the resolution $17 \text{ MeV}/c^2$ of the background subtracted peak is in fair agreement with the simulation. The missing mass distributions have been used to estimate the number of ω mesons produced.

The number of ω mesons produced N_ω and average luminosity L_A is estimated by using:

- $N_\omega = N/(\varepsilon)$ and $L_A = N_\omega/(\sigma \times T_R)$, for inclusive MM,
- $N_\omega = N/(\varepsilon \times \text{BR}_{\omega \rightarrow \pi^0\gamma})$ and $L_A = N_\omega/(\sigma \times T_R)$, for exclusive MM.

Where, N is the number of ω mesons in the background subtracted peak, ε is the efficiency of the selection criteria, the branching ratio $\text{BR}_{\omega \rightarrow \pi^0\gamma}$ is $(8.28 \pm 0.28)\%$ [7], T_R is the total run time $(1.0523 \times 10^6 \text{ s})$ and the cross section σ is $(83.6 \pm 1.5) \text{ nb}$ [8]. The number of ω mesons produced during the $pd \rightarrow {}^3\text{He}\omega$ beam-time is about $N_\omega = 1 \times 10^6$ and the average luminosity is estimated to be about $L_A = 1 \times 10^{31} \text{ cm}^{-2} \text{ s}^{-1}$.

Based on the Monte Carlo studies, 10 events are expected for the $\omega \rightarrow e^+e^-\pi^0$ decay in the pd data, which makes the form factor determination unfeasible. The analysis for the $\omega \rightarrow e^+e^-\pi^0$ decay will be developed to find these event candidates and hence to verify its branching fraction. An analysis for the pp data is also going on, as a feasibility study.

As a next step for this analysis, the branching ratio of the $\omega \rightarrow \pi^0\gamma$ decay will be determined relative to the $\omega \rightarrow \pi^+\pi^-\pi^0$ decay. The branching ratio will also be studied as a function of luminosity.

References:

- [1] L. G. Landsberg, Phys. Rept. **128**, (1985), 301.
- [2] An. Uras *et al.*, J. Phys. Conf. Ser. **270**, (2011), 012038.
- [3] R. Arnaldi *et al.*, Phys. Lett. B **677**, (2009), 260.
- [4] C. Terschluesen, *et al.*, Phys. Lett. B **691**, (2010), 191.
- [5] Sebastian P. Schneider, Phys. Rev. D **86**, (2012), 054013.
- [6] H.-H Adam *et al.*, Proposal for the wide angle shower apparatus (WASA) at COSY-Juelich, (2004).
- [7] K. Nakamura *et al.*, Particle Data Group, JPG **37**, (2010), 075021.
- [8] K. Schonning *et al.*, Phys. Rev. C **79**, (2009), 044002.

The PANDA experiment is one of the major projects of the FAIR facility in Darmstadt and will study the interactions between anti-protons and fixed target protons and nuclei in the momentum range of 1.5-15 GeV/c using the High Energy Storage Ring (HESR). Many measurements of physics topics are foreseen. The semileptonic D_s decays are governed by both the weak and strong forces, where the strong interaction effects can be parameterized by the transition form factor. Techniques such as lattice QCD offer increasingly precise calculations [1], but as the uncertainties shrink, experimental validation of the results becomes increasingly important. The achievable performance of the PANDA detector for these types of reactions has not yet been studied in detail; however, this is expected to work very well based upon the design performance and experience with other detector systems due to the kinematic overconstraints which allow these events to be completely reconstructed despite one particle not being measured. This report summarizes the simulation and reconstruction status of the D_s decay chain at PANDA.

Decay Model Antiproton annihilation on a proton target will be used to generate D_s pairs. One of the D_s mesons can be a "trigger", and be reconstructed via a decay branch that is relatively common and has a simple final state, e.g. the hadronic mode $D_s \rightarrow KK\pi$. For a reasonable simulation, we import a new decay model DS_DALITZ in the software PandaRoot. It includes the contributions of six resonances and the corresponding parameters in the amplitude are fitted to the BaBar experiment [2]. The original code is partly from the EvtGen package developed jointly for the BaBar and CLEO Collaboration, where the $D_s \rightarrow KK\pi$ decay is implemented as a branch of the existing D_DALITZ model. We tested its performance in the framework of PandaRoot via the Dalitz analysis (see Figure 1). This output agrees with the previous measurements [2, 3, 4] as expected. In the semileptonic channel, we adopt the ISGW2 model to simulate the decay of the D_s and the ETA_DALITZ model for the $\eta \rightarrow \pi^+\pi^-\pi^0$ decay.

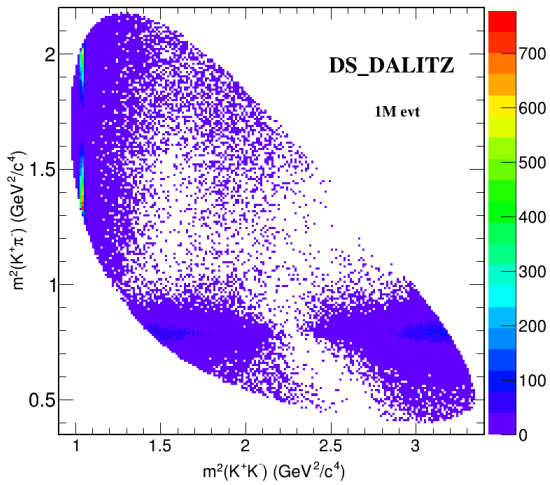


Fig. 1: Dalitz plot of $D_s^- \rightarrow K^+K^-\pi^-$ in MC simulation with DS_DALITZ decay model.

Reconstruction In this procedure, we focus on developing the software and evaluating the expected precision of these measurements using Monte Carlo simulation of the PANDA detector. We have reconstructed the hadronic channel $D_s^- \rightarrow K^+K^-\pi^-$ with 100,000 events. We perform the vertex fitting and mass constraint fitting for all candidates, where the cut on the probability distribution from the χ^2 values is $prob > 0.01$. The reconstruction strategy is slightly tricky for this semileptonic decay chain: $D_s^+ \rightarrow \nu_e e^+ \eta$, $\eta \rightarrow \pi^+\pi^-\pi^0$ and then $\pi^0 \rightarrow \gamma\gamma$. We started from the combination of two photons detected by the Electromagnetic Calorimeter (EMC). The minimal laboratory angle between two photons should be larger than the EMC spatial resolution σ_θ . The mass constraint fitting has been performed on the two-photon system to select the "best" fitted π^0 for reconstructing the mother particle η . The charged tracks of π^+ and π^- determine the vertex reconstruction of $\eta \rightarrow \pi^+\pi^-\pi^0$, and in this step the performance of the kinematic fitter plays an essential role on the total efficiency of the reconstructed η , since the neutral daughter π^0 has achieved a high efficiency with a mass resolution of $3.2 \text{ MeV}/c^2$. The preliminary results of reconstruction efficiency ϵ and resolutions σ of the D_s and η are listed in Table 1.

Table 1: Reconstruction results of D_s^- and η .

	ϵ [%]	σ_{mass} [MeV/c^2]	$\sigma_{vtx} [\mu\text{m}]$			$\sigma_{mom} [\%]$	
			x	y	z	p_t	p_z
D_s^-	18	17	66	73	155	2.8	1.3
η	26	9	318	287	675	3.8	4.3

Summary The efficiency of the $e^+\nu_e$ system should be the product of the efficiencies of D_s^- and η , which is 4.7% in the present result. The cross section of D_s pair at PANDA is roughly estimated to be 10 nb [5]. With the luminosity of $10^{32} \text{ cm}^{-2}\text{s}^{-1}$ and the average branching ratios, the production rate is estimated to be approximately 200 events per month. This result is not the final estimation, since the present software is under development and will be significantly improved in the near future. The upcoming steps will include detailed investigations of the reconstruction efficiency and resolution and incorporating the kinematic fit procedures to extract information on the unmeasured neutrino in the final state.

References:

- [1] I. Kanamori, arXiv:1302.6087 [hep-lat].
- [2] P. del Amo Sanchez *et al.* (BABAR Collaboration), Phys. Rev. D **85**(5), 052001 (2011).
- [3] P. Frabetti *et al.* (E687 Collaboration), Phys. Lett. B **351**, 591-600 (1995).
- [4] R. E. Mitchell *et al.* (CLEO Collaboration), Phys. Rev. D **79**(7), 072008 (2009).
- [5] J. Haidenbauer, Priv. Comm., (2012).

The proposed Day-One experiment at HESR is to measure antiproton-proton elastic scattering in a large range of 4-momentum transfer squared t (0.0008 - 0.1 GeV^2). One goal of the Day-One experiment is to determine the elastic differential parameters (σ_T , ρ and b). The elastic scattered antiproton and recoil proton will be measured by tracking detectors in the forward angle region and by energy detectors near $\theta=90^\circ$, respectively.

The recoil detectors consist of two silicon detectors and two germanium detectors which cover a polar angle from 71° to 91.5° . All detectors are single-sided structure with 1.2 mm pitch on the front side. The main parameters of the silicon and the germanium detectors are shown in Table 1. The silicon detectors will stop recoil protons with energy up to 12 MeV and the germanium detectors will measure recoil protons with energy from 12 MeV to 60 MeV.

Table 1: Main parameters of the Si and Ge detectors.

Name	Length (mm)	Width (mm)	Thickness (mm)	Strip No.	Pitch (mm)
Si _{#1}	76.8	50.0	1.0	64	1.2
Si _{#2}					
Ge _{#1}	80.4	50.0	5.0	67	1.2
Ge _{#2}			11.0		

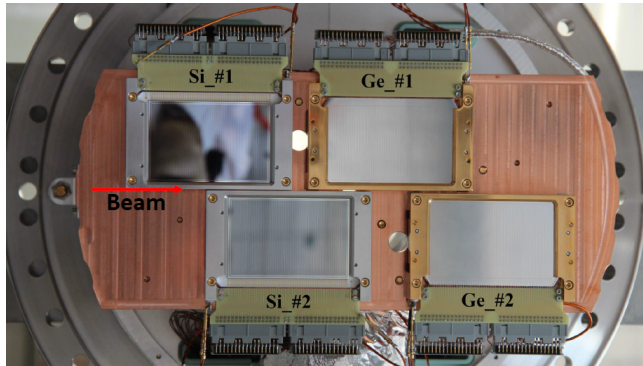


Fig. 1: Layout of detectors for pp elastic scattering experiments.

After assembling and system tests in the laboratory, the detector system has been installed in COSY. The detector layout is shown in Fig. 1. Two commissioning experiments have been performed in 2013. Data of proton-proton elastic scattering has been taken at several beam momenta. The energy spectra of all strips on Si_{#2} and Ge_{#2} at $P_{beam} = 3.2 \text{ GeV}/c$ are shown in Fig. 2 (a, c) after calibration. The candidate elastic events on Si_{#2} clearly form a band. The events on Ge_{#2} have been mixed with background. The main reason is that two or more strips fire when one recoil proton hits on the detector. Therefore, it is necessary to do clustering at the beginning of data analysis. The cluster signal is defined as the sum of the neighbour strip signals which belong to the cluster. The energy

spectra of Si_{#2} and Ge_{#2} have been improved a lot after cluster construction as shown in Fig. 2 (b, d).

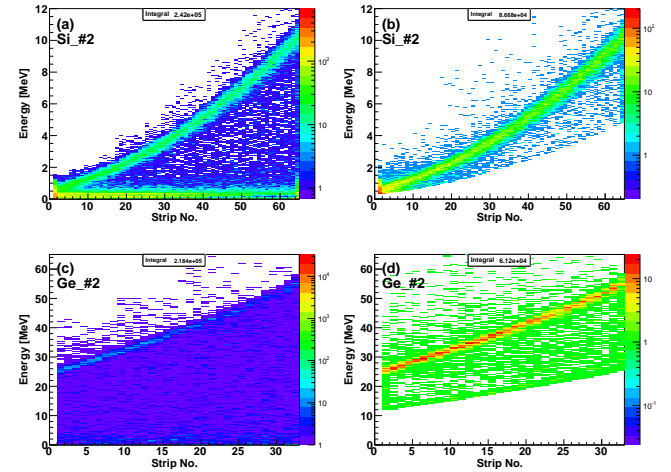


Fig. 2: Energy spectra of Si_{#2} and Ge_{#2} without clustering (a, c) and after cluster construction (b, d).

The hit multiplicity of each event is shown in Fig. 3. It can clearly be seen that Si_{#1} takes up the most percentage at multiplicity=1 and Ge_{#2} takes up the least. The main reason is that Si_{#1} covers larger polar angle (83.2° - 88.5°) than that of Ge_{#2} (76.5° - 80.5°) since the recoil proton's energy becomes larger with the decreasing of the polar angle. Therefore, Si_{#1} takes up smaller percentage than that of Ge_{#2} while multiplicity ≥ 2 .

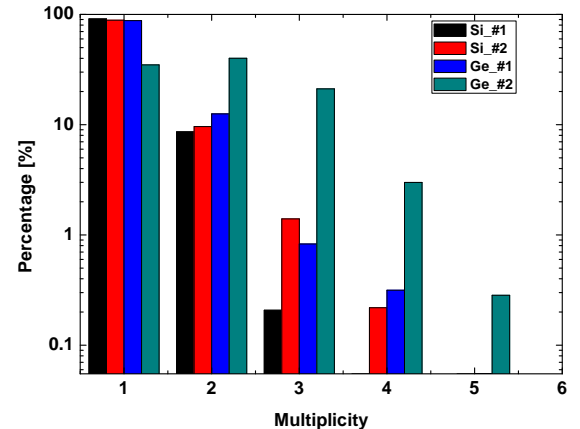


Fig. 3: Multiplicity distribution of events on Si and Ge detectors.

In summary, the clustering algorithm is needed for the complete energy reconstruction and further analysis is needed to determine the t -spectrum.

¹Institute of Modern Physics, CAS, 730000 Lanzhou, China

²Forschungszentrum Juelich, 52425, Germany

The $\bar{\text{P}}\text{ANDA}$ ¹ experiment is one of the main experiments at the upcoming FAIR² facility currently under construction in Darmstadt. In the energy region investigated by $\bar{\text{P}}\text{ANDA}$, background and signal events have similar signatures. Because of this, a hardware-level triggering mechanism is not foreseen for the experiment. Instead, a fast online event filter will substitute this element. The planned event rate for $\bar{\text{P}}\text{ANDA}$ is $2 \cdot 10^7$ /s, leading to a data rate of approximately 200 GB/s. For further in-depth offline analysis, the online event reconstruction has to reduce this data rate by three orders of magnitude. An important part of the online event reconstruction is particle tracking: From discrete hit points continuous tracks are computed. With this, the nature of the recorded particle can be deduced, giving basis for a subsequent, more complex decision to keep or disregard the event. We investigate the feasibility of using GPUs³ for online tracking at $\bar{\text{P}}\text{ANDA}$ and this report introduces the basic principles of the algorithms considered for GPU online tracking and summarizes the status of the study.

Tracking Algorithms Currently, three different algorithms are under investigation for GPU online tracking purposes: Hough Transform, Riemann Track Finder, Triplet Finder. The algorithms all have different properties and specialize in distinct features. All three first perform a circle fit in the two-dimensional (x, y) plane, extending it in a second step to a three-dimensional helix afterwards. The algorithms are in varying stages of development with their feature sets being investigated independently.

The development and studies are done in close cooperation with the NVIDIA Application Lab of the Jülich Supercomputing Centre.

Hough Transform An easily parallelizable method to find straight lines connecting points is the Hough Transform (HT). In order for the HT to work, a conformal mapping pre-step, transforming curved tracks to straight lines, is needed. Using the transformed hit points (x_i, y_i) , the equation $\rho = x_i \cos(\alpha) + y_i \sin(\alpha)$ is solved, with α selected at many different values between 0° and 180° , with arbitrary granularity. When histogrammed, the (α, ρ) bin with the highest multiplicity gives the most probable track parameter. See [1, 2] as well as last year's version of this report for a detailed explanation [5].

For the HT, two different GPU implementations as well as a CPU testing code exist. The first GPU version is written in Thrust [3], a template library on top of NVIDIA's CUDA C/C++ GPU programming language [4]. While creating easily readable code running very fast, the Thrust HT version has only limited customizability. The second GPU version uses plain CUDA code including Dynamic Parallelism. This technique allows the process running on the GPU to initialize independent GPU processes, leading to a very fast and flexible code. In first studies with this code it is shown that the track of a single track event can be reconstructed in 0.5 ms.

Current investigations include the development of a fast multipipeak finding algorithm being able to find an arbitrary number of peaks in a two-dimensional histogram. This is needed for a following qualitative evaluation of the different HT algorithms as well as the HT in general.

Riemann Track Finder This method maps two-dimensional hit points onto a Riemann surface (paraboloid), creates a plane passing the mapped three-dimensional points, and from that deduces the parameters of the line (*track*) connecting the original points [7]. The benefit of this method is the transformation of a circle fitting-problem to a plane calculation – a very fast technique, when the combinatorics of the seeding track points can be kept small.

The Riemann Track Finder is included in $\bar{\text{P}}\text{ANDA}$'s computing framework PandaRoot and regularly and intensively used in track reconstruction. This summer, a first GPU implementation of this algorithm was done using CUDA. While having the same algorithmic structure, some GPU-specific modification had to be made, for example in the generation of the initial starting hits.

The GPU implementation is in a very early stage but shows promising results, as a processing time of 0.5 ms/event has already been reached.

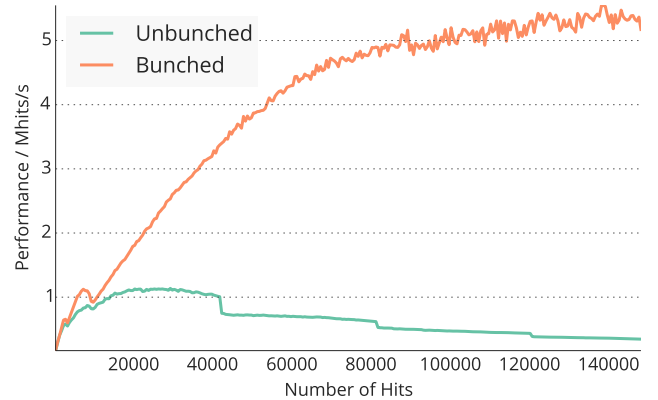


Fig. 1: Performance of the Triplet Finder with and without the bunching wrapper.

Triplet Finder A novel algorithm designed specifically for the $\bar{\text{P}}\text{ANDA}$ STT⁴ is the Triplet Finder. The algorithm uses a hit from a dedicated STT layer (*pivot layer*) to calculate a three-hit combination (triplet) from this hit and two adjacent hits. To form a track, it is combined with a triplet of another pivot layer as well as the $(0, 0)$ point. Benefits of using this technique are small computing times and the possibility to obtain particle tracks of sufficient resolution without using the event starting time t_0 .

Initial work on the Triplet Finder was carried out by Marius Mertens [6]. The feasibility of the concept was proven in subsequent work currently in the process of publication.

The GPU version of the Triplet Finder is implemented by

¹Anti-Proton Annihilation at Darmstadt

²Facility for Antiproton and Ion Research in Europe

³Graphics Processing Units

⁴Straw Tube Tracker

Andrew Adinetz of the NVIDIA Application Lab. Additionally to porting the basic properties and features of the Triplet Finder, some multicore-specific modifications have been made. An example is the implementation of bunching, a wrapping class allowing a chosen, thread-based algorithm to always run with the amount of input data corresponding to the maximum efficiency.

The striking difference in average computing times can be seen in Figure 1. Shown is the performance (number of processed hits per second) of the Triplet Finder as a function of the number of processed hits. The blue line displays the unbunched version of the algorithm: All hits are processed in one call. The complexity of $O(n^2)$ can be seen, as the algorithm compares every hit to other hits. The step structure in the line originates from not optimally filled GPU kernels. The red line represents the performance of the bunched version of the Triplet Finder. Not all hits are processed at once but the whole set of hits is sub-divided into smaller chunks of hits, with chunk sizes chosen to fill up GPU thread blocks and memory most efficiently. Only hits belonging to one bunch are processed in one call leading to a decoupling of performance from event sizes. A bunch size of $1\mu\text{s}$ is shown. The processing time for a single track event with the bunched Triplet Finder is 0.015 ms/event.

Outlook The basic cores of three online tracking algorithms (Hough Transform, Riemann Track Finder, Triplet finder) have been implemented on GPUs. The algorithms are in different stages of their qualitative analysis but already show promising results to be capable of handling PANDA's online tracking requirements.

For some algorithms, additional tools first have to be programmed for further algorithmic evaluation (e.g. multipeak finder). Also, all three algorithms have yet to be implemented into PandaRoot, enabling a direct comparison to Monte Carlo data.

References:

- [1] P. Hough, Machine Analysis of Bubble Chamber Pictures, Proc. Int. Conf. High Energy Accelerators and Instrumentation, 1959.
- [2] R. O. Duda & P. E. Hart, Use of the Hough Transformation to Detect Lines and Curves in Pictures, Comm. ACM, Vol. 15, pp. 11 – 15 (January, 1972).
- [3] J. Hoberock & N. Bell, Thrust, <http://thrust.github.com>.
- [4] NVIDIA Corporation, CUDA, <http://developer.nvidia.com/cuda>.
- [5] A. Herten, Implementations of Hough Transformations on GPUs for PANDA, Annual Report 2012.
- [6] Jülich Center for Hadron Physics / Institut für Kernphysik / COSY, Annual Report 2012, Chapter 6.4.
- [7] R. Frühwirth, A. Strandlie, W. Waltenberger, Helix fitting by an extended Riemann fit, Nuclear Instruments and Methods in Physics Research Section A: Accelerators, Spectrometers, Detectors and Associated Equipment, Vol. 490(1-2) pp. 366 – 378, (2002).

Development of a Silicon Strip Sensor Readout System

Dariusch Deermann

The **PANDA**¹ experiment will be one of the key experiments at FAIR². **PANDA** will examine the reaction of antiprotons at a beam momentum of 1.5 to 15 GeV/c with hydrogen and heavy nuclei.

The MVD³ is the inner most part of **PANDA** surrounding the interaction point and it is a combined system of silicon pixel and strip detectors. It will have four barrel layers, with pixel detectors in the inner two layers and strip detectors in the outer two layers. Furthermore, **PANDA** has fixed target kinematics and a corresponding boost in forward direction for any reaction. Therefore, six detector discs in the forward direction are implemented in addition to the barrel layers. The first four discs consist of pixel detectors only, while discs 5 and 6 consist of an inner pixel disc together with a surrounding ring of strip detectors. Those rings consist of 24 trapezoidal strip detectors, each with a stereo angle of 15°.

The first prototypes of the trapezoidal sensors have been produced this year by CiS⁴. They are 56 mm long and have 512 strips per sensor side with a pitch of 67.5 μm . The substrate is n^- doped with p^+ doped strips on the top side and n^+ doped strips on the back side. The backside strips are separated by p -spray, which means the whole backside surface gets a light p doping. Figure 1 shows the sensor embedded into a sensor board with pitchadapter and 4 APV25 frontend chips.

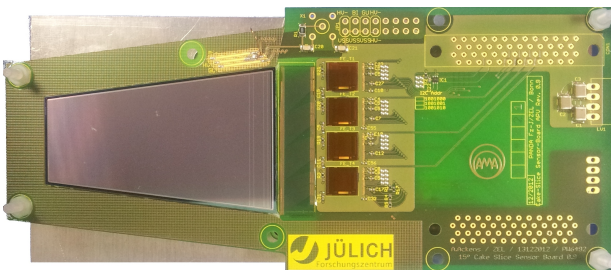


Fig. 1: A trapezoidal silicon strip sensor for the **PANDA** MVD with sensor board.

For the pixel part of the **PANDA** MVD a readout system had been developed in J  lich. This readout system uses a ML605 FPGA board which is usually connected to the PC by an optical SIS100 connection [1]. In order to have a more convenient system, which can be plugged into any available PC, the ethernet connection of the ML605 can be used instead of the SIS100 interface as well.

A first ethernet implementation was done in 2012 [2], which enabled communication by LAN. In the first version single UDP packages could be sent, which can contain up to 368 data words. Each data word consists of 32 bits. With this method a transmission rate of up to 45 MBit/s was reached. For the **PANDA** data acquisition a higher transfer rate

is needed. For this reason the DMA⁵-mode data transfer was extended by the functionality of sending multiple UDP packages as an answer to a single request from PC side. The first 32 bit word of each UDP package is now a command word which uses its first 8 bits to define its type and the last 24 bits for additional information. In case of data transfer the first 8 bits either indicate DMA_REPLY or DMA_LAST_REPLY to show whether there is a following package and uses the remaining 24 bits as a counter. The PC side can use the counter and the DMA_LAST_REPLY flag informations to confirm that no data was lost in the process. With multiple UDP packages a data rate of more than 700 MBit/s is achieved in the readout system.

With 32 bits per data word, one data word per signaling strip and an average of up to 4 signaling strips per physical hit, this corresponds to more than 5.5 million hits per second as a maximum hit rate that can be processed. If two sensors are being operated by the same ML605 board, this rate drops to more than 2.75 million hits per second and sensor.

For the **PANDA** experiment a new ASIC will be designed to readout the silicon strip sensors. This ASIC will work without a trigger and will provide the data as digital output. However, to test our readout system and the prototype sensors, existing frontend chips have to be used. In this case the APV25. The APV25 is a triggered frontend chip that provides analog data output.

To run this frontend chip with the readout system, an ADC⁶ card has to be used and the APV25's output scheme must be processed by the ML605. In order to process the APV25 data a VHDL⁷ module for the APV25 input, as well as a pedestal correction module and a hitfinder module have been implemented into the FPGA firmware. While the input scheme and hitfinder module are based on an existing code [3] the pedestal correction module was newly developed. The ADC card which will be used is a MI125 with 16 channels and is currently being implemented into the readout system.

To gain knowledge of the sensor's behavior and also to assure quality, the sensor's leakage current as well as its capacitance against the used biasing voltage was measured. These tests were realized with a proberbench⁸, a LCR meter⁹, a Source meter and a laptop computer to control the measurement tools and read their results.

The sensor was placed on the proberbench chuck and contacted with two needles at the bias ring and the edge of the sensor to provide bias voltage. This is already enough to measure the leakage current. For capacitance measurements the backside of the sensor needs to be contacted as well.

Since this is not directly possible, the chuck is used as an indirect backside contact. The chuck is a metal plate which

⁵Direct Memory Access

⁶Analog Digital Converter

⁷Very High Speed Integrated Circuit Hardware Description Language

⁸It is a computer controlled measuring station for device with small contact pads

⁹High precision multimeter for inductance (L), capacitance (C), and resistance (R)

¹anti ****PANDA at DArmstadt

²Facility for Antiproton and Ion Research

³Micro Vertex Detector

⁴Forschungsinstitut f  r Mikrosensorik und Photovoltaik GmbH

has a much higher capacitance compared to the sensor, so that its influence on the total capacitance is neglectable but may increase noise. The results can be seen in Figure 2. The

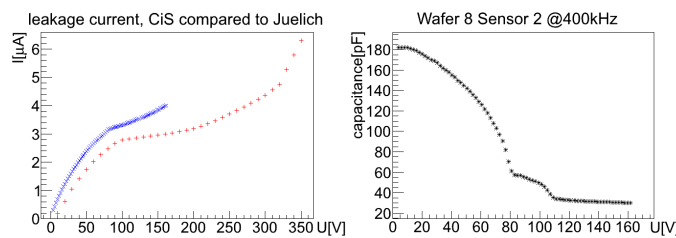


Fig. 2: CV and IV graph. In the IV graph red resembles Jülich and blue resembles CiS.

observed leakage current is just a little higher than the measurement done by CiS, which was done before the sensor was cut out of the wafer. The small difference in leakage current might be induced by a slightly higher temperature in our laboratory. With increasing bias voltage the depletion zone inside the sensor's silicon substrate grows and therefore the capacitance decreases because of the bigger gap between the two conductive layers inside the sensor. Above 110 V the capacitance stays almost constant which indicates full depletion of the sensor.

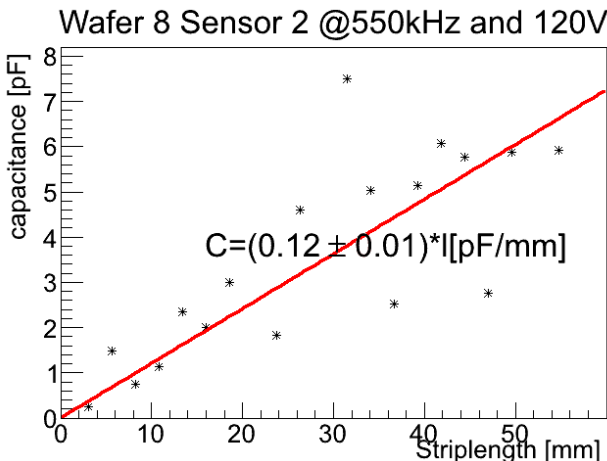


Fig. 3: Capacitance measured as a function of the strip length.

Due to the trapezoidal sensor shape, the strips do not all have the same length. A measurement of the capacitance as a function of the strip length shows a linear growth with increasing strip length. This measurement was done with 120 V bias voltage.

Even though the general trend of growing capacitance is visible in Figure 3, the results showed large fluctuations.

After the implementation of the ADC card into the readout system is done, the next step will be a testing the complete setup in a beam. This will give insight into the sensor's spatial and time resolution as well as the speed and functionality of the readout system.

Furthermore, the measurement of the sensor strip's capacitance as a function of the strip length will be redone with higher precision by the use of a dedicated test board on which

a sensor will be glued and bonded, so that it won't be necessary to use the proberbench's chuck as the backside contact replacement.

References:

- [1] The Jülich Digital Readout System for PANDA Developments, Simone Esch, IKP-1, DPG Frühjahrstagung 2012
- [2] Ethernet Implementation into the Jülich Digital Readout System, Andre Goerres, IKP, PANDA collaboration meeting september 2012
- [3] Untersuchungen zur First-Level-Datenauslesestrukturen für den Silizium-Streifendetektor im Mikro-Vertex-Detektor von PANDA, diploma thesis, Robert Schnell, 2009

Analysis of $\Lambda\bar{\Lambda}$ decay with PandaRoot Analysis Framework

S. Esch and J. Ritman for the $\bar{\Lambda}$ PANDA collaboration

Investigations in hyperon physics is important to understand the creation of quark-antiquark pairs, in particular of the strange quark and the arrangement of quarks to hadrons. The $\bar{\Lambda}$ PANDA experiment will be able to access energetically all strange hyperons and single charmed hyperons. As a first test of the hyperon reconstruction capability of $\bar{\Lambda}$ PANDA the Λ was chosen. It is the lightest hyperon and it occurs in the decay tree of several heavier hyperons. Due to the decay via the weak interaction the strange hyperons have a comparable long lifetime and a decay length of several centimeters. Therefore most of the hyperons decay in an outer part or even outside the MVD. This leads to a worse track quality since the MVD delivers high precision track points in time and space.

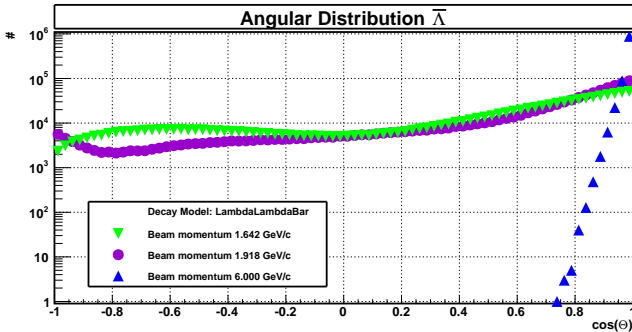


Fig. 1: Monte Carlo angular distribution of $\bar{\Lambda}$ for the three beam momenta.

To improve the reconstruction quality of tracks from the decay of Lambda hyperons plans exist to insert two additional semiconductor layers into the empty space between the MVD and the GEM stations, the so-called Λ -disks. The Λ -disks consist of semiconductor strip detectors and have a similar setup as the large MVD disks.

Simulations have been performed to investigate the reconstruction capability of the $\Lambda\bar{\Lambda}$ decay with the PandaRoot analysis framework and the contribution of the Λ -disks to the reconstruction of Λ hyperons. Four different Λ disk setups have been tested at three different beam momenta, 1.642 GeV/c, 1.918 GeV/c and 6.0 GeV/c. The generated angular distribution if the $\bar{\Lambda}$ can be seen in Figure 1.

The disk setups consist of an extended setup and three different locations of a compact setup (see Figure 2). The compact configuration has the advantage of sharing and saving electronic, mechanic and cooling resources.

Simulation, reconstruction and analysis has been done with the PandaRoot computing framework and the PandaGrid. The PandaRoot framework is still under development, due to this the usage of Monte Carlo information during reconstruction and analysis is still necessary.

The simulation has been done with 10^6 events for each setting.

After the analysis a reconstruction efficiency for the $\Lambda\bar{\Lambda}$ final state of 7.6% for 1.642 GeV/c was achieved, for 1.918 GeV/c 7.4% and for 6.0 GeV/c 2.8%. The overall low efficiency is an effect of not proper working software, which caused a reduction of ca. 20 percentage points.

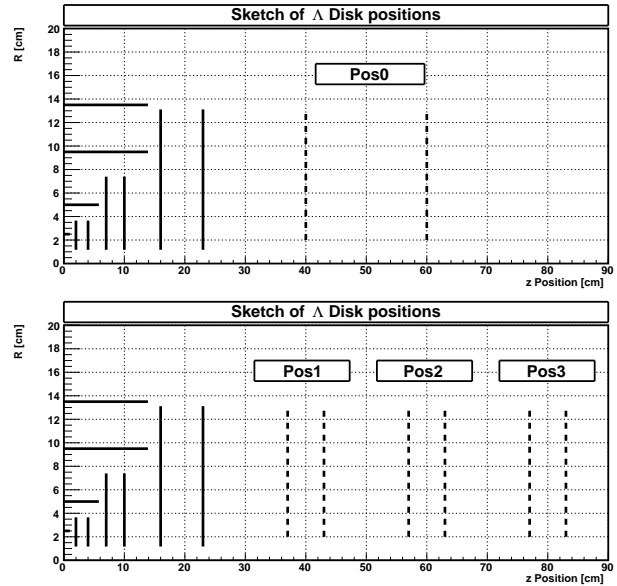


Fig. 2: Sketch indicating the four possible locations of the pair of Lambda-disks. The solid lines indicate the baseline MVD disks, and the dashed lines the Lambda disks.

The invariant mass distribution of the reconstructed tracks peaked at 1.116 MeV/c², in agreement with the PDG value. The resolution is between 2.4 MeV/c for the lowest beam momentum and 3.14 MeV/c for the highest beam momentum. The invariant mass distribution of Λ with the fit is displayed in Figure 3.

To exclude the effect of the poor working track fitter a comparison of the percentage of events with all $\bar{\Lambda}\Lambda$ final state tracks leaving enough hits points in the $\bar{\Lambda}$ PANDA tracking detectors was done (see 1).

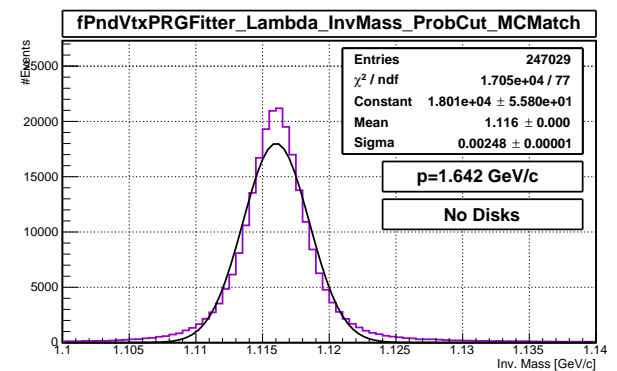


Fig. 3: Invariant Mass of the Λ particle after reconstruction.

The Λ -disks have a positive but small effect on the reconstruction efficiency of the $\Lambda\bar{\Lambda}$ final state. In general the $\bar{\Lambda}$ particles benefits more from the Λ -disks than the Λ particles, since the $\bar{\Lambda}$ are boosted in forward direction. The $\Lambda\bar{\Lambda}$ counting statistic rises roughly by 3.5 percent points for simulations with Λ -disks at 1.642 GeV/c. For 1.918 GeV/c and 6.0 GeV/c the counting statistic rises on average by 2.5 and 0.3 percent points. The high energy setting gains very less

P _{Beam}	Position	Λ	$\bar{\Lambda}$	$\bar{\Lambda}\Lambda$
1.642 GeV/c	-1	55.84%	55.90%	31.68%
	0	+1.06	+5.85	+2.98
	1	+0.48	+5.72	+2.98
	2	+1.63	+6.03	+3.91
	3	+1.62	+5.14	+3.50
1.918 GeV/c	-1	48.60%	58.82%	29.61%
	0	+0.04	+6.69	+2.44
	1	-0.13	+6.71	+2.34
	2	+0.53	+6.67	+2.80
	3	+0.75	+5.57	+2.53
6.00 GeV/c	-1	8.26%	52.84%	5.15%
	0	+0.02	+1.81	+0.41
	1	+0.01	+1.96	+0.41
	2	-0.17	+0.97	+0.32
	3	+0.05	+1.69	+0.32

Table 1: Number of events with detectable tracks of all $\Lambda\bar{\Lambda}$ final states before analysis.

from the Λ -disks, since the Λ gains nothing from the disks. The Λ are emitted backward in the center of mass system, due to the boost of the center of mass system they are emitted in the lab system nearly perpendicular to the beam axis with a very low momentum. Therefore it is very unlikely for the final state particles to hit the Λ -disks.

The variation between the different disk settings is very low. Disk positions which are further downstream have a slightly higher gain than closer ones, but the effect is very small. Due to this no position is preferred.

The Anti-Proton Annihilation at Darmstadt (PANDA) experiment is one of the main experiments at the Facility for Antiproton and Ion Research (FAIR), which is under construction in Darmstadt. PANDA's innermost part is the Micro Vertex Detector (MVD) with silicon pixel and strip sensors. The experiment's concept of a trigger-less operation requires a free-running readout solution, which should be capable of processing events up to 40 kHz/channel in hot spots of the strip part. Events will need an accurate time (<10 ns) and charge (resolution: 8 bit) information, while using less than 4 mW per channel (requirements from [1]). Because of the simplicity of a time-based readout, the TOFPET Application Specific Integrated Circuit (ASIC) provides a suitable basis for the readout of the MVD's strip sensors.

The TOFPET ASIC The ASIC was developed as a readout solution for silicon photomultipliers in the EndoTOFPET-US experiment, more detailed explanations can be found in [2]. It is an image-guided diagnostic system based on a PET scanner. The ASIC delivers a high precision time measurement with a time binning of 50 ps at 160 MHz nominal clock rate, to add a time of flight information. While being capable of running with input event rates of up to 100 kHz, the simple analog design leads to a low power consumption at around 7 mW per channel. It combines 64 channels on a 7.1×3.5 mm² 130 nm CMOS chip. These are the starting parameters for a development towards an adapted offspring for the MVD, the PANDA Strip ASIC (PASTA).

The ASIC's readout concept Even though the high time precision is not needed per se, it helps in getting an accurate value for the charge by measuring the time over threshold (TOT). Both ASICs use a low threshold setting V_{th_T} to minimize time walk effects and a second, higher threshold V_{th_E} to reduce the influence of dark counts. This also delivers an additional mark on the falling edge of the pulse for the TOT.

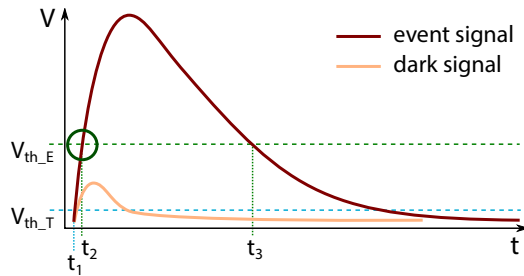


Fig. 1: A simplified signal after the pre-amplifier. Two discriminator levels deliver in four points in time, t_1 and t_3 are stored for time of arrival and time over threshold. Valid events have to exceed V_{th_E} (circle).

Because the nominal operation frequency of the chips is 160 MHz, it delivers an intrinsic timing resolution of 6.25 ns. To get an even finer resolution, a time amplification is performed. The basic concept is to discharge and recharge a capacitor with different constant currents. By separating this process into buffering and amplification and introducing multiple buffers in parallel, event bursts can be stored in different buffers before they are processed further [3]. This

enables a dead time between following events of a few clock cycles ($\approx 20 - 30$ ns at 160 MHz). However, this is not to be mistaken with the continuous rate capability, which is mainly limited by the recharging process and the analog preamplifiers. In total, a time amplification of 128 is reached, leading to a binning of 50 ps at a continuous rate of up to 100 kHz.

Modifications for the MVD strip readout Despite the same concept, a lot of design changes influence the PASTA chip. One of the most important changes is the adaptation to different input signals, caused by a much lower capacitance of silicon strips. A new approach will not only respect the different input, but also increase the linearity for the time over threshold measurement, thus increasing the accuracy. An overall optimization of the circuitry will reduce power dissipation from 7 mW/ch in the TOFPET by 2-3 mW/ch, getting closer to the target of 4 mW/ch.

Geometrical constraints for placing the readout makes it necessary to reduce the chip's channel pitch from 102 μ m to 60 μ m. Changing to an area optimized technology with a smaller structure size of 110 nm is a big help in this process. This alone reduces the occupation with active cells in the digital domain almost by a factor 2. Additionally, rewriting the block that controls the charging operations (TDC_CTRL) described earlier saves 80-90 % of occupied area¹ and ≈ 1 mW/ch of power dissipation for this particular block.

A feature the TOFPET ASIC is missing completely is radiation protection. Concentrating on non-permanent effects, the digital domain of the PASTA chip will contain appropriate protection. Basically, redundancy in digital buffers (flip flops) prevents unpredicted logic operation states. Two methods are used: triple-mode redundancy (TMR) [4] for single-bit buffers and Hamming encoding [5] for multi-bit buffers like state machines. This has been done for the TDC_CTRL before it was rewritten, the protection for the current version of the logic is pending.

Outlook In the course of 2014, the remaining changes to the TOFPET's concept will be finished and a first prototype of the PASTA chip will be produced. A thorough testing of the chip's behavior, especially the susceptibility to radiation effects, will follow afterwards.

References:

- [1] The PANDA Collaboration, *Technical Design Report for the PANDA Micro Vertex Detector*. (2011) http://panda-wiki.gsi.de/pub/Mvd/MvdTalkOrPaperDrafts/panda_tdr_mvd.pdf
- [2] Rolo, M. D. et al, *TOFPET ASIC for PET applications*. *Journal of Instrumentation* (2013) 1748. <http://dx.doi.org/10.1088/1748-0221/8/02/C02050>
- [3] A.E. Stevens et al., *A Time-to-Voltage Converter and Analog Memory for Colliding Beam Detectors*. *IEEE Journal of Solid-State Circuits* 24 (1989) 1748.
- [4] Lyons, R., Vanderkulk, W., *The use of triple-modular redundancy to improve computer reliability*. *IBM Journal of Research and Development* (1962) April.
- [5] Hamming, R., *Error detecting and error correcting codes*. *Bell System technical journal* (1950) XXIV.

¹This block occupies ≈ 20 % of the total area.

ADC based readout system for the Straw Tube Tracker at PANDA

L. Jokhovets, M. Drochner, A. Erven, W. Erven, G. Kemmerling, H. Kleines, P. Kulessa, H.W. Loevenich, P. Marciniewski, M. Mertens, H. Ohm, T. Preuhs, K. Pysz, J. Ritman, V. Serdyuk, S. v. Waasen, P. Wintz, P. Wüstner

I. INTRODUCTION

The work concerns with ADC based data acquisition system for PANDA (AntiProton Annihilations at Darmstadt) Straw Tube Tracker (STT). Test-beam studies in terms of parameters and system architecture definition were carried out. We present on-FPGA real time processing dependent on neighboring straw data and introduce track reconstruction technique.

The system under development has a large number of processing channels, one per each of 4636 straw tubes, which could require an extensive hardware. In addition, a high data rate (up to 20 GByte/s) is expected. This data rate can lie beyond the storage and off-line analysis capabilities. Finally, high particle rate (up to about 1 MHz per straw tube) could lead to event mixing disturbing the measurements.

We start with single Fe-55 pulse response analysis, and determine the necessary combination of shaping time and sampling rate. Our motivation is to minimize the required digitalization and real time processing power. Then, aimed at reducing the data rate to a level suitable for off-line processing, we have investigated the proton beam response and introduced real time processing dependent on the neighboring straw data including following operations

- event building and filtering
- clustering
- self-triggering
- pile-up detection

In our experiments we use the data acquisition system originally developed for the WASA at COSY experiment [2]. The straw signal readout chain consists of front-end transimpedance amplifiers with gain factor of about 360 as well as flash-analog-to-digital converters (FADC) with sampling rate of 240 MHz and binning of 260 ps using subsampling [3]. The digitized data are processed in FPGAs to get leading edge parameter and energy calculation features. The data are buffered continuously in on-FPGAs random access memory (RAM). Processing of buffered data is trigger initiated. The acquisition modules can also be programmed to record the raw sampled data for investigation purposes.

We have modified this system for test beam by introducing real time processing feature. Furthermore, the system can run at the original sampling rate of 240 MHz and at the reduced rate of 120 MHz involving only every second sample into processing.

II. SHAPING TIME, SAMPLING RATE AND TIME RESOLUTION

In order to investigate the influence of the sampling rate on the time measurement, tests with Fe-55 irradiation were performed. We assume, that the pulse duration response by Fe-55 irradiation to be comparable to single cluster pulse by proton beam and is the shortest pulse in system. The comparison of constant fraction time measurements by sampling rate 120 and 240 MHz shows deviation of more than 1 ns (Fig. 1). This accuracy doesn't fulfill the requirements for time resolution in STT [1]. To improve the results, the shaping time has been increased by including a 20 m long cable into the system electronic chain.

The pulse form is changed: the amplitude has been decreased and the pulse duration increased (Fig. 2). The deviation between measurements with 240 and 120 MHz appears smaller, and reaches 300 ps using real time signal fitting (Fig. 2).

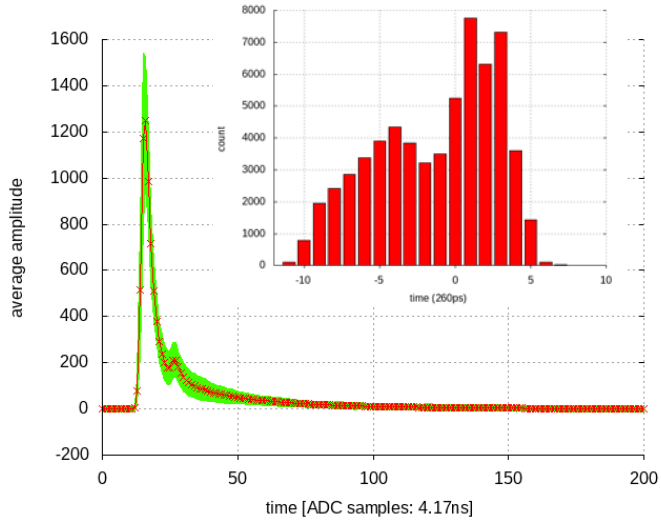


Fig. 1. Sampled response to Fe-55 irradiation and difference in constant fraction time measurements by sampling rate 120 and 240 MHz.

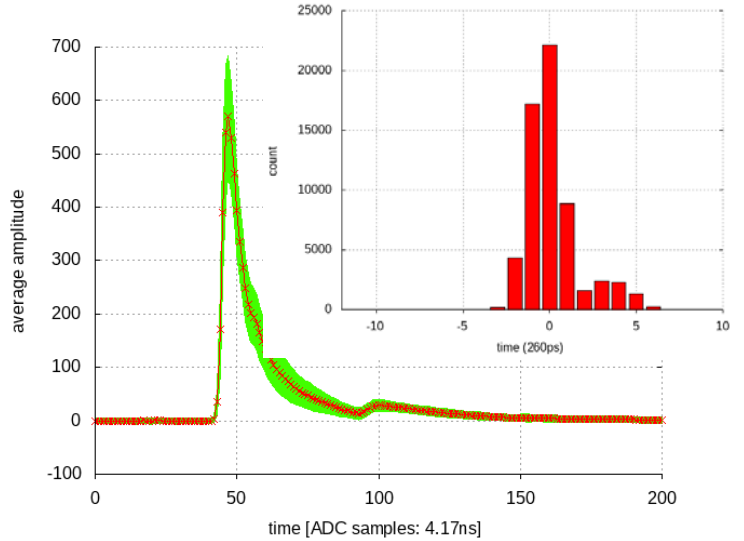


Fig. 2. Sampled response to Fe-55 irradiation and difference in constant fraction time measurements by sampling rate 120 and 240 MHz using increased shaping time due cabling.

Increasing the shaping time we can reduce the sampling rate down to 120 MHz. Single clusters with an ionization energy over average as well as the multiple clusters overlapping will be registered with the time uncertainty of ~ 300 ps. Single clusters with energy below average do not matter, while they are covered with noise. We have estimated [4] that compared to other tracker experiments [5, 6], the reached time resolution will be better. However, if we will get in electronic chain the higher SNR we will have an opportunity to increase the resolution increasing the sampling rate. Therefore we keep open a possibility to get higher sampling rate making small changes in the same system. Together with high density design requirement, this makes preferable the separate implementation of sampling and processing hardware.

III. REAL TIME PROCESSING DEPENDENT ON NEIGHBORING STRAW DATA

Test beam studies were performed as a background for processing operations introduced later. Proton beam of a momentum of 2.7 GeV/c, the Ar/CO₂ gas mixture of 90/10 and high voltage of 1800 V were used. Signals from 64 straw tubes in test setup were sampled with 240 MHz and recorded in 5 μ s time windows. The trigger for readout was generated by an external scintillator detector.

In Fig. 3 one can see pulse responses of 4 straws on the same particle track.

- Leading edges give the time of the first arrived cluster in each straw tube.
- Trailing edge time is the same for all straws on track.

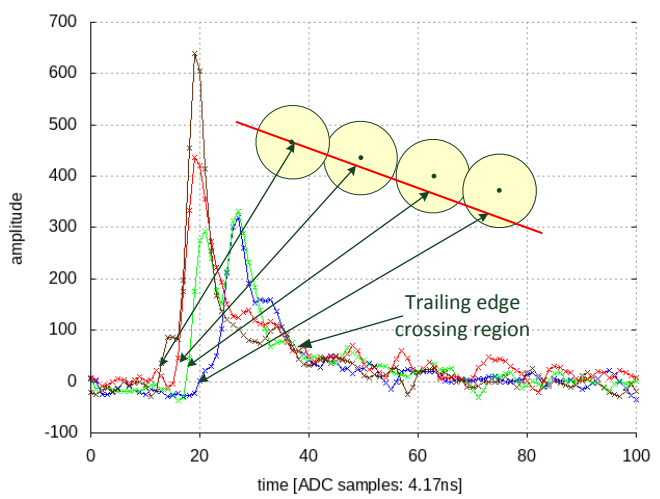


Fig. 3. Signals of 4 straws crossing by same particle.

- Pulse shape appears as superposition of about 30 cluster responses. This increases the number of sampling points in the leading edge compared to Fe-55 response (Fig. 1, Fig. 2) and flattens peaks of single cluster responses.
- When particle track passed near the wire clusters arrive at the wire spread out in time (~ one cluster per 3 ns) and the pulse shape structure appears irregular (Fig. 4). One can also observe a dispersion in the

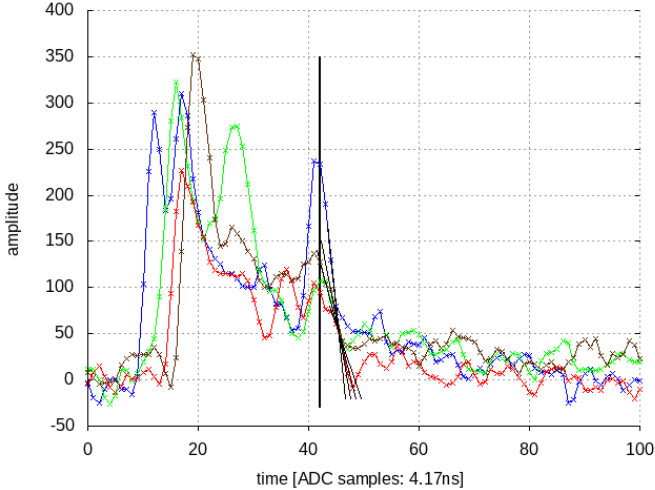


Fig. 4. Track near the wire: trailing edges slopes cross themselves in small region, the last maximum position is not the same.

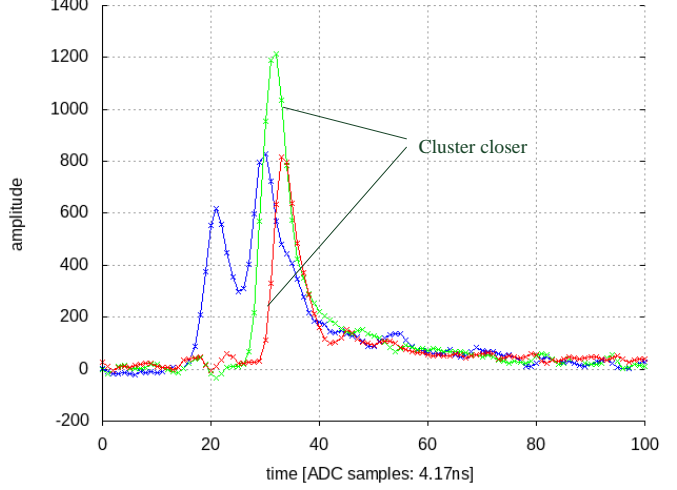


Fig. 5 Track near the wall: Maximums of cluster closers have the same time.

arrival of the last clusters due to spread of primary ionization clusters on track. Position of the last maximum is not the same. However the trailing edges slopes cross themselves in small region and allow to establish the precise boundary for arrival time of the very last cluster (wall time).

- In the case of track passed far from wire (Fig. 5), the difference between arrival times of clusters is in average smaller than in the first case and the pulse shape is more regular. Maximum of cluster closer pulse gives smallest deviation to the native maximum of the last arriving cluster, thus the best reference time for the track to wire distance definition and for tracking reference (wall time). The regular form of this pulse makes it well suitable for interpolation (see experimental results with interpolation of Fe-55) increasing the resolution.

Proton beam tests have shown, that the trailing edge selection is possible via detection of cluster closer maximum in combination with the selection of trailing edges crossing region. This recognition appears as a basic feature for clustering.

A. Event building

We define event as the detection of a signal proposed to be ionization cluster response, for example selected via amplitude over a defined threshold. Straw signals are processed in real time. This means, all crossed straw tubes detect the same time trailing edge of response. The only difference due to electronic channel tolerance, propagation time and clusters spread takes place and should be taken into account. The leading edge parameters for all peaks are calculated in real time too and buffered for maximum possible drift time (200 ns).

B. Event filtering

Analysis shows that 14 % of noise peaks above base have a duration comparable with cluster response. This noise can be rejected considering neighboring straw signals. The filtering search window will be defined according to whole drift time, propagation time, the electron spread and electronic chain tolerance.

For each channel we check event presence in the neighboring (2) and in the second order (3) neighboring straws (Fig. 6). If no event happened in the neighboring straws, the event should be discarded.

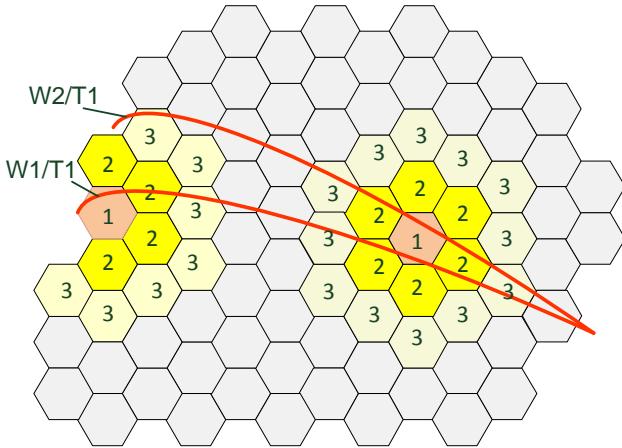


Fig. 6. Event filtering.

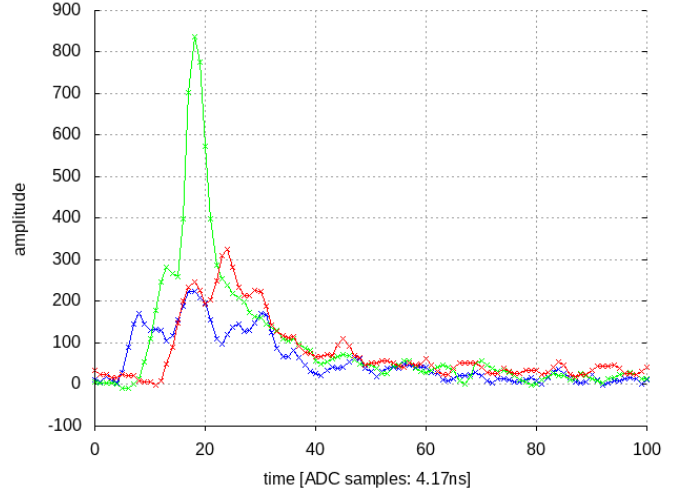


Fig. 7. Low amplitude signal interpretation.

Besides the data stream reduction, event filtering has one more function. By analyzing of local track, it is able to process signal close to noise level. This increases efficiency of STT and is especially important for tracks near the wire, having low amplitude response. For example, the blue curve in Fig. 7 shows low amplitude signal. If events presence in neighboring channels (green and red curves) is found, it can be processed as a signal from particle.

C. Self-triggering and clustering

Using the drift time measurement for track reconstruction requires a time reference, usually provided by scintillator trigger system. The system under development runs in self-triggering mode. Indeed, we register the both leading and trailing edge of signals. This is enough for track to wire distance calculation, as well as for grouping of events on the same track - clustering.

- Due to clustering the data stream will be reduced at least by 25%.
- The largest advantage of clustering is that sorting off-line, as the most critical path by high data rate of 20 GByte/s, will be overcome.
- The next point is, that clustering effects as another kind of filtering. If the number of straws crossed the same time is less than this one needed for successful track reconstruction, the events should be discarded. Both kinds of filtering can be combined.
- Finally, real time clustering allows the real time track reconstruction.

D. Pile-up recognition

The expected total drift time in PANDA STT is from about of 100 ns for fast up to 150 ns for slow gas. The magnetic field presence and finite shaping time lead to an increase of pulse duration up to 300 ns. We cannot distinct possible multiple tracks crossing the same tube (event mixing) and the amount of clusters belonging to the

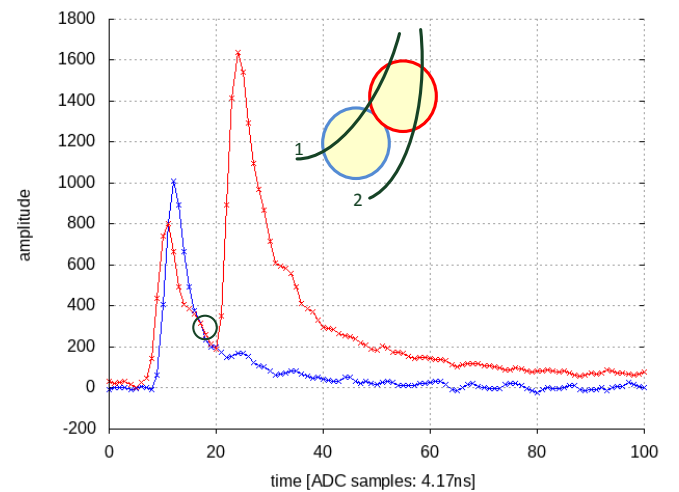


Fig. 8. Event separation.

same track within 100-300 ns based on the single straw data.

Fig. 8 illustrates that dependent on the neighboring straw data, we can select multiple tracks, crossing the straw tube the same time. The first trailing edge is the same for both pulses, which means that particle 1 crosses both straw tubes. The particle 2 crosses one of these tubes. For sufficient track resolution response of all neighboring straws should be involved.

The pile-up recognition allows track selection giving more tracking points and thus rise to system efficiency.

IV. HARDWARE UNDER DEVELOPMENT

Processing dependent on neighboring straws requires high density design. Any subdivision leads to additional overlap and increases the processing power. Therefore the system requirements have been determined as followed:

- Large number of channels should be processed on the same FPGA
- Large number of FPGA should be integrated on the same FPGA-board
- Large FPGA-board dimensions are of choice
- Point-to-Point connections between FPGA-boards are needed
- Using one of hardware standards is preferred.

The ATCA standard [7] with full-mesh network backplane topology meets the requirements. The next system feature is its configuration according to PANDA STT structure (for example, Fig. 9). In this case only information transfer (for event building/tracking) between neighboring boards is required. Assuming the 125 MHz sampling the whole system for PANDA STT project can be built on 1 or 2 ATCA crates. Up to 400 straw channels will be processed on each ATCA board, including up to 10 Kintex 7 FPGAs. The data will be sampled with 8-channel, 125 MHz Linear Technology ADC and transferred to FPGA via low voltage differential signal (LVDS) serial lines (Fig. 10).

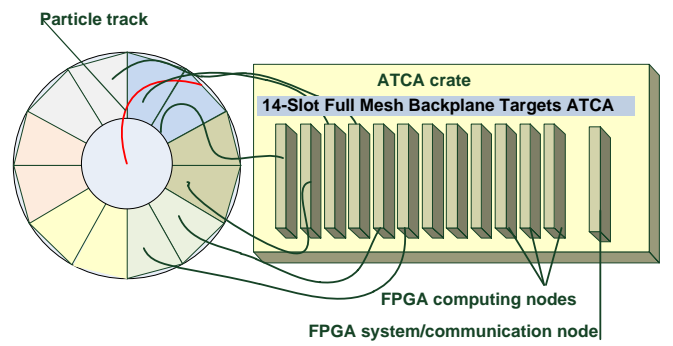


Fig. 9. Implementation insides ATCA crate.

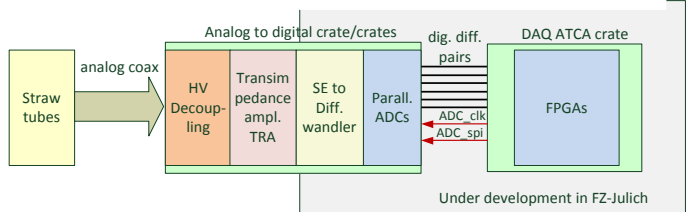


Fig. 10. The data acquisition system general structure

Analyzing pulse response to Fe-55 irradiation we have demonstrated, that with increasing of shaping time up to ~ 25 ns, reducing of sampling rate down to 120 MHz is possible. This is still sufficient to get all pulse parameters with a very small deviation of ~ 300 ps compared to sampling with 240 MHz.

To select the closest information concerning the first cluster, the leading edge discriminator technique should be improved taking into account only first few sampling points according to the tested response of Fe-55 under definite conditions.

We should keep open a possibility to get higher sampling rate making small changes in the same system. Together with high density design requirement, this makes preferable the separate implementation of sampling and processing hardware (Fig. 10).

Proton beam tests have shown, that the trailing edge selection is possible via detection of cluster closer maximum in combination with the selection of trailing edges crossing region. This allows grouping of events on the same track (self-triggering, running without external trigger) for clustering. Due to clustering

the data stream will be reduced at least by 25%, and sorting off-line, as the most critical path by high data rate of 20 GByte/s, will be overcome. In addition, real time clustering allows the real time track reconstruction.

Using data processing based on neighboring straws, the noise rejection up to 14 % can be achieved leading to further data stream reduction. Signals close to noise level will be processed increasing STT efficiency.

The pile-up recognition allows track selection giving more tracking points. This is the second reason giving rise to system efficiency.

The proposed hardware makes the efficient basis for implementation of all above mentioned processing features and operations. A very compact implementation with high integration and high flexibility level makes it a good choice of STT data acquisition system.

REFERENCES

- [1] PANDA Collaboration, Straw Tube Tracker Technical Design Report, <http://arxiv.org/abs/1205.5441v2>.
- [2] WASA Collaboration, Proposal for the Wide Angle Shower Apparatus (WASA) at COSY-Juelich - "WASA at COSY", <http://arxiv.org/abs/nucl-ex/0411038>.
- [3] P. Kulessa et al., A sampling ADC as a universal tool for data processing and trigger application, *Proceedings of Science*, http://pos.sissa.it//archive/conferences/160/012/Bormio2012_012.pdf.
- [4] L. Jokhovets et al., "Investigation of an ADC based signal processing and design of an ATCA data acquisition system unit for the Straw Tube Tracker at PANDA," *Conference Record IEEE NSS/MIC, 2013, NPO2-176* (2013)
- [5] T. Akesson et al., "Particle identification using the Time-over-threshold method in the ATLAS Transition Radiation Tracker," *Nuclear instruments and methods in physics research*, section A474, pp. 172-187, 2001.
- [6] E. Abat et al., "The ATLAS TRT Electronics," *JINST* 3 P06007, 2008.
- [7] T. Jezynski et al., "ATCA/ μ TCA for Physics," *Nuclear Instruments and Methods in Physics Research*, section A623, 1, pp. 510-512, 2010.

The electronical time-resolution for the PANDA Straw Tube Tracker for Fast Flash-ADC read out

H. Ohm^a, L. Jokhovets^b, A. Erven^b, K. Pysz^c, P. Kulessa^c, J. Majewski^c, R. Nellen^a, V. Serdyuk^a, P. Wintz^a

^a IKP-FZ Jülich, ^b ZEA2-FZ Jülich, ^c IFN PAN, Krakow, Poland

Readout of the PANDA central Straw Tube Tracker (STT) with fast flash ADCs permits simultaneous deduction of charge and arrival time of signals for precise energy-loss measurements and particle tracking [1,2,3]. For the application of this technology and in order to cope with the extreme space restrictions and limitations for heat dissipation in the immediate vicinity of the STT inside the PANDA main volume we pursue the following solution: The primary straw signals will be transferred via approx. 12 m long coaxial cables to a location outside the main detector where all electronics from the preamplifier to the digital electronics will be placed in a compact arrangement in few crates. The cables will simultaneously be used for signals and for high voltage and thus make efficient use of the strongly limited space in the cable channels.

All in all this solution does not only solve problems due to the very strong boundary conditions given by the architecture of the PANDA detector but it also offers further advantages:

- Real-time digital signal processing permits application of timing techniques for compensation of amplitude and rise-time effects
- Identification of poor-quality or fake signals, rejection of them or assignment of low weight factors for the track-fitting procedure
- Identification of a local base-line level for each individual signal even under rapidly changing experimental conditions like strongly varying count rates
- Variable signal integration for charge determination avoiding long amplifier shaping times and pile-up under high rates
- Pre-tracking analysis based on the comparison of the cluster structure in the signals of neighbouring groups of straw tubes
- Separate HV/signal cables permit disconnecting individual straw chamber instead of groups of straws in case of short circuit in a tube

During the current investigations the timing performance of the system was studied and compared with the specifications as given in the PANDA technical design report [4] which specifies the time resolution to be 1-2 ns. Since no simple direct measurement of the time resolution of straw tubes is feasible due to the inherent electron drift-time up to approx. 150 ns we measured for various conditions the noise level underlying the signal and the slope of the leading edge of the signal from which the electronical contribution to the time resolution can be deduced according to $\sigma_{time} = \sigma_{voltage} / (dV / dt)$

The influence of the following parameters was investigated:

- Type and lenght of the cable
- Impedance matching between straw and signal cable
- Impedance matching at the amplifier input

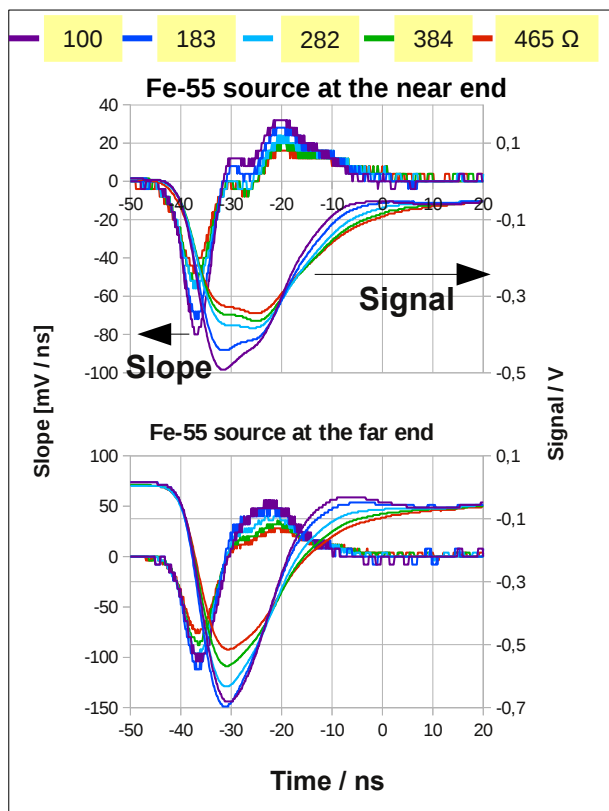


Fig. 1: Signals (right scale) and signal slopes (left scale) for various degrees of impedance matching (see legend on top of the diagram) and for opposite positions of the x-ray source. Nominally the best matching is achieved with $384\ \Omega$ (green lines). The connection between the straw and the amplifier was a 20 cm long twisted-pair cable with $Z \approx 100\ \Omega$.

baseline. The pulse deterioration seen for other values of R are in their consequences comparable or minor to the reflections at the open straw end which are manifested in the difference of signal shapes for opposite source positions. It was found, however, that precise impedance matching between long transmission cables and the amplifier input is crucial.

The RMS noise voltage and time resolution deduced for Fe-55 signals is presented in Fig. 2 for the amplifier coupled to the straw via cables covering a range of length from 20 cm to 20 m. The noise of the amplifier increases immediately when a simple passive circuit decoupling the analog signals from high voltage is plugged in. Cables as long as 20 m give fairly small additional noise contributions. The main effect of the cables is the reduction of the signal slope which is the dominating factor for the increase of the estimated time resolution.

For amplifier positions in the immediate vicinity of the straws values below $\sigma_{\text{time}} = 100 \text{ ps}$ are found both for 275 MHz and 60 MHz bandwidth amplifiers. The higher bandwidth does not give a visible improvement. When coupling the straw via 5 m, 10 m or 20 m long coaxial cables the estimated resolution increases in the worst case to 240 ps. For 10 m which is the most realistic length 100 ps are feasible for the cable type MK7501.

Straw chamber signals from Fe-55 x-rays, Sr-90 β -particles and cosmic rays as well as noise voltages were measured with a 200 MHz digital oscilloscope using a 60 MHz bandwidth transimpedance amplifier. From the signals the slope was deduced as shown in Fig. 1. Time-resolution estimates were deduced in two consecutive steps: The signal response for the various experimental conditions was always measured using the rather uniform single-cluster signal from Fe-55. Realistic estimates for minimum-ionizing particles were then deduced by normalizing the results to average signal slopes measured for Sr-90 and cosmics. Furthermore, these values were normalized to a total gas amplification of $5 * 10^4$ which is defined as an upper limit for the reduction of ageing effects in the straws [4].

The signal impedance of the straws ($Z \approx 373 \Omega$) is much higher than impedances of usual cables and amplifiers. Matching was varied over the range from 100 to 465Ω , see Fig. 1. The magnitude of the slope of the leading edge which is decisive for timing applications does not vary very strongly and it is best when no attempt is made to match the straw with the 100Ω cable. The nominally best matching with $R = 384 \Omega$ has the only advantage of a slightly faster return of the signal to the

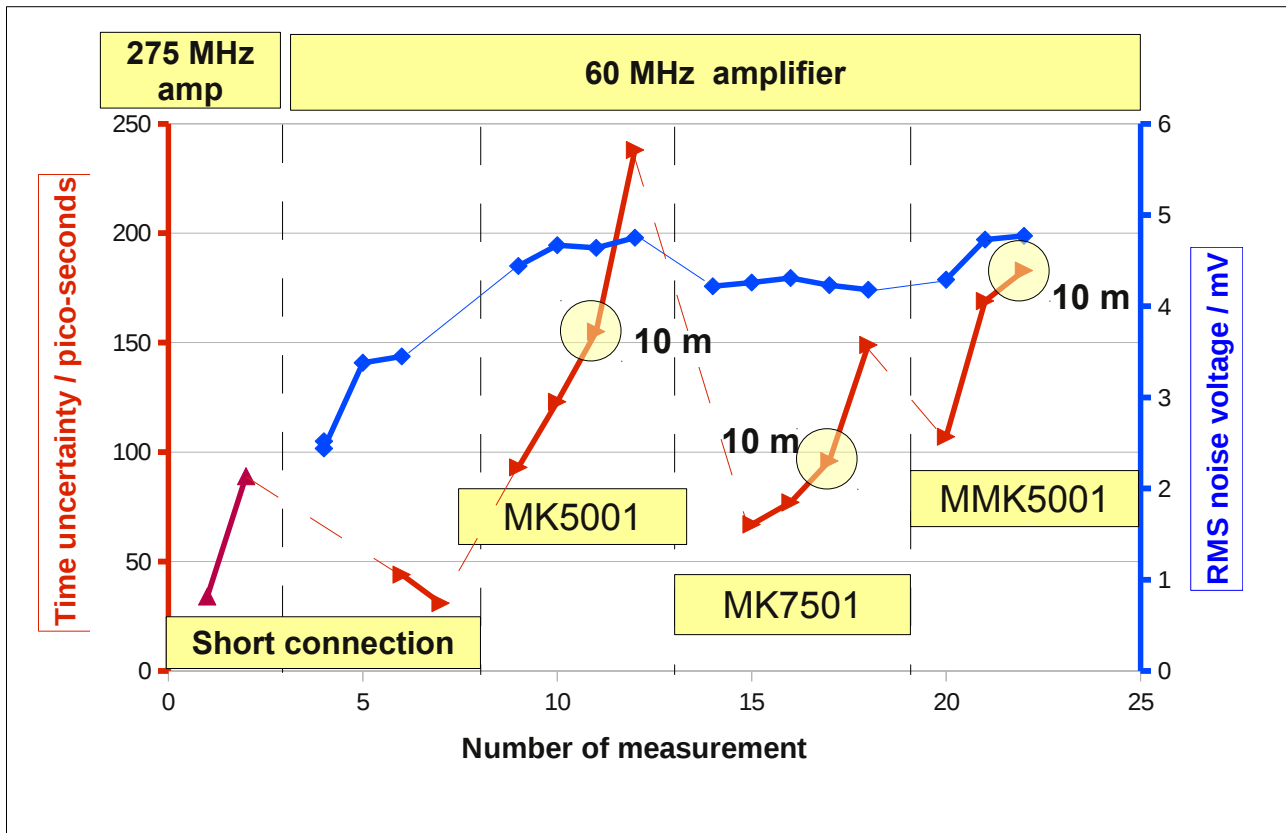


Fig. 2: RMS noise voltages (blue, right scale) and time uncertainties deduced for Fe-55 signals from the signal slope (dark red: 275 MHz, light red: 60 MHz amplifier, left scale). The noise voltage is shown only for the 60 MHz bandwidth amplifier. The time uncertainties are given either for short (20 cm) connections or for long coaxial cables with increasing length of 5 m, 10 m and 20 m. Values for 10 m cables are highlighted. For the MMK5001 the maximum length was 10 m. For each type of cable the first two values for the time uncertainty always refer to 5 m long cables with different techniques for the impedance matching between the cable and the amplifier.

Normalizing the time resolution obtained with Fe-55 signals to a reduced high voltage and to cosmics and Sr-90 a value of 680 ps is obtained for a 10 m long MK7501 cable. This value is well within the limits to be met. Further improvement is expected for amplifiers with optimized input impedance and a shaping optimal for the straw signals. It has to be noted that these resolution estimates include the assumption that timing is derived at the steepest point of the analog signal. No amplitude dependend walk effect is taken into account. These simplification are realistic when the above-mentioned flash-ADC technique with digital signal analysis is employed. With conventional leading-edge timing the amplitude variations are expected to lead to a worsening of the time resolution.

References

- [1] L. Jokhovets et al., contribution to this Annual report
- [2] P. Kulessa, 50th International Winter Meeting on Nuclear Physics - Bormio 2012
- [3] K. Pysz et al. DPG Spring Meeting, 21.03.2011, Muenster
- [4] Technical Design Report for the PANDA Straw Tube Tracker, April 20, 2012

A DIRC demonstrator at COSY

Adrian Zink*, Wolfgang Eyrich*, Liwen Li* and Florian Hauenstein* for the WASA DIRC group

Introduction

For the WASA-at-COSY experiment the implementation of a DIRC (Detection of Internally Reflected Cherenkov light) in the forward range was planned in order to improve the energy resolution for the passing protons and pions. The detector design consists of four quadrants of radiator material with attached focusing elements. In order to meet the requirements of the WASA experiment (proton energy from 450 MeV to 1 GeV and an angular acceptance from 4° to 17°), the quadrants are tilted by 20° with respect to the beam axis. After first prototype tests [1], which showed the feasibility of a DIRC made of acrylic glass (PMMA), half of the envisaged WASA DIRC was built as a demonstrator in order to study the behavior of the detector under experimental conditions, to develop and enhance the electronics, particularly with regard to an adaption to the PANDA DIRCs, and to investigate different photon detectors and focusing concepts.

Demonstrator concept

In order to demonstrate the DIRC concept a test experiment was set up behind the TOF experiment. In figure 1 a schematic view of the apparatus is shown. Upstream one scintillating fiber hodoscope (Scifi) was used to scatter the incoming protons and to determine their position. A second Scifi allows the tracking of the scattered particles. Downstream the two DIRC quadrants are placed to measure the β of particles. For the photon detection, Hamamatsu multianode photomultiplier tubes (MaPMTs) and Photonis microchannel-plate PMTs, capable of detecting single photons, are used due to the low number of expected photons per event (in the order of 10). The read-out of the PMTs is done by a newly developed front end electronics, an amplifier and discriminator board based on FPGAs, the PADIWA (PAndera DIRC WAsa), and by TRBv3 TDC boards[2].

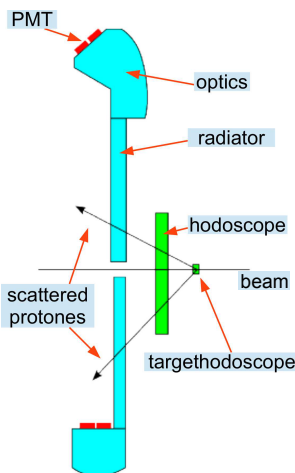


Fig. 1: Schematic drawing of the test experiment.

Beam test results

A first look into the 2012 data gives a brief overview of the functionality. In the upper part of figure 2 the hitpattern for a sample of unscattered protons is shown. Only the upper 3° of the Cherenkov cone with an opening angle of 45.2° are

guided the 0.8 m long path to the focal plane by total reflection (critical angle 42.15°). This results in a quasi straight line. In the lower part of the figure an image of the photomultiplier matrix facing the optics element is shown.

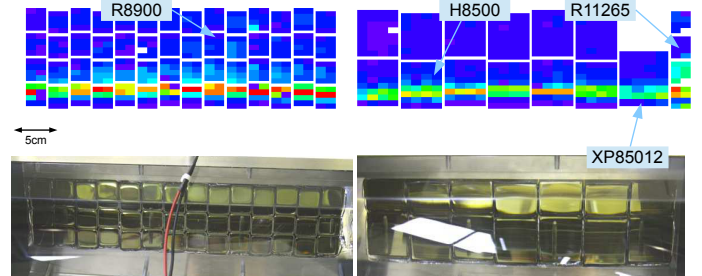


Fig. 2: Up: Photon hitpattern of beam protons on the focal plane for the Erlangen quadrant, down: picture of the photomultiplier matrix.

In figure 3 the hitpattern of a single scattered proton is shown. The additional scattering angle shifts the pattern up. Since the distance from the incident spot of the protons on the radiator plate to the focal plane is shorter and due to the slightly lower Cherenkov angle, the pattern is much more bended. From the position, shape of the distribution and the tracking of the proton, β can be reconstructed with the expected precision.

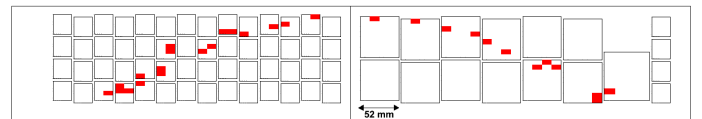


Fig. 3: Single event hitpattern of a scattered proton.

Conclusion and outlook

The demonstrator is the first working DIRC made from acrylic glass. Though the detector worked as expected, some challenges appeared. Particularly the large scale and the non-laboratory use of the TRBv3 and PADIWA boards helped to identify several bugs and limitations of the current design of the FPGA firmware and the board layouts. These were addressed and a further test measurement took place in autumn 2013, using improved electronics and a slightly modified setup. These developments are of special interest for the future PANDA experiment. The data analysis of the measurements is ongoing.

References:

- [1] A. Schmidt et. al., "Prototyping the WASA DIRC", 2011 JINST **6** C10005
- [2] M. Traxler et. al., "compact system for high precision time measurements (< 14 ps RMS) and integrated data acquisition for a large number of channels", 2011 JINST **6** C12004

* Physikalisches Institut IV, Universität Erlangen-Nürnberg, 91058 Erlangen